

1991

Mechanical and crystallographic anisotropy in zirconium alloy tubing.

Zoheir N. Farhat
University of Windsor

Follow this and additional works at: <http://scholar.uwindsor.ca/etd>

Recommended Citation

Farhat, Zoheir N., "Mechanical and crystallographic anisotropy in zirconium alloy tubing." (1991). *Electronic Theses and Dissertations*. Paper 2690.

This online database contains the full-text of PhD dissertations and Masters' theses of University of Windsor students from 1954 forward. These documents are made available for personal study and research purposes only, in accordance with the Canadian Copyright Act and the Creative Commons license—CC BY-NC-ND (Attribution, Non-Commercial, No Derivative Works). Under this license, works must always be attributed to the copyright holder (original author), cannot be used for any commercial purposes, and may not be altered. Any other use would require the permission of the copyright holder. Students may inquire about withdrawing their dissertation and/or thesis from this database. For additional inquiries, please contact the repository administrator via email (scholarship@uwindsor.ca) or by telephone at 519-253-3000ext. 3208.



National Library
of Canada

Bibliothèque nationale
du Canada

Canadian Theses Service Service des thèses canadiennes

Ottawa, Canada
K1A 0N4

NOTICE

The quality of this microform is heavily dependent upon the quality of the original thesis submitted for microfilming. Every effort has been made to ensure the highest quality of reproduction possible.

If pages are missing, contact the university which granted the degree.

Some pages may have indistinct print especially if the original pages were typed with a poor typewriter ribbon or if the university sent us an inferior photocopy.

Reproduction in full or in part of this microform is governed by the Canadian Copyright Act, R.S.C. 1970, c. C-30, and subsequent amendments.

AVIS

La qualité de cette microforme dépend grandement de la qualité de la thèse soumise au microfilmage. Nous avons tout fait pour assurer une qualité supérieure de reproduction.

S'il manque des pages, veuillez communiquer avec l'université qui a conféré le grade.

La qualité d'impression de certaines pages peut laisser à désirer, surtout si les pages originales ont été dactylographiées à l'aide d'un ruban usé ou si l'université nous a fait parvenir une photocopie de qualité inférieure.

La reproduction, même partielle, de cette microforme est soumise à la Loi canadienne sur le droit d'auteur, SRC 1970, c. C-30, et ses amendements subséquents.

**MECHANICAL AND CRYSTALLOGRAPHIC
ANISOTROPY IN ZIRCONIUM
ALLOY TUBING**

by

Zoheir N. Farhat

A Thesis

**Submitted to the Faculty of Graduate Studies and
Research Through the Department of Mechanical
Engineering (Engineering Materials Group) in
Partial Fulfillment of the Requirements for
the Degree of Master of Applied Science
at the University of Windsor**

Windsor, Ontario, Canada

1991



National Library
of Canada

Bibliothèque nationale
du Canada

Canadian Theses Service Service des thèses canadiennes

Ottawa, Canada
K1A 0N4

The author has granted an irrevocable non-exclusive licence allowing the National Library of Canada to reproduce, loan, distribute or sell copies of his/her thesis by any means and in any form or format, making this thesis available to interested persons.

The author retains ownership of the copyright in his/her thesis. Neither the thesis nor substantial extracts from it may be printed or otherwise reproduced without his/her permission.

L'auteur a accordé une licence irrévocable et non exclusive permettant à la Bibliothèque nationale du Canada de reproduire, prêter, distribuer ou vendre des copies de sa thèse de quelque manière et sous quelque forme que ce soit pour mettre des exemplaires de cette thèse à la disposition des personnes intéressées.

L'auteur conserve la propriété du droit d'auteur qui protège sa thèse. Ni la thèse ni des extraits substantiels de celle-ci ne doivent être imprimés ou autrement reproduits sans son autorisation.

ISBN 0-315-69898-5

Canada

Handwritten text

© All Rights Reserved
Zoheir N. Farhat 1991

ABSTRACT

In the present study, the annealing behaviour of 60% tube reduced and stress relieved Zircaloy-4 nuclear fuel cladding material is studied over the temperature range 300 to 1000°C for annealing times of 10^3 , 10^4 and 10^5 seconds. The annealing effects (recovery, recrystallization, grain growth phase transformation, and texture changes) were monitored using Knoop microhardness measurements, optical metallography, x-ray texture, and thermoelectric power (TEP) measurements.

For annealing temperatures up to 500°C there is little change in texture and mechanical anisotropy; rather, the tubing becomes softer due to recovery and removal of cold-work. In the temperature range 500 to 800°C, there is change in microhardness due to recrystallization and grain growth effects. The microhardness changes occurring in this temperature range are dependent on the direction of measurement in the tubing since a definite recrystallization texture is developed. For annealing temperatures above 800°C, the overall room temperature strength of the tubing is increased due to phase changes (β -Zr is formed at temperatures above 800°C and this transforms to α' on cooling to R.T.) and the tubing exhibits

a more mechanically anisotropic behaviour. The data on the mechanical anisotropy ratio (minimum/maximum hardness) shows that the recrystallized structure produced at about 500°C for annealing times 10^3 and 10^4 seconds is more mechanically anisotropic than the as-received tubing.

ACKNOWLEDGMENTS

I would like to express my gratitude to Dr. D. O. Northwood for his supervision, advice, encouragement and guidance throughout the course of this research and during my entire education at the University of Windsor.

Greatest thanks go to Dr. W. V. Youdelis for his informative directions and remarks. I would also like to thank Mr. J. W. Robinson for his technical assistance.

I am very grateful to all my family for their patience and encouragement throughout the years of my education.

CONTENTS

| | |
|---|-----|
| ABSTRACT | iv |
| ACKNOWLEDGMENTS | vi |
| CONTENTS | vii |
| FIGURES | ix |
| TABLES | xiv |
| CHAPTER 1 INTRODUCTION | 1 |
| CHAPTER 2 LITERATURE REVIEW | 4 |
| 2.1 MECHANICAL AND CRYSTALLOGRAPHIC ANISOTROPY | 4 |
| 2.2 TEXTURE | 6 |
| 2.2.1 WAYS OF MEASURING TEXTURE | 7 |
| 2.2.2 KEARN'S NUMBER (f) | 10 |
| 2.3 MECHANICAL ANISOTROPY | 14 |
| 2.3.1 WAYS OF MEASURING MECHANICAL ANISOTROPY | 14 |
| 2.3.2 THE FLOW SURFACE | 15 |
| 2.3.3 THE YIELD CRITERION | 19 |
| 2.3.4 KNCOP MICROHARDNESS FLOW SURFACE | 21 |
| 2.4 THERMOELECTRIC POWER (TEP) | 24 |
| 2.5 HEATING EFFECTS ON MICROSTRUCTURE AND ANISOTROPY | 27 |
| 2.6 SUMMARY OF PREVIOUS WORK ON TEXTURE AND MICROHARDNESS | 30 |
| CHAPTER 3 EXPERIMENTAL DETAILS | 43 |
| 3.1 MATERIALS | 43 |

| | |
|--|-----|
| 3.2 HEAT TREATMENTS | 43 |
| 3.3 THERMOELECTRIC POWER (TEP) MEASUREMENTS | 44 |
| 3.4 RING TENSILE TEST | 44 |
| 3.5 MICROHARDNESS MEASUREMENTS AND OPTICAL METALLOGRAPHY | 45 |
| 3.5.1 CONSTRUCTION OF THE KNOOP HARDNESS FLOW SURFACE | 46 |
| 3.6 TEXTURE MEASUREMENTS | 51 |
| 3.6.1 CALCULATION OF f-PARAMETER | 52 |
| | |
| CHAPTER 4 EXPERIMENTAL RESULTS | 63 |
| | |
| 4.1 MICROHARDNESS MEASUREMENTS | 63 |
| 4.1.1 FLOW SURFACE DIAGRAMS | 63 |
| 4.1.2 ANISOTROPY RATIO | 65 |
| 4.1.3 KHN VERSUS ANNEALING TEMPERATURE | 66 |
| 4.2 TEXTURE | 68 |
| 4.3 THERMOELECTRIC POWER (TEP) | 70 |
| 4.4 OPTICAL METALLOGRAPHY | 71 |
| 4.5 OXYGEN EFFECTS | 73 |
| 4.6 RING TENSILE TEST | 74 |
| | |
| CHAPTER 5 DISCUSSION | 139 |
| | |
| CHAPTER 6 CONCLUSIONS AND RECOMMENDATIONS | 151 |
| | |
| 6.1 CONCLUSIONS | 151 |
| 6.2 RECOMMENDATIONS | 154 |
| | |
| REFERENCES | 156 |
| | |
| BIBLIOGRAPHY | 158 |
| | |
| APPENDIX | 162 |
| | |
| VITA AUCTORIS | 165 |

FIGURES

- 2.1 Schematic diagram showing the orientation of the hexagonal prism for a bimodal distribution in a tubing. 31
- 2.2 (0001) poles of random sample intersecting the reference sphere. 32
- 2.3 Schematic diagram showing the relationship between an (hkil) pole, the basal pole (0001), the tilt angle ϕ , and the sample surface. 33
- 2.4 Standard projection of diffracting planes of α -Zirconium. 34
- 2.5 Schematic diagram showing a general three-dimensional state of stress. 35
- 2.6 Schematic diagram showing the three principal stresses resulted by a rotation of the cube element in figure 2.5. 36
- 2.7 Schematic diagram showing the direction of the hydrostatic and the deviatoric stresses on a yield prism. 37
- 2.8 Schematic diagram showing the Knoop indenter impression and coordinates. 38
- 2.9 Schematic diagram showing the relationship between Knoop indenter orientations and deviatoric stress ratios. 39
- 2.10 Schematic diagram showing the directions corresponding to the different Knoop indenter orientations on a π -plane. 40
- 2.11 The binary Zr-Sn phase diagram. 41
- 2.12 A typical curve showing the effect of annealing temperature and duration on grain size. 42
- 3.1 Schematic diagram showing experimental set-up for

| | |
|--|----|
| thermoelectric power (TEP) measurements. | 55 |
| 3.2 Schematic diagram showing tensile grips for ring sample. | 56 |
| 3.3 "Basic" computer program for calculation of the anisotropy coefficients. | 57 |
| 3.4 (a) Schematic diagram of the hexagonal prism and the tilt angle (ϕ) between the major (hkil) planes and the basal plane; (b) standard stereographic projection for α -Zr showing the positions of the major (hkil) poles and the rotation angle α . | 59 |
| 3.5 "Basic" computer program for calculation of the f-parameter. | 60 |
| 4.1 Flow surface diagram for Zircaloy-4 tubing in the as-received condition. | 75 |
| 4.2 Flow surface diagram for Zircaloy-4 tubing annealed at 300°C for 10 ³ seconds. | 76 |
| 4.3 Flow surface diagram for Zircaloy-4 tubing annealed at 400°C for 10 ³ seconds. | 77 |
| 4.4 Flow surface diagram for Zircaloy-4 tubing annealed at 500°C for 10 ³ seconds. | 78 |
| 4.5 Flow surface diagram for Zircaloy-4 tubing annealed at 600°C for 10 ³ seconds. | 79 |
| 4.6 Flow surface diagram for Zircaloy-4 tubing annealed at 700°C for 10 ³ seconds. | 80 |
| 4.7 Flow surface diagram for Zircaloy-4 tubing annealed at 800°C for 10 ³ seconds. | 81 |
| 4.8 Flow surface diagram for Zircaloy-4 tubing annealed at 900°C for 10 ³ seconds. | 82 |
| 4.9 Flow surface diagram for Zircaloy-4 tubing annealed at | |

| | |
|---|----|
| 1000°C for 10 ³ seconds. | 83 |
| 4.10 Flow surface diagram for Zircaloy-4 tubing annealed at 300°C for 10 ⁴ seconds. | 84 |
| 4.11 Flow surface diagram for Zircaloy-4 tubing annealed at 400°C for 10 ⁴ seconds. | 85 |
| 4.12 Flow surface diagram for Zircaloy-4 tubing annealed at 500°C for 10 ⁴ seconds. | 86 |
| 4.13 Flow surface diagram for Zircaloy-4 tubing annealed at 600°C for 10 ⁴ seconds. | 87 |
| 4.14 Flow surface diagram for Zircaloy-4 tubing annealed at 700°C for 10 ⁴ seconds. | 88 |
| 4.15 Flow surface diagram for Zircaloy-4 tubing annealed at 800°C for 10 ⁴ seconds. | 89 |
| 4.16 Flow surface diagram for Zircaloy-4 tubing annealed at 900°C for 10 ⁴ seconds. | 90 |
| 4.17 Flow surface diagram for Zircaloy-4 tubing annealed at 1000°C for 10 ⁴ seconds. | 91 |
| 4.18 Flow surface diagram for Zircaloy-4 tubing annealed at 300°C for 10 ⁵ seconds. | 92 |
| 4.19 Flow surface diagram for Zircaloy-4 tubing annealed at 400°C for 10 ⁵ seconds. | 93 |
| 4.20 Flow surface diagram for Zircaloy-4 tubing annealed at 500°C for 10 ⁵ seconds. | 94 |
| 4.21 Flow surface diagram for Zircaloy-4 tubing annealed at 600°C for 10 ⁵ seconds. | 95 |
| 4.22 Flow surface diagram for Zircaloy-4 tubing annealed at 700°C for 10 ⁵ seconds. | 96 |

| | |
|--|-----|
| 4.23 Flow surface diagram for Zircaloy-4 tubing annealed at 800°C for 10 ⁵ seconds. | 97 |
| 4.24 Flow surface diagram for Zircaloy-4 tubing annealed at 900°C for 10 ⁵ seconds. | 98 |
| 4.25 Flow surface diagram for Zircaloy-4 tubing annealed at 1000°C for 10 ⁵ seconds. | 99 |
| 4.26 The mechanical anisotropy ratio, for Zircaloy-4 tubing, vs. annealing temperature for 10 ³ seconds annealing time. | 100 |
| 4.27 The mechanical anisotropy ratio, for Zircaloy-4 tubing, vs. annealing temperature for 10 ⁴ seconds annealing time. | 101 |
| 4.28 The mechanical anisotropy ratio, for Zircaloy-4 tubing, vs. annealing temperature for 10 ⁵ seconds annealing time. | 102 |
| 4.29 KHN, in major directions, vs. annealing temperature for Zircaloy-4 tubing for an annealing time of 10 ³ seconds. | 103 |
| 4.30 KHN, in major directions, vs. annealing temperature for Zircaloy-4 tubing for an annealing time of 10 ⁴ seconds. | 104 |
| 4.31 KHN, in major directions, vs. annealing temperature for Zircaloy-4 tubing for an annealing time of 10 ⁵ seconds. | 105 |
| 4.32 The f-parameter, in major directions, vs. annealing temperature for Zircaloy-4 tubing for an annealing time of 10 ³ seconds. | 106 |
| 4.33 The f-parameter, in major directions, vs. annealing temperature for Zircaloy-4 tubing for an annealing time of 10 ⁴ seconds. | 107 |
| 4.34 The f-parameter, in major directions, vs. annealing temperature for Zircaloy-4 tubing for an annealing time of 10 ⁵ seconds. | 108 |

| | |
|---|-----|
| 4.35 TEP vs. annealing temperature for Zircaloy-4 for an annealing time of 10^3 , 10^4 and 10^5 seconds. | 109 |
| 4.36 Optical micrograph of Zircaloy-4 tubing in the as-received condition (using polarized light). | 110 |
| 4.37 Optical micrograph of Zircaloy-4 annealed at 500°C for 10^3 seconds (using polarized light). | 111 |
| 4.38 Optical micrograph of Zircaloy-4 annealed at 500°C for 10^4 seconds (using polarized light). | 112 |
| 4.39 Optical micrograph of Zircaloy-4 annealed at 500°C for 10^5 seconds (using polarized light). | 113 |
| 4.40 Optical micrograph of Zircaloy-4 annealed at 600°C for 10^3 seconds (using polarized light). | 114 |
| 4.41 Optical micrograph of Zircaloy-4 annealed at 600°C for 10^4 seconds (using polarized light). | 115 |
| 4.42 Optical micrograph of Zircaloy-4 annealed at 600°C for 10^5 seconds (using polarized light). | 116 |
| 4.43 Optical micrograph of Zircaloy-4 annealed at 800°C for 10^3 seconds (using polarized light). | 117 |
| 4.44 Optical micrograph of Zircaloy-4 annealed at 800°C for 10^4 seconds (using polarized light). | 118 |
| 4.45 Optical micrograph of Zircaloy-4 annealed at 800°C for 10^5 seconds (using polarized light). | 119 |
| 4.46 Optical micrograph of Zircaloy-4 annealed at 900°C for 10^3 seconds (using polarized light). | 120 |
| 4.47 Optical micrograph of Zircaloy-4 annealed at 900°C for 10^4 seconds (using polarized light). | 121 |
| 4.48 Optical micrograph of Zircaloy-4 annealed at 900°C for | |

| | |
|---|-----|
| 10 ⁵ seconds (using polarized light). | 122 |
| 4.49 Optical micrograph of Zircaloy-4 annealed at 1000°C for 10 ³ seconds (using polarized light). | 123 |
| 4.50 Optical micrograph of Zircaloy-4 annealed at 1000°C for 10 ⁴ seconds (using polarized light). | 124 |
| 4.51 Optical micrograph of Zircaloy-4 annealed at 1000°C for 10 ⁵ seconds (using polarized light). | 125 |
| 5.1 A schematic diagram showing the effect of annealing temperature on the Zircaloy-4 fuel tubing. | 149 |

TABLES

| | |
|---|-----|
| 3.1 Chemical analysis for Zircaloy-4 fuel tubing. | 62 |
| 4.1 KHN in major directions for various heat treatment conditions for Zircaloy-4 tubing. | 126 |
| 4.2 KHN, in major directions, and mechanical anisotropy ratio for Zircaloy-4 tubing annealed at various temperatures for 10 ³ seconds. | 127 |
| 4.3 KHN, in major directions, and mechanical anisotropy ratio for Zircaloy-4 tubing annealed at various temperatures for 10 ⁴ seconds. | 128 |
| 4.4 KHN, in major directions, and mechanical anisotropy ratio for Zircaloy-4 tubing annealed at various temperatures for 10 ⁵ seconds. | 129 |
| 4.5 The f-parameter, in major directions, at different annealing temperatures for 10 ³ seconds for Zircaloy-4 tubing. | 130 |

| | | |
|------|--|-----|
| 4.6 | The f-parameter, in major directions, at different annealing temperatures for 10^4 seconds for Zircaloy-4 tubing. | 131 |
| 4.7 | The f-parameter, in major directions, at different annealing temperatures for 10^5 seconds for Zircaloy-4 tubing. | 132 |
| 4.8 | TEP values at different annealing temperatures for 10^3 seconds for Zircaloy-4 tubing. | 133 |
| 4.9 | TEP values at different annealing temperatures for 10^4 seconds for Zircaloy-4 tubing. | 134 |
| 4.10 | TEP values at different annealing temperatures for 10^5 seconds for Zircaloy-4 tubing. | 135 |
| 4.11 | Grain size for Zircaloy-4 tubing after various heat treatments. | 136 |
| 4.12 | Oxygen content (in ppm by weight) of Zircaloy-4 tubing in the as-received condition and after various heat treatments. | 137 |
| 4.13 | The yield strength in the tangential direction for Zircaloy-4. | 138 |
| 5.1 | Predicted and measured yield strength values for Zircaloy-4. | 150 |

CHAPTER 1

INTRODUCTION

In 1949 zirconium was used for the first time as a structural material for the nuclear reactors of submarines. In the 1950's, zirconium became available outside government programs and the chemical process industry began to use it in a variety of severe corrosion environments. Although many of the first commercial power reactors used stainless steel to clad the uranium dioxide fuel, this changed by the middle 1960's and zirconium alloys became the main cladding materials for the water-cooled reactors.

Although many zirconium alloy systems have been studied for potential usage in nuclear systems, only a few of them are of commercial importance. The most common in use today in nuclear applications are Zircaloy-2, Zircaloy-4, and Zr-2.5wt% Nb. Zircaloy is a generic term for a series of zirconium-tin alloys containing minor amounts of Fe, Cr and Ni which were developed by the US Navy Nuclear Propulsion Program for

nuclear applications.

Thin-walled zirconium alloy tubing is widely used as a cladding material for the uranium fuel in nuclear power reactors. Zircaloy-4 is one of the most common zirconium alloys used in the PWR's (Pressurized Water Reactor) and the BWR's (Boiling Water Reactor) because it provides a low neutron absorption per unit of strength and a good corrosion resistance.

Zircaloy-4 remains in the hexagonal α -phase up to a temperature of about 870°C. Because of this crystallographic structure, anisotropic behaviour is expected. A strong crystallographic texture causes a pronounced anisotropy in the mechanical properties of the tubing which will affect the behaviour of the nuclear fuel elements in the reactor; therefore, the tubing texture must be specified and measured. The Zircaloy-4 fuel cladding is used in the cold-worked or cold-worked and stress relieved conditions. As a result of long term exposure at a reactor operating temperature of about 300°C or temperature transient experienced during such occurrences as a postulated loss-of-coolant accident, LOCA, where temperatures can reach a 1000°C, the fuel cladding could experience

texture and hence property, changes. The mechanical anisotropy of zirconium base alloys has been studied extensively in the past but there is little indication of how this anisotropy is related to texture. The aim of the present study is to follow the changes in anisotropy produced by annealing at different temperatures from 300°C to 1000°C for different annealing times (10^3 , 10^4 , and 10^5 seconds) using Knoop microhardness, x-ray texture measurement, optical metallography, and thermoelectric power measurements. The Knoop microhardness measurements are used as means of measuring the mechanical anisotropy non-destructively. These microhardness measurements were then compared to tensile test measurements made using ring samples.

CHAPTER 2

LITERATURE REVIEW

2.1 MECHANICAL AND CRYSTALLOGRAPHIC ANISOTROPY

If a metal exhibits the same properties in all directions it is said to be "isotropic". If the properties are different in different directions, the metal is said to be "anisotropic". Metals may be isotropic or anisotropic with respect to any type of behaviour, such as thermal conductivity, electrical resistivity, coefficient of expansion, plastic deformation, or fracture.

For different metals and different fabrication methods the degree of anisotropy will vary between wide limits: some metals are so nearly isotropic that it may be difficult to detect the difference in properties in different directions; other metals may be highly anisotropic.

Single crystals in general are distinguished by a marked anisotropy in their physicochemical properties. In the case of metals, this anisotropy is

most evident in crystals where planes and rows of closest atomic packing are well delineated, as in hexagonal close-packed structures. The variations in packing density as we view the crystal from different directions lead, in turn, to variations in the cohesive force from which the symmetry of the lattice can be determined. Thus, for example, a three dimensional plot of the elastic modulus will display the underlying lattice symmetry in much the same way as would the bounding faces on a perfectly developed crystal.

From an engineering point of view we are not concerned with the anisotropy of single crystals as such, because single crystals are not generally used in structural applications, but we are concerned with the anisotropy of single crystals insofar as it causes anisotropy of polycrystalline engineering materials in which the fabrication process has caused all the individual crystals to be oriented similarly. This condition of non-random orientation of the grains is referred to as "preferred orientation" or "texture" and is studied by means of x-ray diffraction. In the most extreme case, all the grains would have exactly the same orientation, and the polycrystalline aggregate would then be expected to exhibit the same degree of anisotropy as a single crystal of the same

material. A high degree of crystallographic anisotropy usually causes a high degree of mechanical anisotropy.

Crystallographic anisotropy induced by the cold-working operation is directly related to the resulting mechanical anisotropy . However, recrystallization during annealing changes this deformation texture and the form of mechanical anisotropy, but, generally, will not produce isotropy.

2.2 TEXTURE

The anisotropy of zirconium single crystals is present in the polycrystalline metal, which normally is heavily textured and has anisotropic properties. This is of special importance to the mechanical properties of Zircaloy-4 tubes in their use as fuel sheathing in nuclear reactors.

Hexagonal close-packed (hcp) α -zirconium (below approximately 850°C) has a crystal lattice with a unique direction, the basal plane normal or the basal pole [0001], and (0001) is the slip plane. Plastic deformation in α -Zr occurs either by slip or twinning. The slip systems are of the type $\{10\bar{1}0\}\langle 1\bar{2}10\rangle$ with all slip directions perpendicular to the [0001]. Thus,

tension or compression along [0001] cannot be accommodated by slip. Instead, twinning occurs and this requires a higher resolved shear stress than slip, making [0001] a stronger direction of the crystal.

The thermomechanical processing of the hexagonal close-packed Zircalloys from ingot into tubing results in the development of a strong crystallographic texture. The most commonly observed texture⁽¹⁾ of the final tubing is a bimodal distribution of the basal poles concentrated in the radial-tangential (R- θ) plane of the tube (Fig.2.1) with the maximum intensity at angles of plus and minus 30° to 40° from the radial direction. However, a wide range of less common textures is also observed depending, particularly, on the cold reduction process followed during the manufacturing operation.

2.2.1 WAYS OF MEASURING TEXTURE

Crystallographic texture is most often characterized by constructing a direct pole figure or an inverse pole figure from x-ray diffraction data. Comparison of pole figures and inverse pole figures can be difficult. This led to the development of different texture numbers in order to allow a simple quantitative comparison. Such numbers are the F-factor which was

originally defined by Kallstrom⁽²⁾ and the f-parameter which was originally defined by Kearns⁽³⁾. The f-parameter is widely used in the nuclear industry to characterize the texture of the zirconium fuel sheathing. These techniques are briefly discussed below.

A full pole figure^(4,5) is a stereographic projection showing the intensity of normals to a " specific " plane in all directions. To plot a full pole figure, intensity maxima on a single diffraction ring (Debye ring) are plotted on a single reflection circle on the pole figure. A series of diffraction patterns with the specimen tilted by some angular increment must be taken to cover the whole projection.

An inverse pole figure, on the other hand, is a stereographic projection showing the intensities of "all" planes in a specific direction. Harris⁽⁶⁾ introduced this technique which incorporates in a single diagram all the information given conventionally in pole charts for various (hkl) reflections and, therefore, it represents a considerable degree of condensation. To plot an inverse pole figure, the intensities from the sample are compared with those from a randomly oriented sample (grains are randomly oriented). Then a texture coefficient (T.C.) for each (hkl) is

calculated using the equation :

$$T.C._i = (I_i / I'_i) / [(1/n) * \Sigma (I_i / I'_i)] \quad 2.1$$

Where I_i is the intensity of the i^{th} reflection for the textured sample, and I'_i is the intensity of the i^{th} reflection from the randomly oriented sample. These T.C. values are then entered on a stereographic projection .

A fuller description of the anisotropy of textured metals is obtained by using the crystalline orientation distribution function^(7,8) (CODF). The CODF gives the probability of crystallite having an orientation described by the Euler angles (ϕ, θ , and ψ), and a series of generalized spherical harmonics. The analysis in terms of CODF are generally presented by plotting the probability contours of a crystallite having a given orientation in the Eulerian space at a constant ϕ sections. Calculations of CODF are rather laborious and involve the use of pole figure intensity data.

The texture factor^(1,2), F , which was defined by Kallstrom, is the normalized weighted average of the basal poles in the investigated plane of the tube. The direct pole figure⁽⁴⁾ intensity data are used to calculate F

according to the formula:

$$F = \int_{-\pi/2}^{\pi/2} I(\phi) \cos(\phi) d\phi / \int_{-\pi/2}^{\pi/2} I(\phi) d\phi \quad 2.2$$

Where $I(\phi)$ is the integrated plane intensity distribution as a function of tilt angle ϕ measured from the radial direction. It should be noted that in the definition of the texture factor F , only the basal poles in the investigated plane of the tube are considered, whereas, Kearns' number (the f -parameter) basal poles in all directions are considered, as discussed in detail below.

2.2.2 KEARN'S NUMBER (f)

The concept of the f -parameter⁽³⁾ was originally conceived as a single-number quantity from which physical properties in polycrystalline material could be calculated from single crystal values. The concept of the f -parameter may also be used as a quantitative index of the effective texture, where the single f number represents the effective fraction of basal poles aligned in any one reference direction.

The orientation parameter f is defined as :

$$f = \sum V_{\phi}^f \cos^2 \phi$$

2.3

where V_{ϕ}^f is the volume fraction of crystals with their basal poles [0001] oriented at a tilt angle, ϕ , to the reference direction, and the summation from $\phi = 0$ to $\phi = \pi/2$ gives the effective contribution of these grains to the gross texture in the reference direction, the reference direction being the normal to the plane facing the x-ray beam in a diffractometer scan.

As indicated by equation 2.3, to calculate "f" one must first evaluate V_{ϕ}^f , that is, the number of [0001] poles as a function of their tilt to the reference direction. This can be derived from conventional (0001) pole figure data. Figure 2.2 shows a random distribution of (0001) poles intersecting the reference sphere. The angle ϕ defines the tilt of (0001) poles to the reference direction; α defines directions in the reference plane. However, only the pole density, $I(\phi)$, averaged over 360° of α is required in the calculation of f (equation 2.3), so the pole density as a function of α need not be known. To evaluate V_{ϕ}^f as a function of ϕ , one must evaluate the volume of metal in each of series of $\Delta\phi$ bands from $\phi = 0$ to $\phi = \pi/2$. The volume of metal in each band is proportional to the number

of poles in the band. From the geometry in Figure 2.2, it can be seen that the size of the band is proportional to its circumference which, in turn, is proportional to $\sin \phi$. Therefore, the volume of metal in a $\Delta\phi$ is proportional to $I(\phi) \sin \phi \Delta\phi$. The volume fraction V_{ϕ}^f can then be calculated from:

$$V_{\phi}^f = \left[\int_{\phi_1}^{\phi_2} I(\phi) \sin \phi \, d\phi \right] / \left[\int_0^{\pi/2} I(\phi) \sin \phi \, d\phi \right] \quad 2.4$$

where the integral in the denominator represents the total number of basal poles [0001] in a given volume of the sample. When the average basal pole density in any $\Delta\phi$ band, $I(\phi)$, is expressed as a fraction of the basal pole density in the same $\Delta\phi$ band of a random sample (Random=1), this integral equals "unity". The expression for f in equation 2.3 may now be expressed in an integral form as

$$f = \int_0^{\pi/2} I(\phi) \sin \phi \cos^2 \phi \, d\phi \quad 2.5$$

In a tubing, calculation of "f" resolves the ordinary scatter of [0001] orientations into an effective fraction aligned in each of the three principal tubing directions (radial, axial, and tangential direction). Values of "f" of

0 and 1 indicate perfect alignment of the [0001] crystal directions perpendicular and parallel, respectively, to the reference direction. A value of 1/3 in each of the principal directions defines the isotropic case and the sum of the "f" numbers in these directions is theoretically equal to unity, irrespective of the anisotropy in any one direction.

The orientation distribution curve, $I(\phi)$, can be calculated from conventional pole figure data. However, it is laborious to obtain complete pole figure data and actually is unnecessary. The $I(\phi)$ versus ϕ curve can be evaluated much easier from intensity analysis in an ordinary diffractometer scan. To understand how the desired data may be derived from peak intensities, it is first necessary to examine some of the factors which influence the diffractometer trace. The geometric relationship between the x-ray beam, the sample surface, and the detector is of prime importance. These are arranged in a way so that as a scan of θ (Bragg angle) is made, only crystal planes parallel to the plane of the sample surface contribute to the measured diffracted intensity. Thus, the measured intensity of any [hkil] pole, having a tilt angle ϕ from the basal pole [0001], represents the intensity of the basal pole [0001] at an angle ϕ from the reference direction (see Fig. 2.3).

Measurement of the intensity, I , for all of the $(hkil)$ peaks of a test sample, and comparison with the corresponding intensities, I° , for a random sample, will therefore indicate the preferred orientation existing in the test sample. However, this method does not account for all the $[0001]$ pole orientations, since only those discrete orientations corresponding to the diffraction planes of α -zirconium are measurable. These orientations are shown on the (0001) standard projection of α -zirconium in Figure 2.4. The angle ϕ is the tilt of a diffraction pole from the basal pole. The angle α indicates a pole rotation about the basal pole. The detailed calculation of the f -parameter is reviewed in Chapter 3.

2.3 MECHANICAL ANISOTROPY

2.3.1 WAYS OF MEASURING MECHANICAL ANISOTROPY

The need to predict the mechanical behaviour of the fuel cladding material in a nuclear reactor has stimulated new interest in the measurement of mechanical anisotropy.

A simple way to predict yielding in different directions of a tubing, is by conducting tensile tests⁽⁹⁾ in different directions. This, however, is limited by the geometry of the tubing; for example, it is not practical to

conduct a tensile test along the thickness of the tubing.

A closed-end burst test⁽¹⁰⁾ is sometimes used to predict the behaviour of the tubing under biaxial loading. This is done by hydraulically pressurizing the closed-end tubing and measuring the strains in the axial and tangential directions. This test gives the yield stress only in one direction of the tubing .

A ring test⁽⁹⁾ is also used . This is simply done by loading a small ring with a certain width to thickness ratio. This test, as the closed-end burst test, gives the yield point only in one direction.

Usually a combination of the above mentioned tests is conducted to give some information about the mechanical anisotropy of the tubing. In fact, these tests are done as a verification of the yield surface obtained from Knoop microhardness measurements^(10,11) discussed in the next section.

2.3.2 THE FLOW SURFACE

The flow surface, sometimes referred to as the yield surface, is the boundary of the elastic domain and it is path-dependent in the sense that

a point on it may be approached by many different loading paths within the elastic region .

In general, the state of stress at a point in a body is specified by values of the six independent stress components, σ_1 , σ_2 , σ_3 , τ_{23} , τ_{31} , and τ_{12} , referred to an arbitrary set of orthogonal, 1, 2, and 3 axes (see Fig. 2.5). It might appear, therefore, that we would need a six dimensional stress space in which to represent a general flow surface. However, it is always possible to choose directions of orthogonal axes, x, y, and z, for which the shear stresses, τ_{yz} , τ_{zx} , and τ_{xy} , all equal to zero, as shown in Figure 2.6. These are called principal axes and the corresponding stresses (σ_x , σ_y , and σ_z) the principal stresses. It is, therefore, convenient to choose the principal axes as the reference axes, and this incurs no loss of generality.

First, we introduce the observation that the addition of an equal-all-around (hydrostatic) pressure to a specimen does not affect its yield behaviour, at least for pressures of the same order as the tensile yield stress. By this statement we mean that if the point $(\sigma_x, \sigma_y, \sigma_z) = (a, b, c)$ lies on the flow surface and so does the point $(a+h, b+h, c+h)$ for all h, at least within fairly wide limits. It follows that any point (a ,

b , c) on the flow surface generates a line passing through the point and parallel to the line $\sigma_x = \sigma_y = \sigma_z$, which is in the first octant of the principal stress space and equally inclined to all three principal stress axes. Hence, the flow surface is a prism which may be thought of as being generated by sliding a curve along the " space diagonal " $\sigma_x = \sigma_y = \sigma_z$.

This being so, all additional information necessary for us to specify the flow surface completely is the shape and the size of the cross section of the yield prism. Now, by elementary solid geometry, all planes perpendicular to the line $\sigma_x = \sigma_y = \sigma_z$ have the equation $\sigma_x + \sigma_y + \sigma_z = \text{constant}$. As it is immaterial which cross section of the prism we consider, we can set the constant to any arbitrary value. The most convenient value is zero, which corresponds to the plane perpendicular to the axis of the prism and passing through the origin of the principal stress space. This special plane is called the π -plane, and the intersection of the yield prism with it the C-curve.

It is a matter of elementary algebra to reduce any point on the flow surface to the corresponding point on the C-curve. Let (a,b,c) lie on the yield surface. The corresponding point on the C-curve has coordinates

(a-h,b-h,c-h) and in addition since it lies on the π -plane, the sum of the three principal stresses is zero ; so $h = (a+b+c)/3$. We can, thus, write for any point on the flow surface the identity

$$(\sigma_x, \sigma_y, \sigma_z) \equiv (\sigma'_x, \sigma'_y, \sigma'_z) + (\sigma_o, \sigma_o, \sigma_o) \quad 2.6$$

where

$$\sigma_o = (\sigma_x + \sigma_y + \sigma_z) / 3 \quad 2.7$$

and

$$\sigma'_x = \sigma_x - \sigma_o$$

$$\sigma'_y = \sigma_y - \sigma_o \quad 2.8$$

$$\sigma'_z = \sigma_z - \sigma_o$$

Note that $\sigma'_x + \sigma'_y + \sigma'_z \equiv 0$. The stresses $(\sigma'_x, \sigma'_y, \sigma'_z)$ are known as the " deviatoric " stresses or stress deviations, and σ_o is known the " hydrostatic " stress. In geometrical terms we have broken down the stress vector in three dimensional stress space into two components. One,

the deviatoric stress, lying in the π -plane, determines the shape of the flow surface and causes yielding, the other, hydrostatic stress, is perpendicular to the π -plane in the direction of the diagonal (see Fig. 2.7).

2.3.3 THE YIELD CRITERION

Hill⁽¹²⁾ has formulated a quantitative treatment of plastic anisotropy without regard to its crystallographic origin. He assumed a homogeneous material characterized by three orthogonal axes 1, 2, and 3. The theory also assumes that in any given direction the tensile and compressive yield strengths are equal.

The proposed anisotropy yield criterion has the form:

$$F(\sigma_2 - \sigma_3)^2 + G(\sigma_3 - \sigma_1)^2 + H(\sigma_1 - \sigma_2)^2 + 2L\tau_{23}^2 + 2M\tau_{31}^2 + 2N\tau_{12}^2 = 1 \quad 2.9$$

where F, G, H, L, M, and N are the constants which characterize the anisotropy. For principal axes (x, y, and z) where $\tau_{yz} = \tau_{zx} = \tau_{xy} = 0$, we have

$$F(\sigma_y - \sigma_z)^2 + G(\sigma_z - \sigma_x)^2 + H(\sigma_x - \sigma_y)^2 = 1 \quad 2.10$$

where σ_x , σ_y , and σ_z are principal stresses. This equation can be reduced to the isotropic case when

$$F = G = H = 1/(2\sigma_{\text{yield}}^2) \quad 2.11$$

where σ_{yield} is the yield stress in any direction. The isotropic case is the Von Mises yield criterion.

Consider a tensile test in the x-direction and let X be the yield stress in this direction. At yielding $\sigma_x=X$, $\sigma_y=\sigma_z=0$, and equation 2.10 now becomes $X^2*(G + H) = 1$. Similarly, if Y and Z are tensile yield stresses in the y and z directions, respectively, then

$$X^2 = 1 / (G + H)$$

$$Y^2 = 1 / (H + F)$$

$$Z^2 = 1 / (F + G)$$

2.12

Solving equations 2.12 simultaneously,

$$2F = (1/Y^2) + (1/Z^2) - (1/X^2)$$

$$2G = (1/Z^2) + (1/X^2) - (1/Y^2)$$

2.13

$$2H = (1/X^2) + (1/Y^2) - (1/Z^2)$$

Unfortunately, for sheet and thin tubing it is not convenient to measure Z directly. In Chapter 3 we will show how can this problem be overcome by means of Knoop microhardness measurements.

In geometrical terms the yield criterion, equation 2.10, represents an elliptical cylinder along the diagonal of the σ_x , σ_y , and σ_z principal axes. The intersection of this cylinder with the π -plane, the C-curve, is an ellipse (a circle for isotropic case).

2.3.4 KNOOP MICROHARDNESS FLOW SURFACE

Wheeler and Ireland⁽¹¹⁾ proposed a technique for using the anisotropy of Knoop microhardness in polycrystalline metals to determine a graphical representation of the metals resistance to plastic flow " flow surface " for all combinations of principal stresses. This powerful technique provides a rapid means of establishing a flow surface non-destructively.

The Knoop indenter coordinates (l , w , and h) are parallel, respectively, to the long diagonal, short diagonal, and the direction of the indenter penetration (Fig. 2.8). The Knoop hardness number (KHN) is defined as the ratio of the load (kg) applied to the indenter to the unrecovered area (mm^2). The six KHN's obtained when the indenter coordinates are parallel to the material axes are empirically representative of yield stresses when the ratio of the deviatoric stresses σ'_w to σ'_l is 7 to 1. The geometry of the Knoop indenter is such that the ratio of the principal deviatoric stresses σ'_w to σ'_l is 7 to 1. This ratio was selected because it produced flow surfaces similar in shape to flow surfaces determined by standard methods.

A material-KHN-flow surface is constructed from KHN values obtained on each of the three planes determined by the material principal axes. For Knoop indenter penetration of each of these planes, there are two orientations of the indenter where the indenter coordinates (h , w , and l) are parallel to the material axes. These six indenter orientations and the associated deviatoric stress ratios for a section of a tubing are shown in Figure 2.9. The R , θ , and Z are the material axes (in a tubing), where R is the radial direction, θ is the tangential direction, and Z is the axial

direction. Each of the six KHN values are located on the π -plane along the appropriate deviatoric-stress-ratio line at a distance (from the origin) directly proportional to the KHN value. The KHN-flow-surface is then formed by the closed smooth curve through the six KHN points. The directions of the six deviatoric-stress-ratio lines, a, b, c, d, e, and f, are determined by the 7 to 1 deviatoric stress ratio associated with each of the six Knoop indenter orientations. For example, Knoop indenter orientation "b" measures the hardness in direction "b" on the π -plane. The coordinates of direction "b" are in the ratio of 7θ to $1Z$ to $-8R$ ($-8R$ is determined from the fact that the sum of all three deviatoric stresses must be zero). Figure 2.10 shows the a, b, c, d, e, and f, directions on a π -plane.

The axes of anisotropy of zirconium alloy tubings are parallel to the material forming directions. The forming directions of extruded tubing are the radial, axial, and tangential directions.

Wheeler and Ireland⁽¹¹⁾ have shown that the flow surface constructed from microhardness data, for Zircaloy-2, is consistent with the results obtained from uniaxial tensile and close-end burst tests. Bera and Wright⁽¹⁰⁾ in their work on Zircaloy-4 tubing showed a good agreement between

KHN-flow-surface and the data from tensile and burst tests.

2.4 THERMOELECTRIC POWER (TEP)

The principal of the thermoelectric power is based on the Seebeck effect which states that "when two different metals are joined together at their ends to form a circuit, it is found that a current usually flows in the circuit if the two junctions are at different temperatures". Thus, a thermoelectromotive force develops between the two junctions. The thermoelectric power is a name given to the variation of the thermoelectromotive force per difference of temperature between the two junctions; thus, the relative TEP, ΔS , of the sample with respect to the reference metal (usually aluminum) is given by

$$\Delta S = \Delta V / \Delta T \quad 2.14$$

where ΔV is the thermoelectromotive force difference (voltage difference) between the two junctions and ΔT is the temperature difference, that is, one junction is at temperature T and the other is at temperature $T+\Delta T$. The absolute TEP, S_s , of the sample is given by

$$S_s = S_{ref} + \Delta S$$

2.15

where S_{ref} is the absolute TEP of the reference metal at the same temperature. As this TEP depends on temperature^(13,14), the temperature gradient, ΔT , must be chosen so that to ensure accurate measurement of ΔV , and also must be sufficiently low to give the isothermal value of S_s at the mean temperature of $T + \Delta T/2$.

The thermoelectric power of a material depends, primarily, on the chemical potential of the free electrons. The change in the chemical potential of the free electrons (which is a function of the Fermi level of the material) is caused by the existence of crystalline defects such as the displacement of ions by thermal oscillations (phonons), the presence of accidental impurities or solute atoms, imperfections such as dislocations, grain boundaries, stacking faults, vacancies, etc. Consequently, all the microstructural changes will be detected with thermoelectric power measurement. The thermoelectric power is, particularly, sensitive to deformation, recovery, recrystallization, and phase transformation. However, TEP is also sensitive to the amount of impurities, precipitation, and texture changes.

The TEP of hexagonal metals such as zirconium is anisotropic. As a consequence, the TEP of a textured sample will depend on the direction of measurement⁽¹⁵⁾. However, a study⁽¹⁶⁾ on Zircaloy-4 shows the same type of TEP evolution with annealing time regardless of the orientation of the sample with respect to the direction of measurement. That is, the "shape" of the TEP versus time curves is similar in all directions but they might shift upward or downward depending on the orientation of the sample with respect to the direction of measurement.

The thermoelectric power technique has recently been used in the nuclear industry to study the microstructure-property relationship of zirconium alloys fuel cladding material. A study⁽¹⁷⁾ on the annealing of Zr-1 wt% Nb showed that TEP measurements were, particularly, useful technique for studying the progress of recovery in cold-worked materials, a process which cannot be monitored by microhardness measurement. Recrystallization and phase changes were monitored by both TEP and microhardness measurement. Another study⁽¹⁸⁾ showed the dependence of thermoelectric power on the annealing temperature of cold-worked Zircaloy-4 fuel sheathing. In this study, changes in the microstructure due to recovery, recrystallization and phase changes were seen as changes in

the value of TEP.

2.5 HEATING EFFECTS ON MICROSTRUCTURE AND ANISOTROPY

In order to better understand the changes in the microstructure occurring on heating of Zircaloy-4 (Zr-1.5wt% Sn), it is useful to examine the Zr-Sn phase diagram. The hcp substitutional solid solution, α -zirconium, has a maximum solubility of 9.3wt% Sn at a temperature of 982°C of the peritectoid reaction (Fig. 2.11). The aging response of Zr-Sn alloys below the peritectoid reaction temperature and up to 9wt% Sn was studied⁽¹⁹⁾. Under most conditions of aging (including up to 1000 hours at temperatures in the range 500 to 600°C), following solution treatment in the α -Zr or β -Zr phases, minimal precipitation of second phase particles occurred. The stability of α -Zr was related, primarily, to the slow kinetics of phase decomposition.

For temperatures up to 870°C, Zircaloy-4 is composed only of α -zirconium. In the temperature range 870 to 890°C a two phase region exists, α -Zr (hcp) and β -Zr (bcc). The single phase β -Zr region extends from 890 to 1780°C.

The oxygen content of Zr-Sn alloys has an effect on the position of the transformation lines. Increasing the oxygen content is known to raise the α -Zr/ $(\alpha$ -Zr+ β -Zr) transformation temperature⁽²⁰⁾ for Zircaloy-4. Thus, oxygen is an α -stabilizer.

The microstructure and anisotropy which evolve upon heating can be characterized by many techniques, such as, optical microscopy, SEM, TEM, hardness, resistivity, x-ray, and TEP measurements. These techniques are used to monitor recovery, recrystallization, grain growth, phase transformation, precipitation, and texture changes.

A cold-worked material is in a state of considerable mechanical stress, resulting from internal elastic strains. If heated at relatively low temperatures atoms are able to move to positions nearer to equilibrium in the crystal lattice. Such small movements reduce local strains and therefore the mechanical stresses associated with them, without producing any visible change in the microstructure. Moreover, hardness and strength will remain at the high value produced by cold-work, and may even increase as in the case of cold-worked brass⁽²¹⁾. This process is known as recovery.

If the annealing temperature is further increased, a point is reached when new crystals begin to grow from nuclei produced in the deformed metal: this phenomenon is known as recrystallization. The recrystallization temperature depends, in part, on the amount of cold-work prior to annealing. The new crystals are equiaxed in form, that is, they do not show any elongation, as did the distorted cold-worked crystals which they replaced. These newly recrystallized crystals are soft and strain free. However, their strength would vary depending on the recrystallization texture developed and the mechanical anisotropy of these newly recrystallized grains.

If the annealing temperature is above the recrystallization temperature of the metal, the newly formed crystals will continue to grow by absorbing each other, until the structure becomes relatively coarse-grained. The extent of grain growth depends to a large degree on the annealing temperature used and the duration of the annealing process. Figure 2.12 shows that as the annealing temperature and duration increase⁽²¹⁾, the grain size also increases. The strength of the larger grain size material is lower than the fine grain size material. However grain growth will not generally produce

a significant change in anisotropy.

If the annealing temperature is increased above the transformation line, a second phase will form. The strength and anisotropy of the new structure will vary depending on many factors, such as, temperature and time of heating, cooling rate, and the microstructure of the transformed phase upon cooling.

2.6 SUMMARY OF PREVIOUS WORK ON TEXTURE AND MICROHARDNESS

A study^(22,23) on the annealing behaviour of Zr-1wt% Nb fuel cladding showed that as the annealing temperature is increased, the tubing becomes more mechanically and crystallographically isotropic. Also showed a significant drop in microhardness at the recrystallization temperature (~600°C) and a small change in texture, due to recrystallization, in the tangential direction. In an investigation⁽¹⁰⁾ on the effect of annealing temperature on the anisotropy of Zircaloy-4, the mechanical anisotropy was observed to be very high up to about 1000°C before a relatively sharp change occurred, leading to a substantially isotropic condition. In this study no attempt was made to relate the mechanical anisotropy to texture.

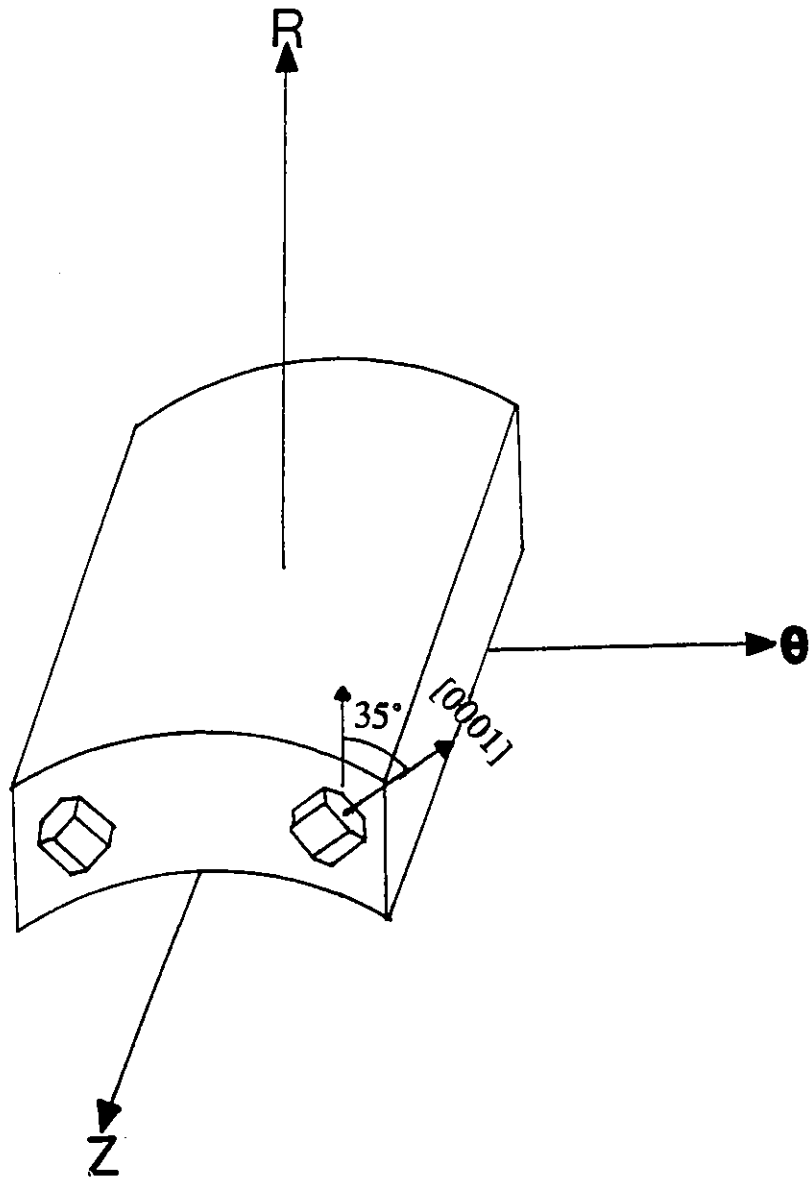


Figure 2.1 Schematic diagram showing the orientation of the hexagonal prism for a bimodal distribution in a tubing.

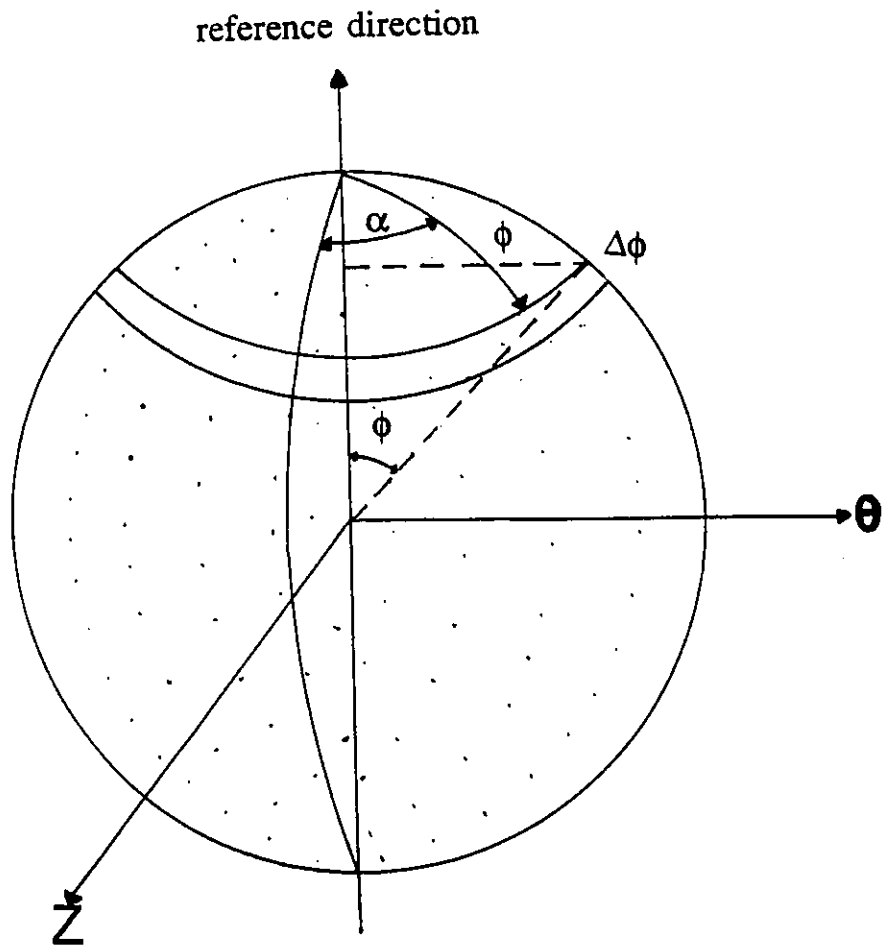


Figure 2.2 (0001) poles of random sample intersecting the reference sphere⁽³⁾.

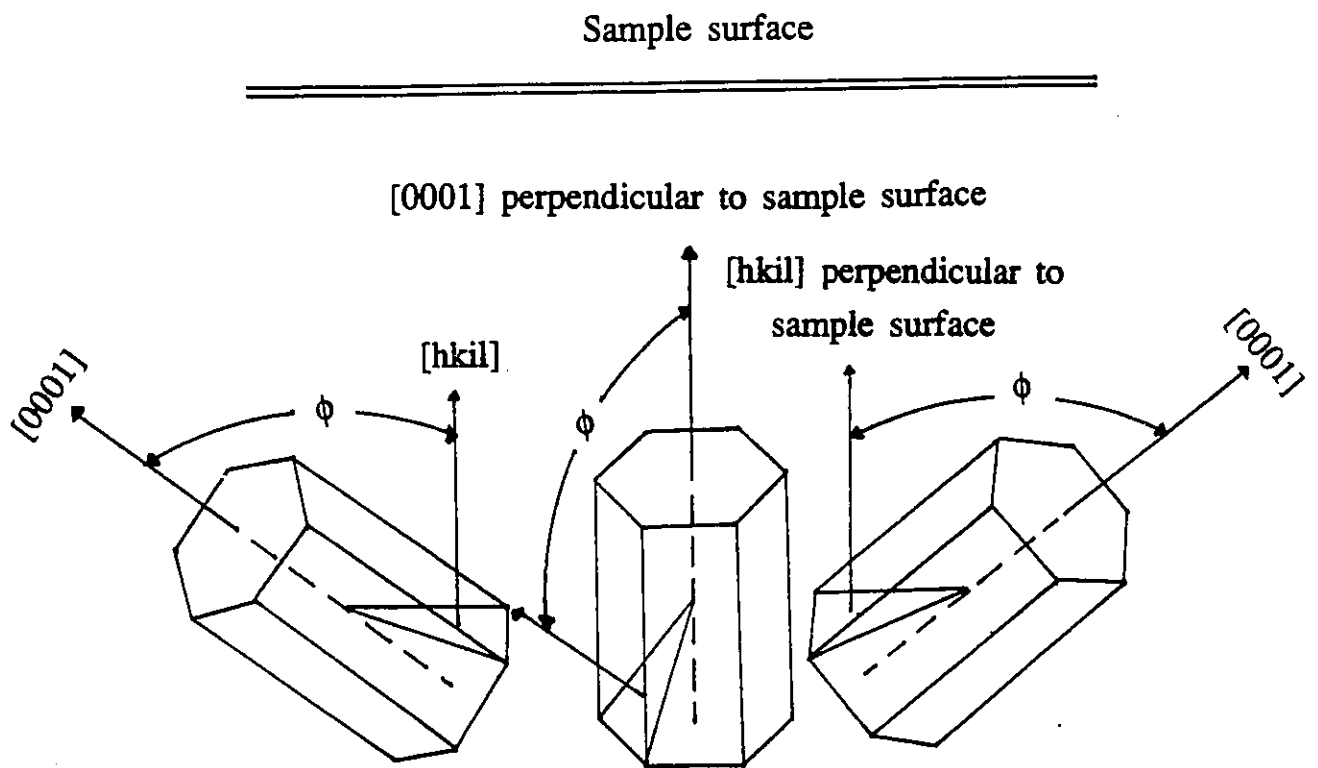


Figure 2.3 Schematic diagram showing the relationship between an (hkil) pole, the basal pole (0001), the tilt angle ϕ , and the sample surface.

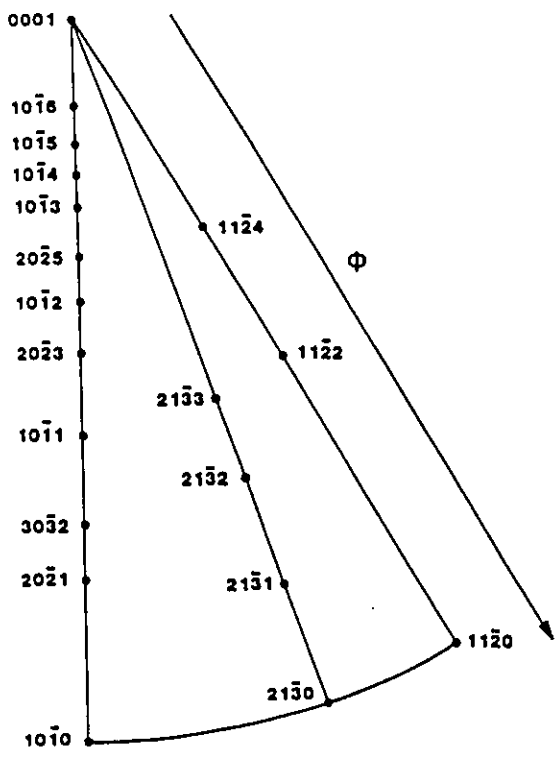


Figure 2.4 Standard projection of diffracting planes of α -Zirconium.

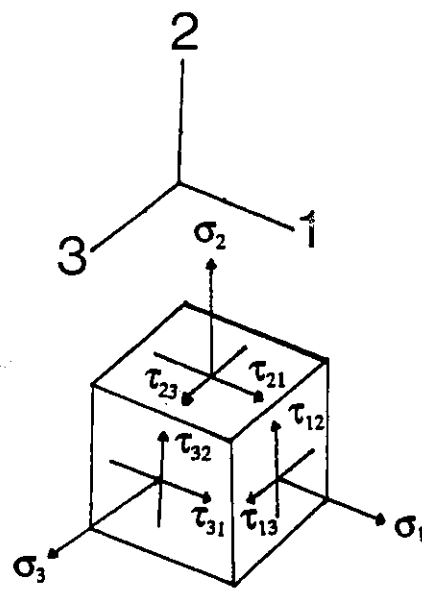


Figure 2.5 Schematic diagram showing a general three-dimensional state of stress.

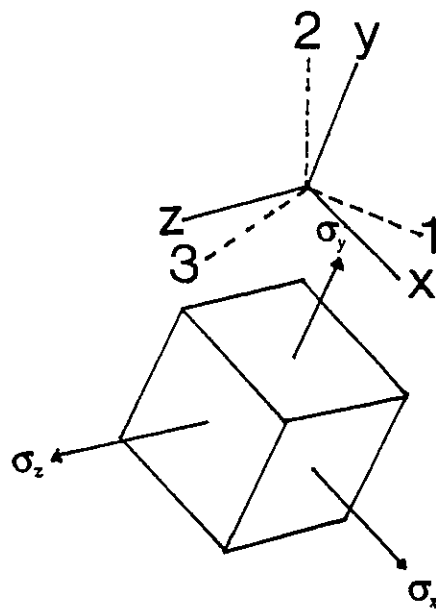


Figure 2.6 Schematic diagram showing the three principal stresses caused by a rotation of the cube element in figure 2.5.

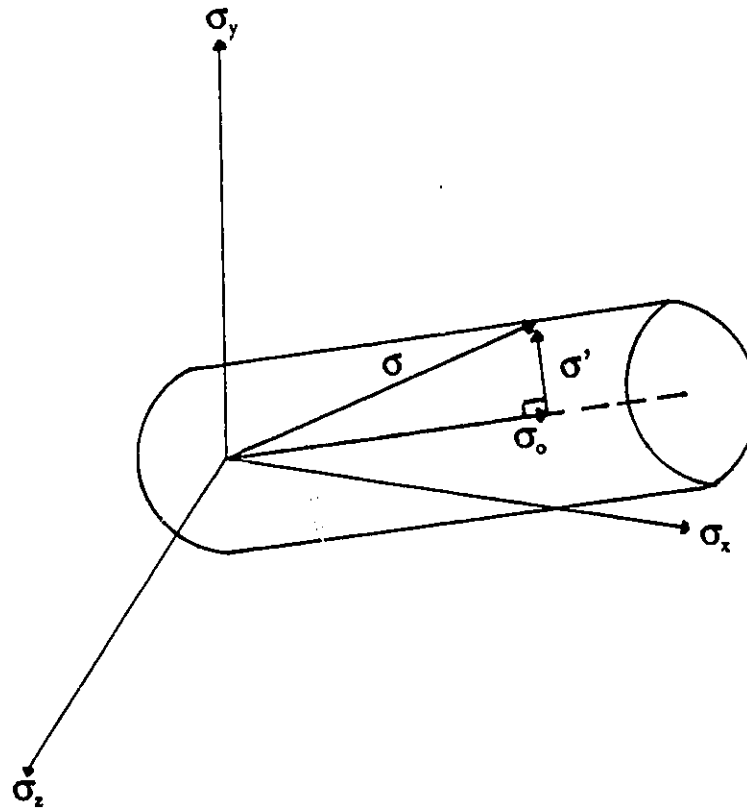


Figure 2.7 Schematic diagram showing the direction of the hydrostatic and the deviatoric stresses on a yield prism.

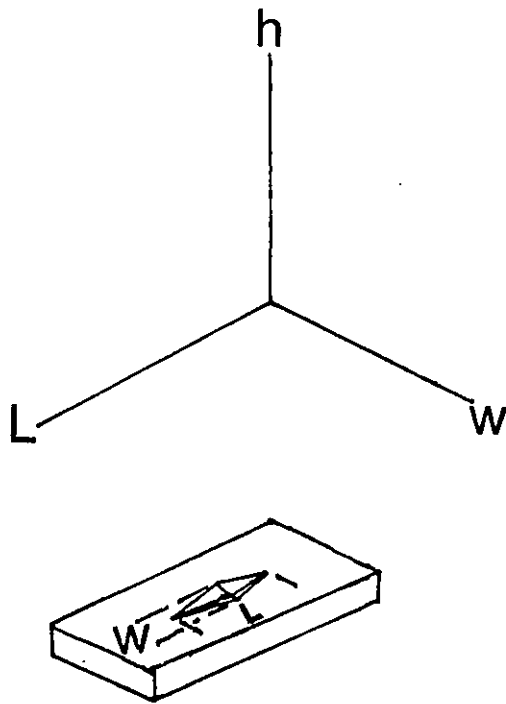


Figure 2.8 Schematic diagram showing the Knoop indenter impression and coordinates.

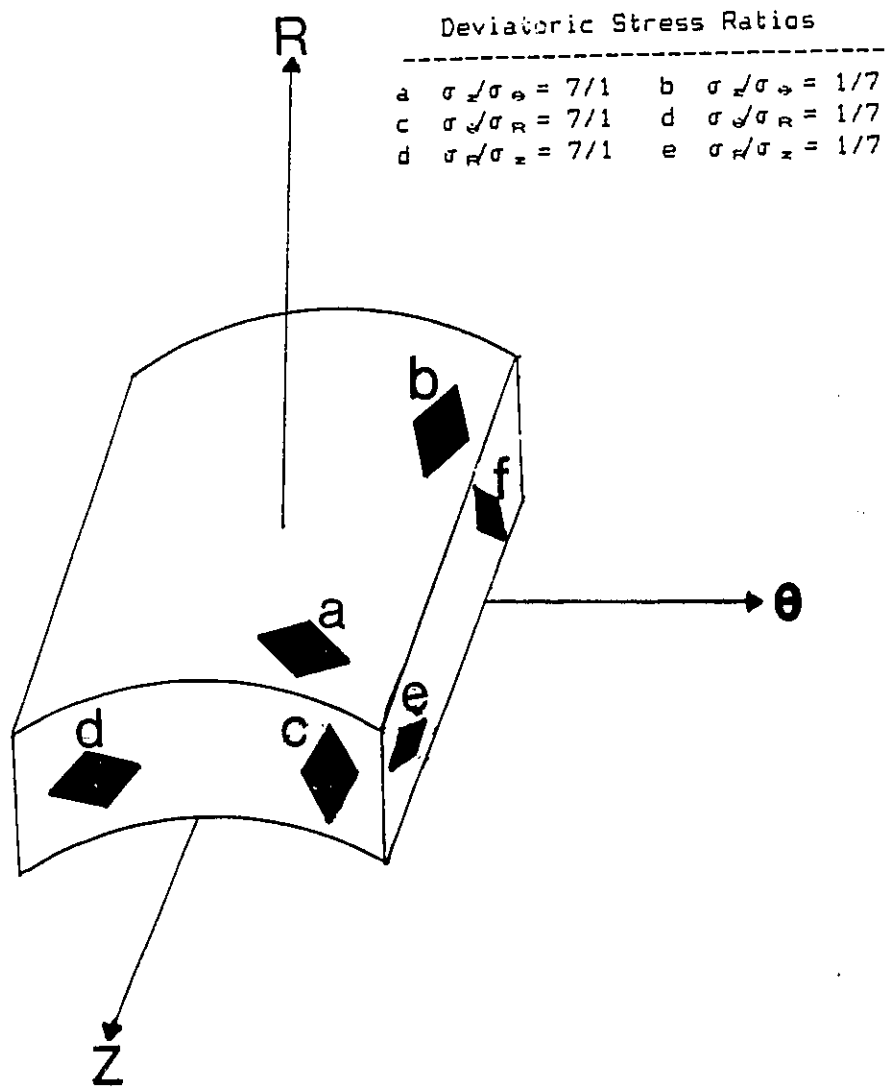


Figure 2.9 Schematic diagram showing the relationship between Knoop indenter orientations and deviatoric stress ratios.

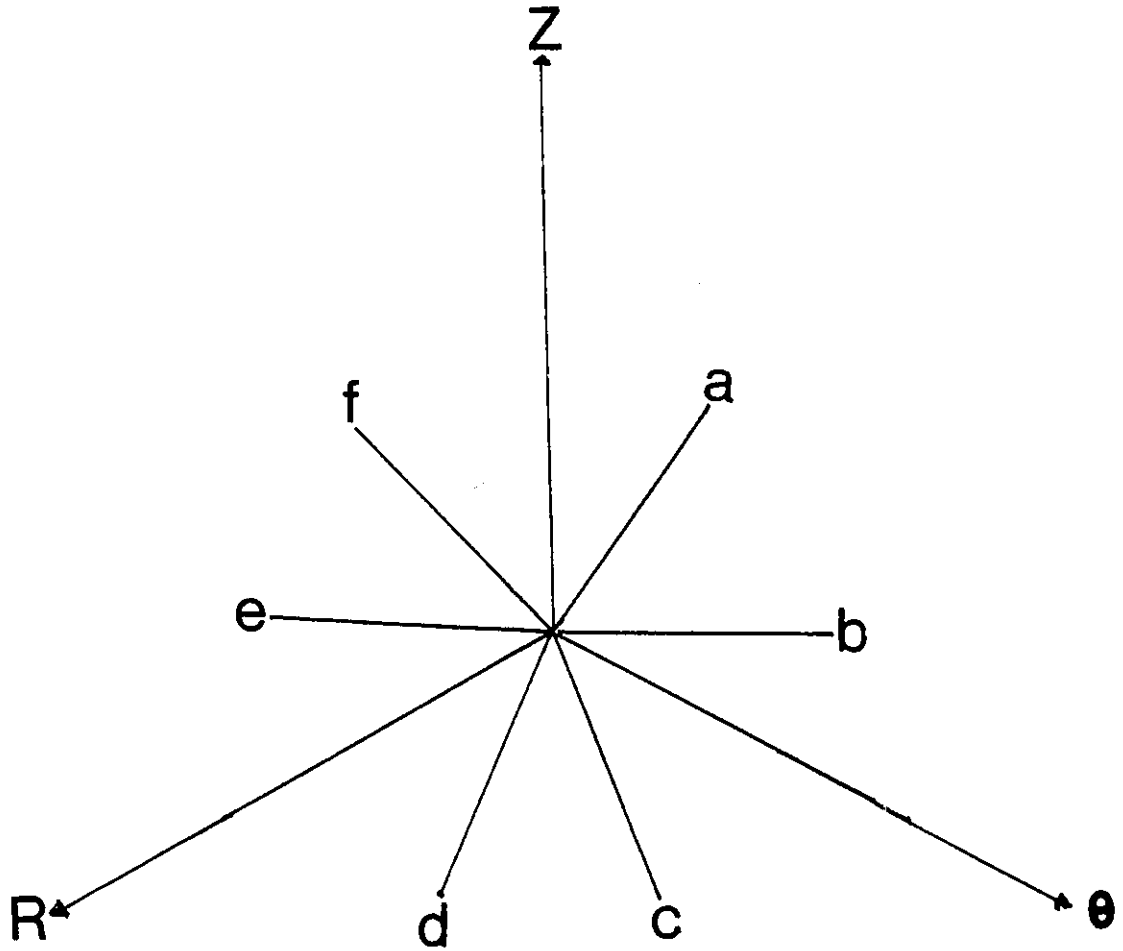


Figure 2.10 Schematic diagram showing the directions corresponding to the different Knoop indenter orientations on a π -plane.

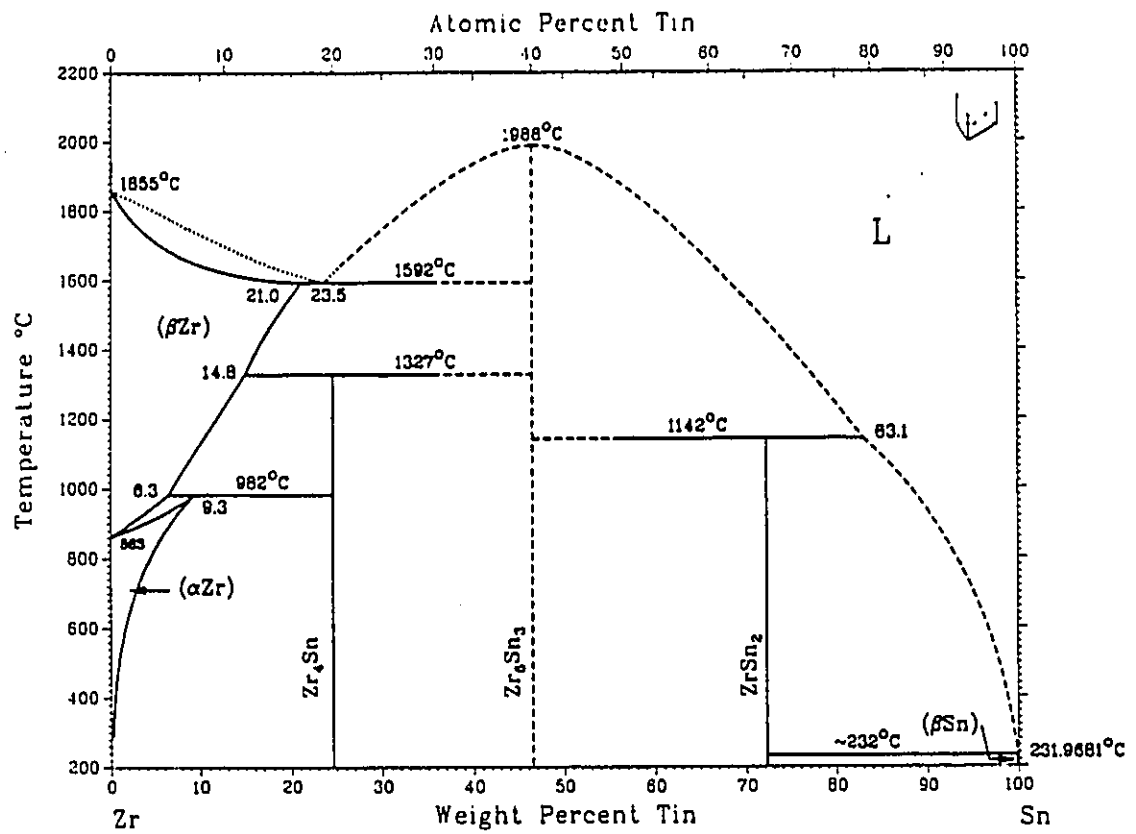


Figure 2.11 The binary Zr-Sn phase diagram⁽²⁴⁾.

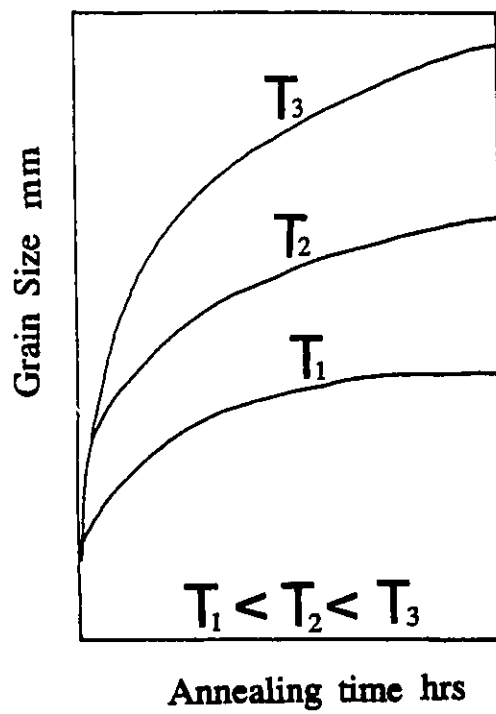


Figure 2.12 A typical curve showing the effect of annealing temperature and duration on grain size⁽²¹⁾.

CHAPTER 3

EXPERIMENTAL DETAILS

3.1 MATERIALS

The material used in this work was as-fabricated Zircalloy-4 fuel tubing. The tubing was provided in the 60% tube-reduced and stress relieved condition. The complete chemical analysis is given in Table 3.1. The tubing size was 15.5 mm outside diameter and 0.4 mm wall thickness.

3.2 HEAT TREATMENT

Small sections of the tubing were cut and sealed, to prevent oxidation, in a vacuum-evacuated quartz tube for heat treatment. The samples were heated to temperatures from 300 to 1000°C (at 100°C intervals $\pm 2^\circ\text{C}$) for 10^3 , 10^4 , and 10^5 seconds. The samples were then cooled in air to room temperature and used for texture and microhardness measurement, TEP, metallography, and ring tensile tests. All measurements were taken at room temperature.

3.3 THERMOELECTRIC POWER (TEP) MEASUREMENTS

The thermoelectric power samples, 40 mm long and 3 mm wide, were cut prior to heating using a slow-speed diamond saw. The thermoelectric power was measured in the axial direction of the tubing.

Figure 3.1 is a schematic diagram showing the experimental set-up for the thermoelectric power measurements. The two aluminum blocks A and B act as a reference metal and are maintained at temperatures T and $T + \Delta T$, respectively. The temperature T was set at 20°C and ΔT at 10°C . The two ends of the flat sample are pressed on these blocks so as to ensure a good thermal and electrical contact. A voltage ΔV (in microvolt) is generated by the thermocouple formed by the sample and the reference metal. ΔS , the relative TEP of the sample at the mean temperature $T + \Delta T/2$ is calculated from equation 2.14.

3.4 RING TENSILE TEST

Rings of 8 mm in width were cut from the heat treated samples having a width to thickness ratio of 20. A width to thickness ratio of 20 was chosen to eliminate the effect of the sample geometry on the test⁽⁹⁾. Special grips were designed for the ring test and these are shown

schematically in Figure 3.2. The yield strength was measured in the tangential direction (θ -direction).

3.5 MICROHARDNESS MEASUREMENTS AND OPTICAL METALLOGRAPHY

The heat treated samples were cut, using a slow diamond saw, into sections of approximate size 10 mm by 10 mm. Each set of three sections (axial, radial, and tangential) were first mounted together using a cold mounting technique. Then they were ground to 600-grit SiC and swab etched using a solution containing 45 ml HNO_3 , 45 ml H_2O and 8 ml Hf. These samples were used for microhardness measurements and suitable ones (showing recrystallization, grain growth, and phase changes) were used for light optical metallography. Metallographic samples were examined at 200 and 500X magnification using polarized light.

The microhardness measurements were made using 50 gf and a Knoop indenter. A Knoop hardness indenter was used in order to obtain information on the anisotropy of the material. The Knoop hardness number (KHN) can be calculated from the equation

$$\text{KHN} = 14229 L / d^2$$

3.1

where L is the load in grams and d is the length of the long diagonal in μm . The Knoop hardness flow surface technique⁽¹¹⁾ was used for the determination of the mechanical anisotropy.

3.5.1 CONSTRUCTION OF THE KNOOP HARDNESS FLOW SURFACE

Hardness indentation for six orientations on the three surfaces (axial, radial, and tangential) were made as shown in Figure 2.9. Each KHN value is plotted on the corresponding line (a, b, c, d, e, and f) on the π -plane as described in section 2.3.4.

Drawing a smooth closed curve through the six KHN points may result in a significant error if it is eye balled. In this study, the error is minimized by fitting the six KHN points to Hill's anisotropic yield criterion (equation 2.10) using a multilinear regression method.

Write equation 2.10 in conventional tubing coordinates (Z, θ , R) by substituting Z for x, θ for y, and R for z. Equation 2.10 now becomes

$$F (\sigma_{\theta} - \sigma_R)^2 + G (\sigma_R - \sigma_Z)^2 + H (\sigma_Z - \sigma_{\theta})^2 = 1 \quad 3.2$$

now, let

$$\begin{aligned} U &= (\sigma_{\theta} - \sigma_R)^2 \\ V &= (\sigma_R - \sigma_Z)^2 \\ W &= (\sigma_Z - \sigma_{\theta})^2 \end{aligned} \quad 3.3$$

Substituting equations 3.3 into equation 3.2 and rearranging we get

$$U = (1/F) - (G/F)V - (H/F)W \quad 3.4$$

Let,

$$\begin{aligned} a &= 1/F \\ b &= - G/F \\ c &= - H/F \end{aligned} \quad 3.5$$

Equation 3.4 now becomes,

$$U = a + bV + cW \quad 3.6$$

U is a linear function of two independent variables, namely, V and W. The "best" values of the coefficients (a, b, and c) are determined by setting up the sum of the squares of the errors (S_r),

$$S_r = \Sigma (U_i - a - bV_i - cW_i)^2 \quad 3.7$$

then, differentiating (equation 3.7) with respect to each of the unknown coefficients. The coefficients yielding the minimum sum of the squares of the errors are obtained by setting the partial derivatives equal to zero as follows :

$$\begin{aligned} (\partial S_r / \partial a) &= -2 \Sigma (U_i - a - bV_i - cW_i) = 0 \\ (\partial S_r / \partial b) &= -2 \Sigma V_i (U_i - a - bV_i - cW_i) = 0 \\ (\partial S_r / \partial c) &= -2 \Sigma W_i (U_i - a - bV_i - cW_i) = 0 \end{aligned} \quad 3.8$$

Expressing equations 3.8 as a set of simultaneous linear equations:

$$\begin{aligned}
na + \Sigma bV_i + \Sigma cW_i &= \Sigma U_i \\
\Sigma aV_i + \Sigma bV_i^2 + \Sigma cW_iV_i &= \Sigma U_iV_i \\
\Sigma aW_i + \Sigma bV_iW_i + \Sigma cW_i^2 &= \Sigma U_iW_i
\end{aligned}
\tag{3.9}$$

in a matrix form,

$$\begin{bmatrix}
n & \Sigma V_i & \Sigma W_i \\
\Sigma V_i & \Sigma V_i^2 & \Sigma W_iV_i \\
\Sigma W_i & \Sigma V_iW_i & \Sigma W_i^2
\end{bmatrix}
\begin{bmatrix}
a \\
b \\
c
\end{bmatrix}
=
\begin{bmatrix}
\Sigma U_i \\
\Sigma U_iV_i \\
\Sigma U_iW_i
\end{bmatrix}
\tag{3.10}$$

One first solves equation 3.10 to obtain a, b, and c, and then calculate the anisotropy coefficients F, G, and H using equations 3.5. Knowing these anisotropy coefficients, the yield strength in the three major directions (Z, θ , and R) of the tubing can be calculated from equations 2.12,

$$\begin{aligned}
Y_Z^2 &= 1 / (G + H) \\
Y_\theta^2 &= 1 / (H + F) \\
Y_R^2 &= 1 / (F + G)
\end{aligned}
\tag{3.11}$$

where Y_Z , Y_θ , and Y_R are the yield strengths in the Z, θ , and R directions respectively. These are the intercepts of the Z, θ , and R axes on the π -plane.

The values of U_i , V_i , and W_i are determined by equation 3.3, hence,

$$\begin{aligned}
 U_i &= (\sigma_{\theta i} - \sigma_{Ri})^2 \\
 V_i &= (\sigma_{Ri} - \sigma_{Zi})^2 \\
 W_i &= (\sigma_{Zi} - \sigma_{\theta i})^2
 \end{aligned}
 \tag{3.12}$$

Where σ_{Zi} , $\sigma_{\theta i}$, and σ_{Ri} are determined from the π -plane by resolving each of the six KHN points (in the a, b, c, d, e, and f directions) into three components in the Z, θ , and R directions, respectively. The sum of the squares of the errors can be evaluated by substituting the values of a, b, and c into equation 3.7. It should be mentioned that the sum of the squares of the errors (S_e) depends upon which variable (U, V, or W) we choose as the dependent variable. In the above analysis U was chosen to be the dependent variable (equation 3.4). Similar analyses were done using V and W as the dependent variables, and three different sums of squares of errors were obtained. The criterion adopted was that the

smallest of the errors gives the best fit, i.e. the anisotropy coefficients F, G, and H that were chosen corresponded to the smallest of the three sums of the error squares calculated.

Figure 3.3 lists the "Basic" computer program that performs the multilinear regression analysis, and calculates the values of F, G, H, Y_z , Y_θ , Y_R and S_r . The flow surface was then plotted using Statistical Analysis System (SAS) computer software package.

3.6 TEXTURE MEASUREMENTS

The heat treated samples were cut into small sections displaying the radial, tangential and axial surfaces. For the tangential and axial surfaces, small sections were placed side-by-side to make the sample area larger than the area covered by the x-ray beam.

The x-ray diffraction patterns were recorded using an x-ray diffractometer and a graphite monochromated CuK_α radiation. The patterns were recorded over the range 2θ from 20 to 140° using a scan rate of 2° per minute. These diffraction patterns were recorded for the radial, tangential, and axial directions by exposing the respective surfaces to the

x-ray beam scan. The randomly oriented sample was a zirconium powder (~ 325 mesh). The zirconium particles, having all possible orientations with respect to the x-ray beam, have diffraction intensities that define the crystallographic isotropy.

3.6.1 CALCULATION OF f-PARAMETER

The texture of the tubing was determined using Kearn's⁽³⁾ technique. The output of this technique is the f-parameter, a number that represents the texture quantitatively.

First, the intensities of all (hkil) reflections for the test sample and the random sample were determined. A texture coefficient (T.C.) for each (hkil) reflection is calculated using equation 2.1. Each of the reflection planes is at some tilt angle ϕ from the basal pole [0001] as shown by the stereographic projection in Figure 3.4a. Figure 3.4b shows the hexagonal prism and the angles between major (hkil) planes and the basal plane. However, as indicated by Figure 3.4a, the diffraction planes are located along lines at only three positions of the rotation angle α :

0° ($10\bar{1}l$) , 19.1° ($21\bar{3}l$) , and 30° ($11\bar{2}l$).

First, average T.C. values were calculated at tilt angles ϕ at 3° increments for all three lines, $(10\bar{1}\ell)$, $(21\bar{3}\ell)$, and $(11\bar{2}\ell)$, separately. We assume that the intensity between diffraction points varies linearly with the tilt angle ϕ . Thus,

$$T.C._j(\phi) = T.C._{dj} + [(\phi - \phi_d) / (\phi_{d+1} - \phi_d)] * (T.C._{(d+1)j} - T.C._{dj}) \quad 3.13$$

where $T.C._j(\phi)$ is the texture coefficient at some tilt angle ϕ for line j . $T.C._{dj}$ and $T.C._{(d+1)j}$ are the texture coefficients of two consecutive diffraction planes, d and $d+1$, on the same line (j). ϕ_d and ϕ_{d+1} are the tilt angles of the d and $d+1$ diffraction planes.

It is also assumed that the intensity varies linearly with the rotation angle α . Thus, the $T.C.(\phi)$ value is averaged over the range of α which is 30° on an inverse pole figure. The average texture coefficient at an angle ϕ where all three lines are defined is calculated by

$$T.C.(\phi)_{\text{average}} = (1/30) \{ 19.1 [(T.C._1(\phi) + T.C._2(\phi))/2] + 10.9 [(T.C._2(\phi) + T.C._3(\phi))/2] \} \quad 3.14$$

Where $T.C._1(\phi)$, $T.C._2(\phi)$, and $T.C._3(\phi)$ are the texture coefficients of lines 1, 2, and 3, respectively, at the same tilt angle ϕ . If only two lines were defined, for example, lines 1 and 2, then the $T.C.(\phi)_{\text{average}}$ is calculated by simple averaging,

$$T.C.(\phi)_{\text{average}} = [T.C._1(\phi) + T.C._2(\phi)]/2 \quad 3.15$$

Finally, having calculated the average pole density (intensity distribution), $T.C.(\phi)_{\text{average}}$, the f-parameter can now be calculated from equation 2.3,

$$f = \sum V_o^f \text{Cos}^2 \phi$$

where V_o^f is calculated by an equation similar to equation 2.4,

$$V_o^f = [T.C.(\phi)_{\text{average}} \text{Sin} \phi] / [\sum T.C.(\phi)_{\text{average}} \text{Sin} \phi] \quad 3.16$$

Figure 3.5 lists the " Basic " computer program for calculation of the f-parameter.

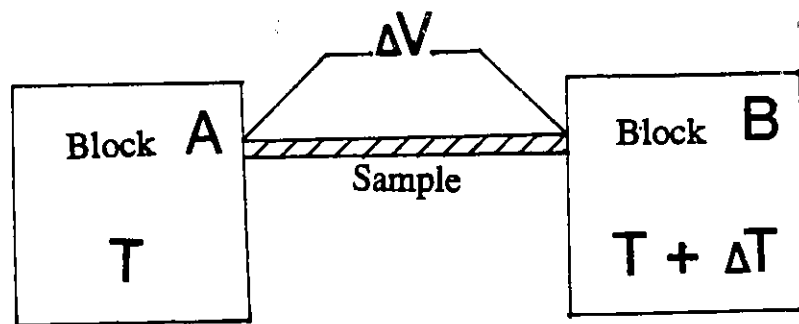


Figure 3.1 Schematic diagram showing experimental set-up for thermoelectric power (TEP) measurements.

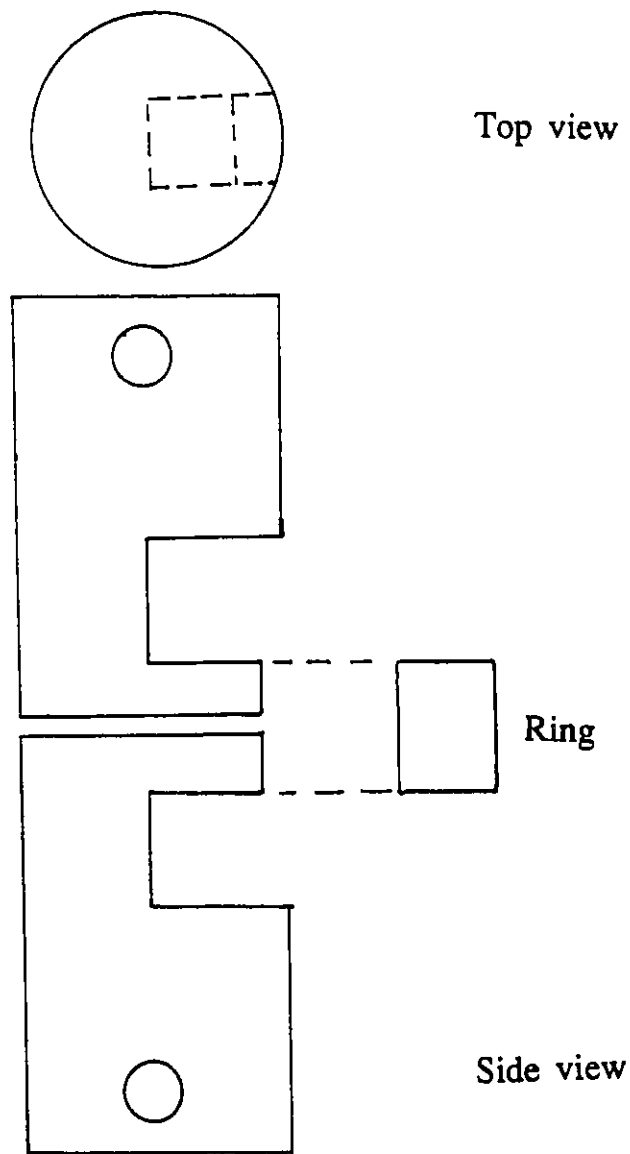


Figure 3.2 Schematic diagram showing tensile grips for ring sample.

```

100 DIM A(6,3)
110 FOR I=1 TO 6
120 FOR J=1 TO 3
130 READ A(I,J)
131 NEXT J
132 LPRINT A(I,1) ; A(I,2) ;A(I,3)
133 NEXT I
140 DATA 6.3,3.8,0
150 DATA 4.2,7.1,0
160 DATA 0,4.8,2.8
170 DATA 0,2.9,4.8
180 DATA 4,0,6.6
190 DATA 6.2,0,3.8
200 DIM U(6),V(6),W(6)
210 SUMU=0:SUMV=0:SUMW=0:SUMVV=0:SUMWW=0:SUMWV=0:SUMUV=0:SUMUW=0
220 FOR L=1 TO 6
230 U(L)=(A(L,2)-A(L,3))^2
240 V(L)=(A(L,3)-A(L,1))^2
250 W(L)=(A(L,1)-A(L,2))^2
260 SUMU=SUMU+U(L)
270 SUMV=SUMV+V(L)
280 SUMW=SUMW+W(L)
290 SUMVV=SUMVV+(V(L)*V(L))
300 SUMUU=SUMUU+(U(L)*U(L))
310 SUMUV=SUMUV+(U(L)*V(L))
320 SUMWV=SUMWV+(W(L)*V(L))
330 SUMUW=SUMUW+(U(L)*W(L))
340 NEXT L
350 DIM B(3,4),C(3,4)
360 N=6
370 B(1,1)=N:B(1,2)=SUMV:B(1,3)=SUMU:B(1,4)=SUMW
380 B(2,1)=SUMV:B(2,2)=SUMVV:B(2,3)=SUMUV:B(2,4)=SUMWV
390 B(3,1)=SUMU:B(3,2)=SUMUV:B(3,3)=SUMUU:B(3,4)=SUMUW
400 FOR K=1 TO 3
410 PIVOT=B(K,K):IL=K
420 FOR L=K+1 TO 3
430 IF ABS(B(L,K))<ABS(PIVOT) THEN GOTO 460
440 PIVOT=B(L,K)
450 IL=L
460 NEXT L
470 FOR LL=1 TO 4

```

Figure 3.3 "Basic" computer program for calculation of the anisotropy coefficients.

```

480  TEMP=B(K,LL)
490  B(K,LL)=B(IL,LL)
500  B(IL,LL)=TEMP
510  NEXT LL
520  FOR J=1 TO 4
530  C(K,J)=B(K,J)/PIVOT
540  NEXT J
550  FOR I=1 TO 3
560  IF I=K GOTO 600
570  FOR J=1 TO 4
580  C(I,J)=B(I,J)-B(I,K)*C(K,J)
590  NEXT J
600  NEXT I
610  FOR I=1 TO 3
620  FOR J=1 TO 4
630  B(I,J)=C(I,J)
640  NEXT J
650  NEXT I
660  NEXT K
680  LPRINT "11W"
700  H=1/B(1,4)
710  G=(-H)*B(2,4)
720  F=(-H)*B(3,4)
730  LPRINT "F=";F ; "G=";G ; "H=";H
740  XX=(1/(G+H))^.5
750  YY=(1/(H+F))^.5
760  ZZ=(1/(F+G))^.5
770  LPRINT "XX=";XX ; "YY=";YY ; "ZZ=";ZZ
780  SUMSR=0:SUMST=0
790  FOR M=1 TO 6
800  SR=(W(M)-B(1,4)-B(2,4)*V(M)-B(3,4)*U(M))^2
810  SUMSR=SUMSR+SR
820  ST=(W(M)-SUMW/6)^2
830  SUMST=SUMST+ST
840  NEXT M
850  R=((SUMST-SUMSR)/SUMST)^.5
870  LPRINT "SUMSR=";SUMSR ; "R=";R
880  END

```

Figure 3.3 cont'd

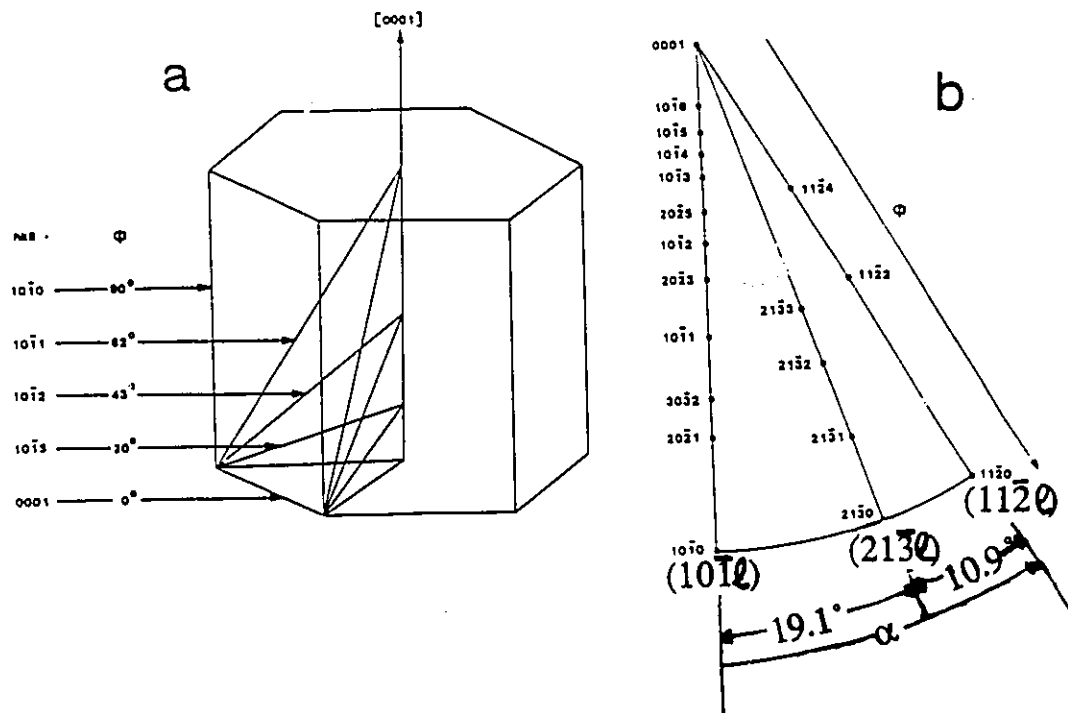


Figure 3.4 (a) Schematic diagram of the hexagonal prism and the tilt angle (ϕ) between the major (hkil) planes and the basal plane; (b) standard stereographic projection for α -Zr showing the positions of the major (hkil) poles and the rotation angle α .

```

1020 DIM Z(20)
1030 FOR N=1 TO 19
1040 READ Z(N)
1050 NEXT N
1060 DATA 100,3.6,5,26.5,5.2,19.1,5,81.6,1.8,4,13.2,3.2,1,2.9,.6,10,6.5,15.6,5.
5
5010 DIM RZ(19) : DIM NM(19) : DIM TC(19)
5020 FOR J=1 TO 19 : READ RZ(J)
5030 NEXT J
5040 DATA 35.5,12.3,5.2,29.6,9.3,16.4,8.2,100,11.2,23.2,15.6,15.7,6.7,16.7,3.7,
4.6,15.3,22.9,16.3
5050 SM=0
5060 FOR J=1 TO 19
5070 NM(J)=Z(J)/RZ(J)
5090 SM=SM+NM(J)
5100 NEXT J
5110 FOR J=1 TO 19 : TC(J)=19*(NM(J)/SM)
5130 NEXT J
5160 DIM AG(3,11) : DIM TX(3,11) : DIM PH(30) : DIM RX(3,30) : DIM PG(30)
5170 FOR J=1 TO 11 : READ AG(1,J) : LPRINT AG(1,J) : TX(1,J)=TC(J):NEXT J
5180 FOR J=1 TO 4 : READ AG(2,J) : LPRINT AG(2,J) : TX(2,J)=TC(J+11):NEXT J
5190 FOR J=1 TO 4 : READ AG(3,J) : LPRINT AG(3,J) : TX(3,J)=TC(J+15):NEXT J
5200 DATA 0,20.2,24.7,31.5,36.3,42.5,50.7,61.4,70.1,74.8,90,58.3,67.6,78.4,90.0
,38.5,57.8,90
5250 FOR K= 1 TO 3
5260 XX=1.5:IA=2:IB=1
5270 FOR J=1 TO 30
5275 PH(J)=XX*3.14159/180 :PG(J)=XX
5280 IF XX<AG(K,1) THEN RX(K,J)=-1
5290 IF XX<AG(K,1) THEN 5330
5300 IF XX>AG(K,IA) THEN IB=IA
5310 IF XX>AG(K,IA) THEN IA=IA+1
5320 RX(K,J)=TX(K,IB)+((XX-AG(K,IB))/(AG(K,IA)-AG(K,IB)))*(TX(K,IA)-TX(K,IB))
5323 IF K<=3 THEN 5330
5324 IF J>=14 THEN 5330

```

Figure 3.5 "Basic" computer program for calculation of the f-parameter.

```

5325 IF RX(3,J) < RX(1,J) THEN RX(3,J)=-1
5330 XX=XX+3
5340 NEXT J
5350 NEXT K
5370 DIM RA(30): DIM AN(30) : DIM VL(30)
5380 SM =0: FT=0: FI=0
5390 FOR J=1 TO 30
5400 IF RX(2,J)>=0 THEN 5430
5410 IF RX(3,J)>=0 THEN RA(J) =(RX(1,J)+RX(3,J))/2: GOTO 5450
5420 RA(J)=RX(1,J) : GOTO 5450
5430 IF RX(3,J)=-1 THEN RA(J)=(RX(1,J)+RX(2,J))/2 : GOTO 5450
5440 RA(J)=1/30*((19.1*(RX(1,J)+RX(2,J))/2)+(10.9*(RX(2,J)+RX(3,J))/2))
5450 AN(J)=RA(J)*SIN(PH(J)): SM=SM+AN(J)
5460 NEXT J
5461 LPRINT SM
5470 FOR J=1 TO 30
5480 VL(J)=AN(J)/SM
5490 FI=VL(J)*((COS (PH(J)))^ 2)
5500 FT=FT+FI: NEXT J
5530 FOR J=1 TO 30
5540 LPRINT PG(J);" ";RX(1,J);" ";RX(2,J);" ";RX(3,J);" ";RA(J)
5550 NEXT J
5570 FOR J=1 TO 30
5580 LPRINT PG(J);" ";RA(J);" ";VL(J)
5590 NEXT J
5610 FOR J=1 TO 19
5620 LPRINT TC(J);" ";Z(J);" ";RZ(J)
5630 NEXT J
5640 LPRINT "F_PAR=": FT
5660 END

```

Figure 3.5 cont'd

Table 3.1 Chemical analysis for Zircaloy-4 fuel tubing.

| | | | |
|----|---------|----|---------|
| Al | <20 | Nb | <50 |
| B | .30 | Ni | <35 |
| Cd | .25 | O | 1290 |
| Co | <10 | Pb | <25 |
| Cr | .095wt% | Si | 29 |
| Cu | <25 | Sn | 1.54wt% |
| Fe | .208wt% | Ta | <100 |
| Hf | 68 | Ti | <25 |
| Mg | <10 | V | <25 |
| Mn | <25 | W | <50 |
| Mo | <10 | N | 23 |

All results, other than wt%, are ppm.

CHAPTER 4

EXPERIMENTAL RESULTS

4.1 MICROHARDNESS MEASUREMENTS

4.1.1 FLOW SURFACE DIAGRAMS

The Knoop hardness values for the six "hardness impression" directions (a, b, c, d, e and f-see Fig.2.9) are given in Table 4.1 for temperatures from 300°C to 1000°C at 100°C intervals and for three different annealing times of 10^3 , 10^4 and 10^5 seconds. The "best fit" Knoop hardness flow surface diagrams constructed from these results are shown in Figures 4.1 to 4.25. Flow surface diagrams of the Zircaloy-4 cladding have, in general, an elliptical shape which is indicative of high degree of anisotropy.

Examination of Table 4.1 and Figures 4.1 to 4.25 show that:

- 1- For annealing time of 10^3 seconds the elliptical flow surface undergoes an "overall" reduction in size (an overall softening) with increasing annealing temperature. However, a clockwise rotation of the major axis of

the ellipse is evident at an annealing temperature of 500°C. This results in the ellipse becoming narrower in the Z-direction (softer in the axial direction) and wider in the θ -direction (stronger in the tangential direction). At an annealing temperature of a 1000°C the flow surface becomes somewhat circular in shape, that is, the hardness in all directions is comparable.

2- For an annealing time of 10^4 seconds the general trend is similar to that found for the 10^3 seconds annealing time where the general softening is observed. However, at an annealing temperature of 600°C the flow surface undergoes a considerable clockwise rotation of the major axis of the ellipse, making the tangential direction (θ -direction) a stronger direction than the radial and axial directions. At the annealing temperature of 900°C, again, we observe a further change in anisotropy, and the radial direction (R-direction) becomes the strongest direction. At an annealing temperature of 1000°C isotropy is evident from the shape of the flow surface (almost circular).

3- For annealing time of 10^5 seconds a general softening occurs as the annealing temperature is increased. At a temperature of 600°C a change in

anisotropy takes place, whereby, the major axis of the elliptical flow surface rotates clockwise making the tangential direction the strongest direction, i.e. as for the 10^4 seconds annealing time. At a temperature of 1000°C the flow surface becomes circular which characterizes the isotropic case. At this temperature, i.e. 1000°C , mechanical isotropy is more evident for an annealing time of 10^5 seconds than it was for the shorter annealing times of 10^3 and 10^4 seconds.

4.1.2 ANISOTROPY RATIO

For the purposes of this study, the degree of mechanical anisotropy is defined as the "min/max" ratio of the major and the minor axes of the ellipse of the flow surface. The degree of anisotropy (as thus defined) of Zircaloy-4 cladding after various heat treatments is given in Tables 4.2 to 4.4 and Figures 4.26 to 4.28.

Examination of the annealing temperature versus the mechanical anisotropy ratio for different annealing times shows that: for annealing times 10^3 and 10^4 seconds the mechanical anisotropy ratio undergoes no significant change up to a temperature of 500°C . At temperatures from 500 to 900°C the mechanical anisotropy ratio decreases, that is, the Zircaloy-

4 fuel cladding becomes more anisotropic. When heated at temperature of 1000°C the mechanical anisotropy ratio increases sharply approaching a value of unity which is indicative of mechanical isotropy.

For heating time of 10^5 seconds and annealing temperatures up to 500°C there is no significant change in the mechanical anisotropy ratio. At an annealing temperature of 500°C the mechanical anisotropy ratio starts to climb, that is, Zircaloy-4 cladding becomes more isotropic. At a temperature of 800°C the mechanical anisotropy ratio decreases, then increases again for temperatures up to a 1000°C where it reaches a min/max ratio of about unity.

4.1.3 KHN VERSUS ANNEALING TEMPERATURE

Values of Knoop microhardness for all three directions (radial, axial, and tangential) in the tubing are given in Tables 4.2 to 4.4 and Figures 4.29 to 4.31 as a plot of KHN versus annealing temperature. Examination of these results shows that, overall, the radial direction is the strongest direction, followed by the tangential direction and finally the axial direction, which is the softest direction.

1- For an annealing time of 10^3 seconds the KHN's in the axial and

tangential directions (Y_z and Y_θ , respectively) show the same general trend. For a temperature up to 500°C there are no significant changes in the values of KHN. The microhardness then decreases significantly for temperatures up to 800°C, remains reasonably constant from 800 to 900°C before increasing again at 1000°C. The axial direction, however, exhibits an increase in microhardness at 400°C. The microhardness then decreases and remain fairly constant from 500 to 900°C before it drops sharply at 1000°C.

2- For an annealing time of 10^4 seconds, the KHN values for the three directions show the same general softening for temperatures up to 400°C. The KHN values for the radial direction remain fairly constant from 500 to 800°C, then increase at 900°C and finally drop sharply at 1000°C. The microhardness in the axial direction remains almost constant from 400 to 700°C, then drops and remains reasonably constant from 700 to 900°C, before sharply increasing at 1000°C. The microhardness in the tangential direction, however, differs somewhat from the general trend. A sharp increase is observed starting from a temperature of 400°C up to a maximum microhardness at 600°C, where the tangential direction becomes the strongest direction. The microhardness in the tangential direction then

drops again for temperatures up to 900°C. As was the case for the axial direction, an increase in KHN values is observed at 1000°C.

3- For annealing time of 10^5 seconds, a steady decrease in microhardness was observed up to an annealing temperature of 400°C. This was followed by a sharp decrease at 500°C. The KHN remains reasonably constant up to 800°C when it starts to increase again up to an annealing temperature of 1000°C for the axial and the tangential directions. The microhardness in the radial direction remains almost constant from 600 to 1000°C.

4.2 TEXTURE

The f-parameters for various annealing conditions are given in Tables 4.5 to 4.7 and Figures 4.32 to 4.35. Examination of these results shows that, for all annealing conditions up to 900°C, the radial direction has the largest f-parameter and the axial direction has the smallest f-parameter. That is, the largest number of [0001] poles tend to be aligned parallel to the radial direction, and the number of [0001] poles, tending to be aligned parallel to the axial direction, is the smallest. An exception to this occurs at a temperature of about 950°C for 10^3 and 10^4 seconds annealing time, in which, the radial and tangential curves cross each other and the f-

parameter in the tangential direction becomes greater than that in the radial direction.

1- For annealing time of 10^3 seconds and annealing temperatures up to 300°C we observe no change in texture in all three directions. In the temperature range 300 to 500°C an increase in the f-parameter is evident in the tangential direction, which is, accompanied by a decrease in the f-parameter in the axial direction and no significant change in the f-parameter in the radial direction. For the temperature range 600 to 900°C the f-parameter increases in the radial and axial directions accompanied by a corresponding decrease in the f-parameter in the tangential direction. At a temperature from 800 to 1000°C the f-parameter in the radial direction drops drastically, while, it climbs sharply in the axial direction without any significant change in the tangential direction. At 1000°C the value of the f-parameters in all three directions approach each other, that is, the tubing becomes somewhat crystallographically isotropic.

2- For annealing time of 10^4 seconds the f-parameter curves in all three directions have the same general trend as the 10^3 seconds annealing time curves. However, for the 10^4 seconds annealing time a sharp increase in the f-parameter up to 500°C is observed in the tangential direction

accompanied by a decrease in the axial direction and a slower increase in the radial direction. At 800°C the f-parameter drop in the radial direction is not as steep as for the 10^3 seconds annealing time. At an annealing temperature of 1000°C the texture of the tubing approaches the isotropic state.

3- For an annealing time of 10^5 seconds the same general trends are evident except that the f-parameters in the radial and tangential directions, for annealing temperatures ranging from 500 to 900°C, are not as close (in magnitude) as was the case for the shorter annealing times. However, at 1000°C the tangential and radial directions have the same f-parameter value, and thus the tubing is perfectly isotropic in the radial-tangential (R- θ) plane. The f-parameter in the axial direction also approaches the isotropic condition, i.e. $f=0.333$, which makes the tubing almost perfectly isotropic.

4.3 THERMOELECTRIC POWER (TEP)

The thermoelectric power (TEP) values for various heat treatment conditions are summarized in Tables 4.8 to 4.10 and Figure 4.35. Examination of these results shows that in the temperature range 300 to

400°C (for the 10^3 , 10^4 and 10^5 seconds annealing times) the TEP value tends to decrease. In the annealing temperature range 400 to 500°C no significant change in TEP value has occurred, beyond 500°C and up to 600°C the TEP value increases sharply. Then it drops again at 700°C for both 10^3 and 10^5 seconds annealing times. For the annealing time of 10^4 seconds, however, the TEP value climbs up to 700°C then drops down at 800°C. In the temperature range 800 to 1000°C a steady increase in the TEP value is evident for all the three annealing times.

4.4 OPTICAL METALLOGRAPHY

Micrographs of the fuel sheathing in the as-received condition and after heating for 10^3 , 10^4 and 10^5 seconds at 500, 600, 800, 900, and 1000°C (followed by air cooling to ambient temperature) are given in Figures 4.36 to 4.51 and grain sizes for selected samples, to show the growth of the recrystallized α -grains, are given in Table 4.11.

Examination of these results shows that:

- 1- The as-received microstructure, Figure 4.36 consists of small elongated α -grains which are produced by the drawing process for the tubing.

2- At a temperature of 500°C. for all annealing times, there is partial recrystallization and "new" small, equiaxed α -grains are observed. The grain size of these newly nucleated grains increases as the annealing time is increased.

3- At an annealing temperature of 600°C recrystallization is essentially complete and the grain size is evidently larger for longer annealing times as shown by comparing Figures 4.40 to 4.42 and Table 4.11.

4- At 800°C growth of the α -grains is evident. The grain size again increases with the duration of annealing (see Figures 4.43 to 4.45 and Table 4.11).

5- Heating the alloy at 900°C brings it above the α -Zr/(α -Zr+ β -Zr) transus (about 870°C) and into the β -Zr phase region (about 890°C). On cooling (in air) to room temperature all the β -Zr transforms to α' (transformed β). The α' has a basketweave or parallel-plate Widmanstatten structure. The size and amount of α' increases with increasing annealing time. The amount of α' is estimated to be 10, 30, and 50% of the microstructure for 10^3 , 10^4 and 10^5 seconds annealing time, respectively. The remainder of the

microstructure is retained α . This is illustrated in Figures 4.46 to 4.48.

6- Heating at 1000°C brings the alloy into the single phase β -Zr region. Cooling to room temperature produces α' structure. Figures 4.49 to 4.51 show very large α' -grains having a basketweave structure and increasing in size as annealing time is increased.

4.5 OXYGEN EFFECTS

Oxygen, which can be absorbed during annealing process, can have two effects on the Zr-Sn alloys. The first effect is to raise the α -Zr/(α -Zr+ β -Zr) transus temperature. The second effect is a strengthening effect⁽²⁵⁾. The oxygen content of Zircaloy-4 cladding was determined for the as received sample as well as samples annealed at 500°C or 1000°C for 10³, 10⁴ and 10⁵ seconds. Table 4.12 gives the oxygen contents of the samples.

Examination of Table 4.12 shows that, at an annealing temperature of 500°C and for all annealing times, the oxygen content of Zircaloy-4 tubing is comparable to that of the as-received sample tubing. At an annealing temperature of 1000°C absorption of oxygen has evidently occurred. For

an annealing time of 10^3 seconds (at 1000°C) the oxygen content is comparable to that for the as-received sample. However, as the annealing time increases to 10^4 and 10^5 seconds a significant increase in the oxygen content is observed, which indicates that oxygen absorption has taken place.

4.6 RING TENSILE TEST

The ring tensile test results for various heat treatment conditions are summarized in Table 4.13. Examination of Table 4.13 shows that, the yield strength in the tangential direction (θ -direction) "generally" tends to increase with an increase in annealing time, for both annealing temperatures of 500 and 1000°C .

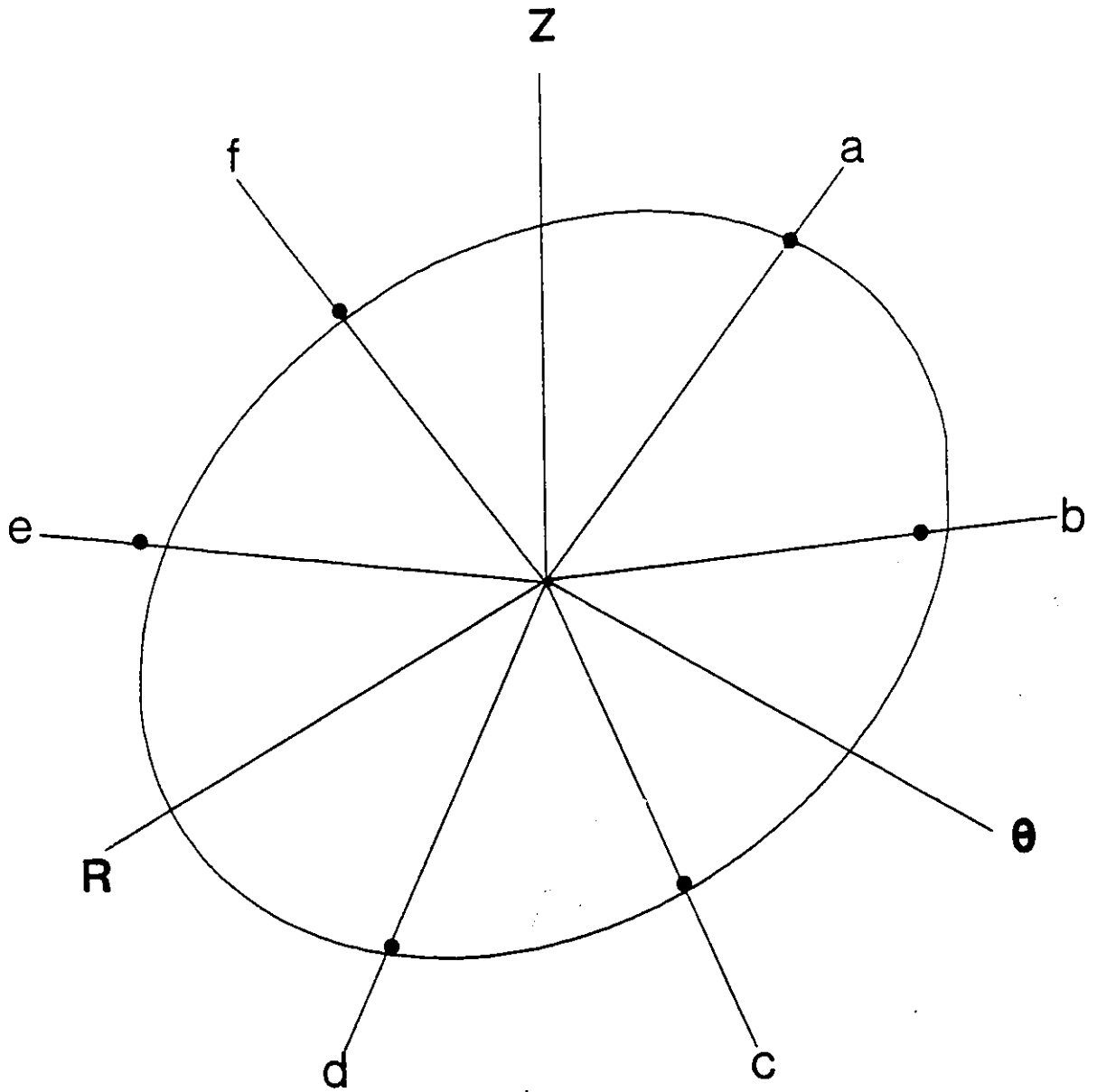


Figure 4.1 Flow surface diagram for Zircaloy-4 tubing in the as-received condition.

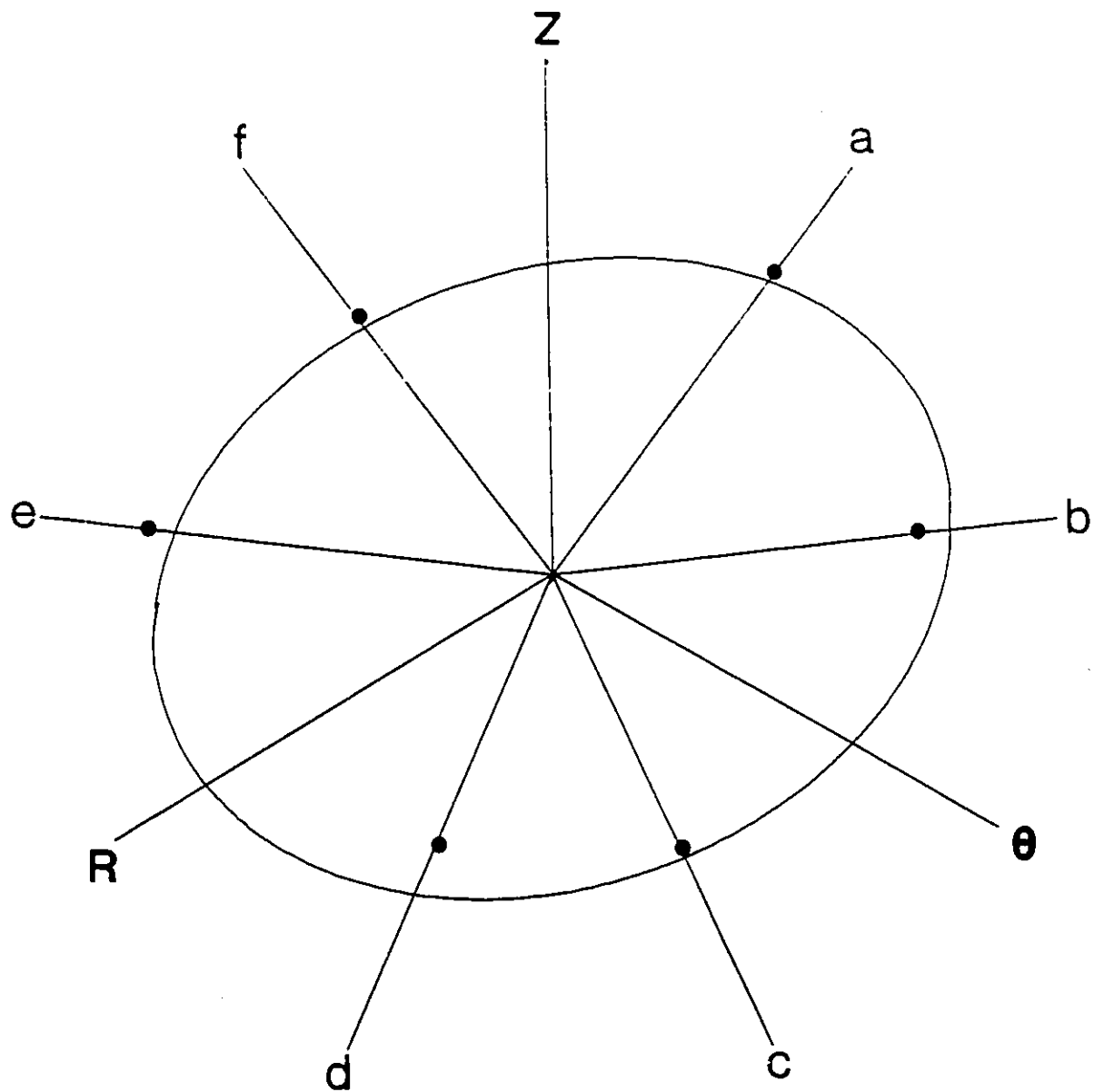


Figure 4.2 Flow surface diagram for Zircaloy-4 tubing annealed at 300°C for 10³ seconds.

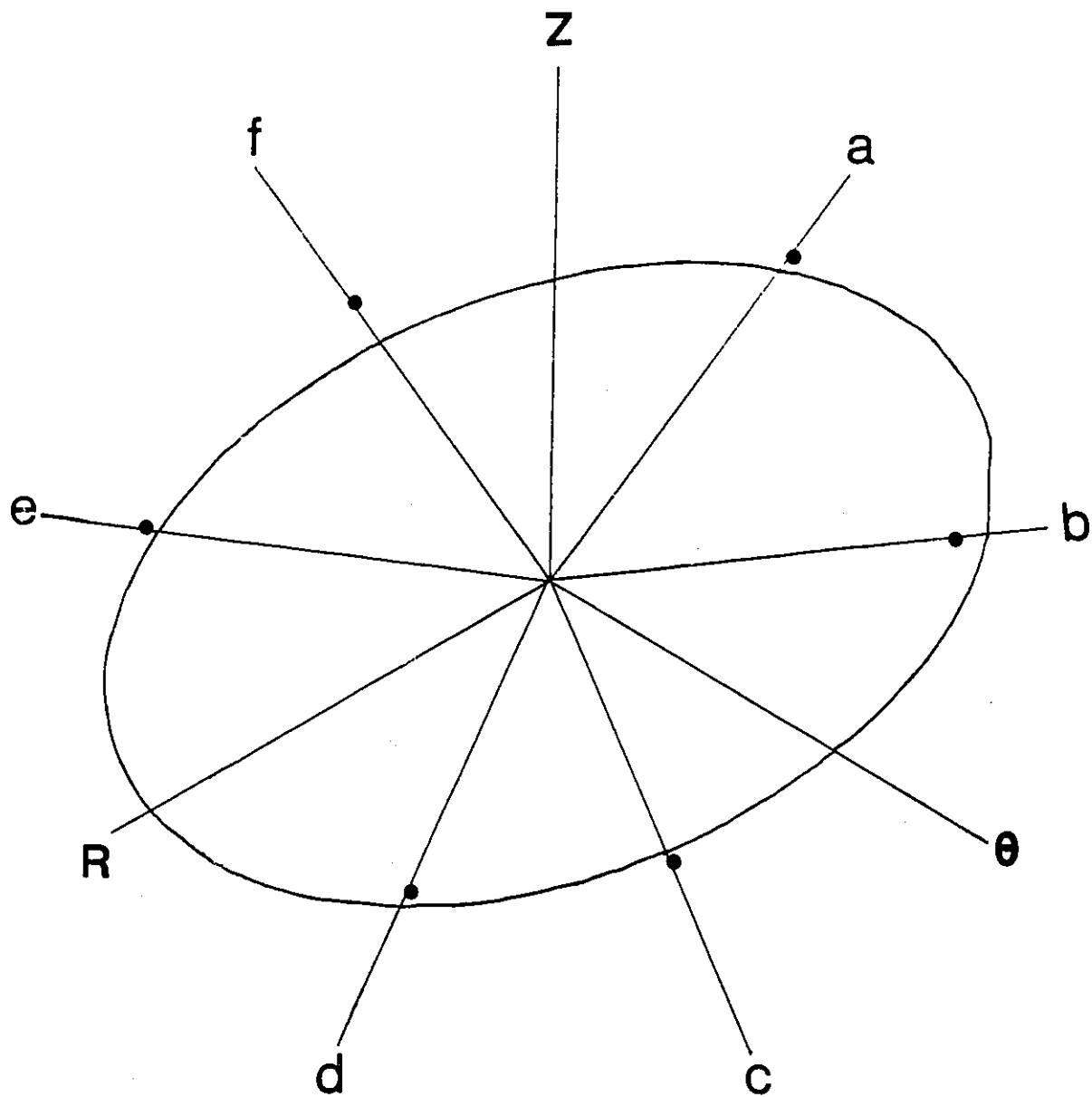


Figure 4.3 Flow surface diagram for Zircaloy-4 tubing annealed at 400°C for 10³ seconds.

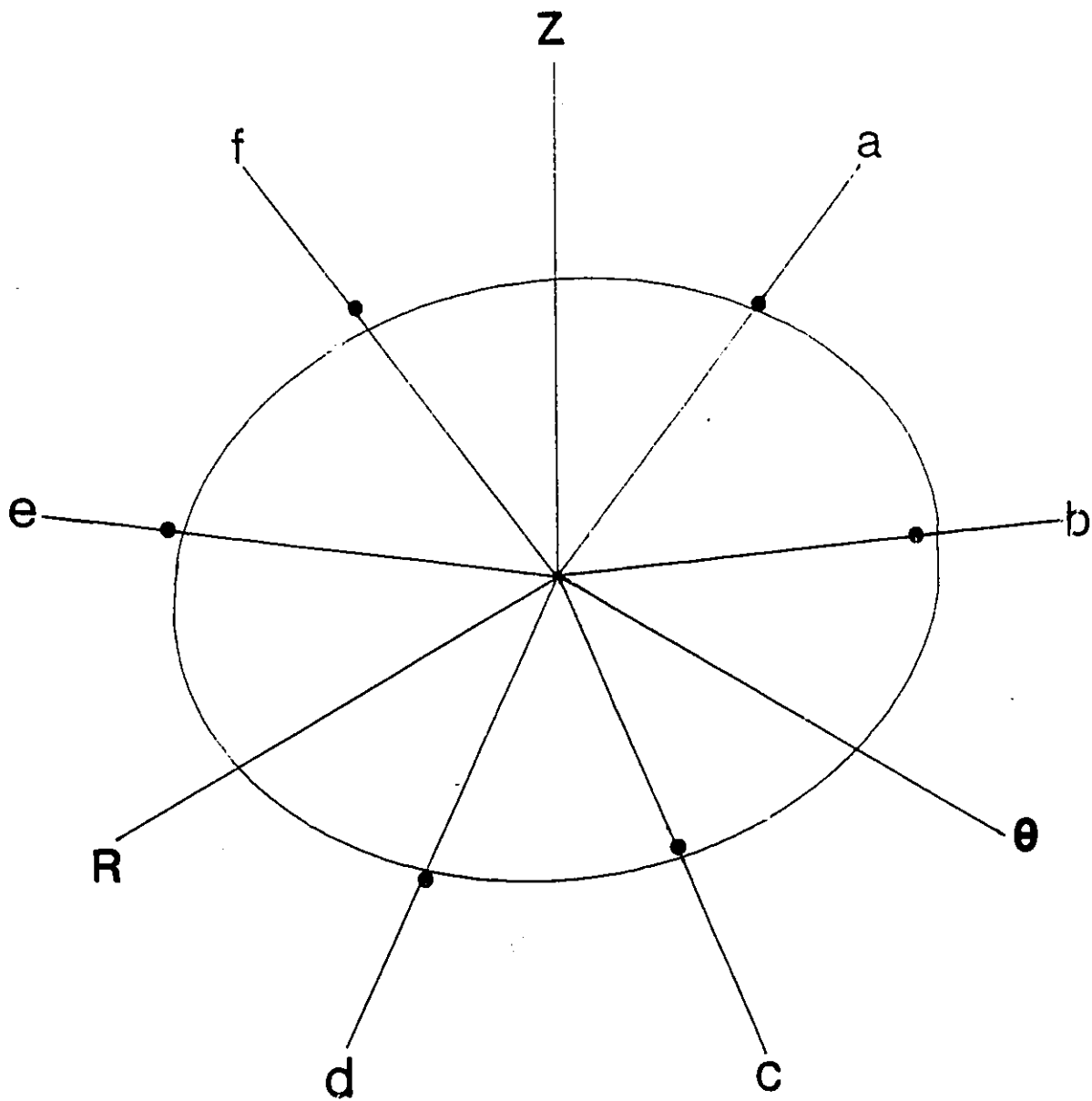


Figure 4.4 Flow surface diagram for Zircaloy-4 tubing annealed at 500°C for 10^3 seconds.

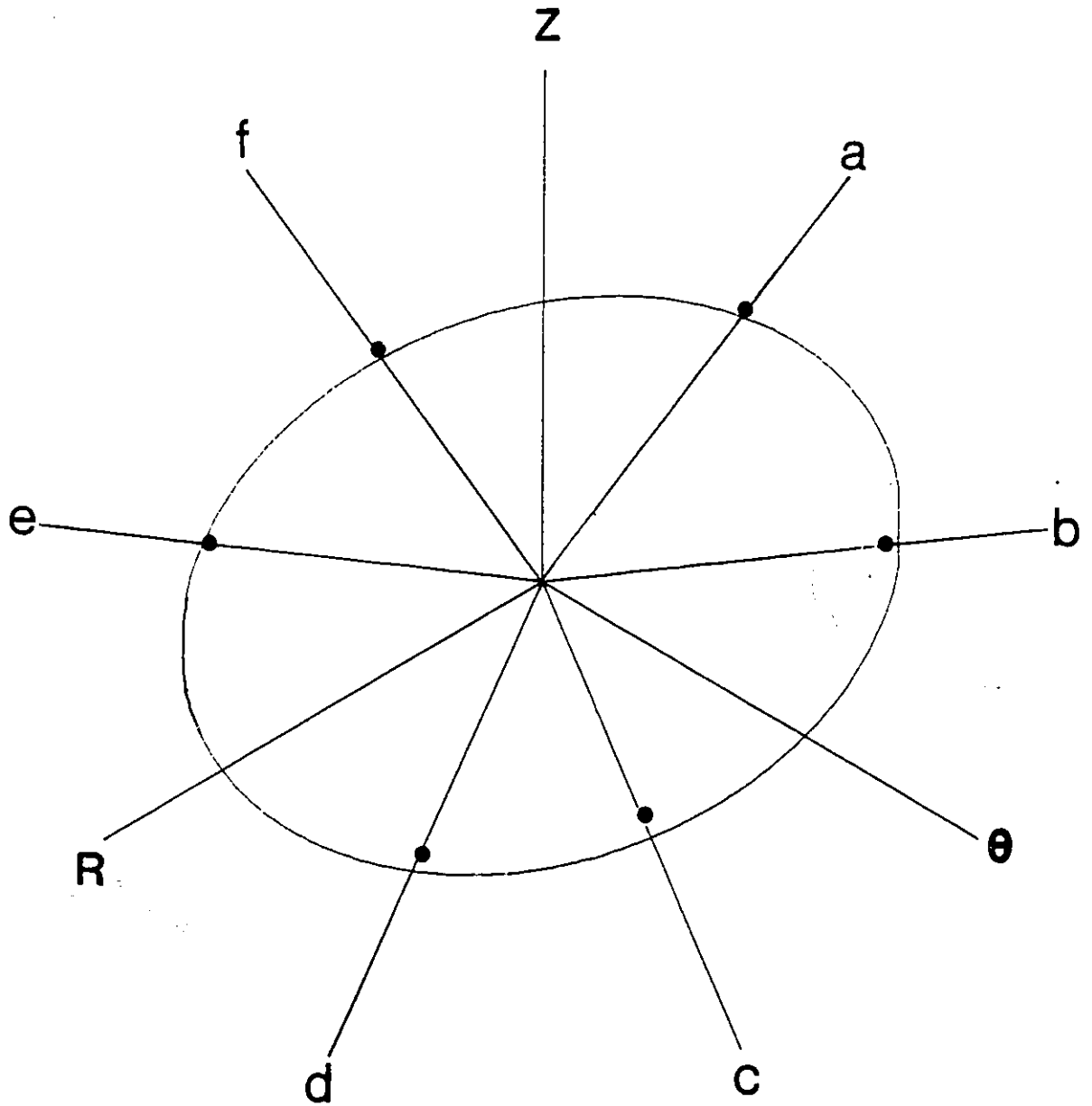


Figure 4.5 Flow surface diagram for Zircaloy-4 tubing annealed at 600°C for 10³ seconds.

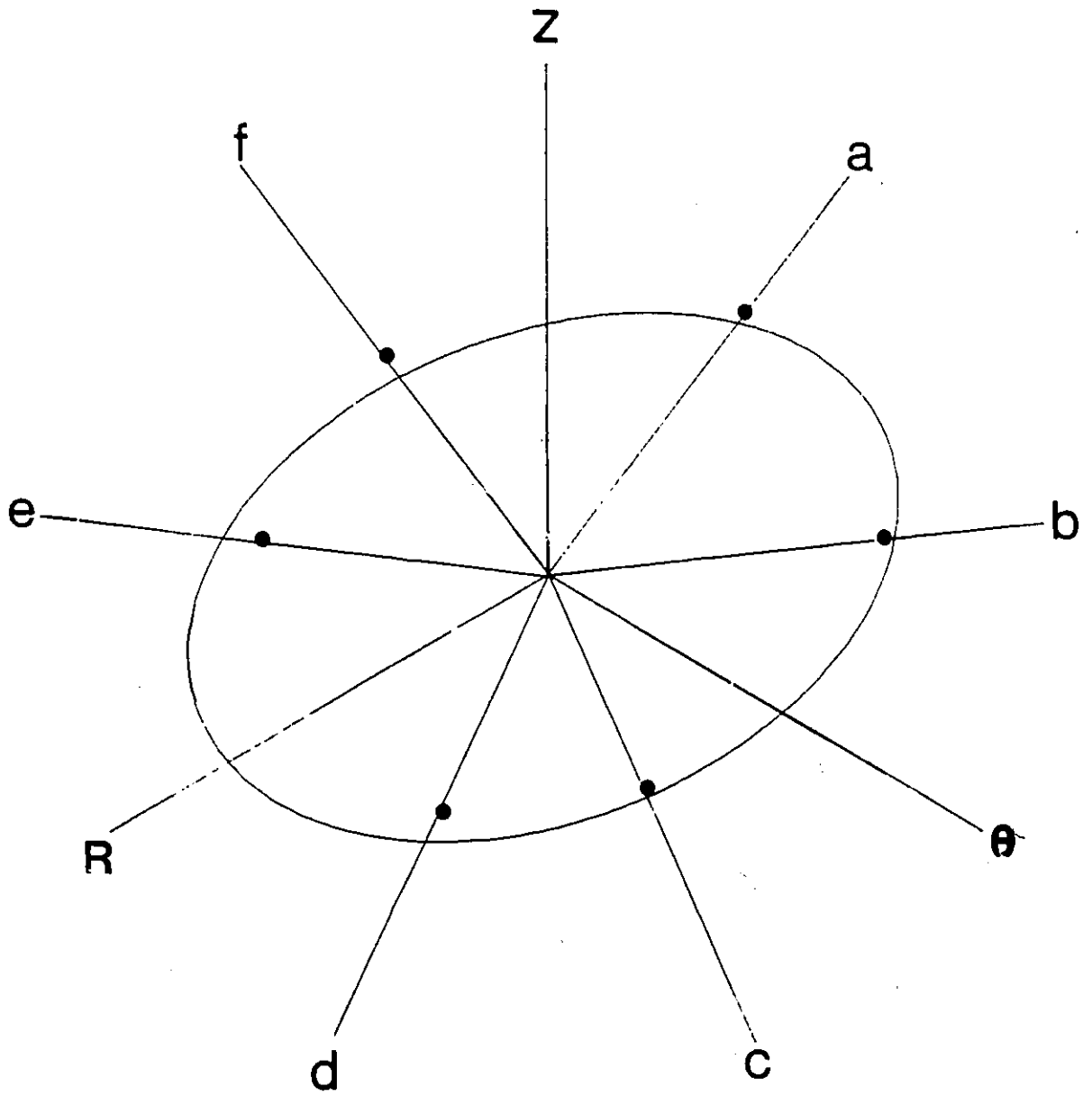


Figure 4.6 Flow surface diagram for Zircaloy-4 tubing annealed at 700°C for 10³ seconds.

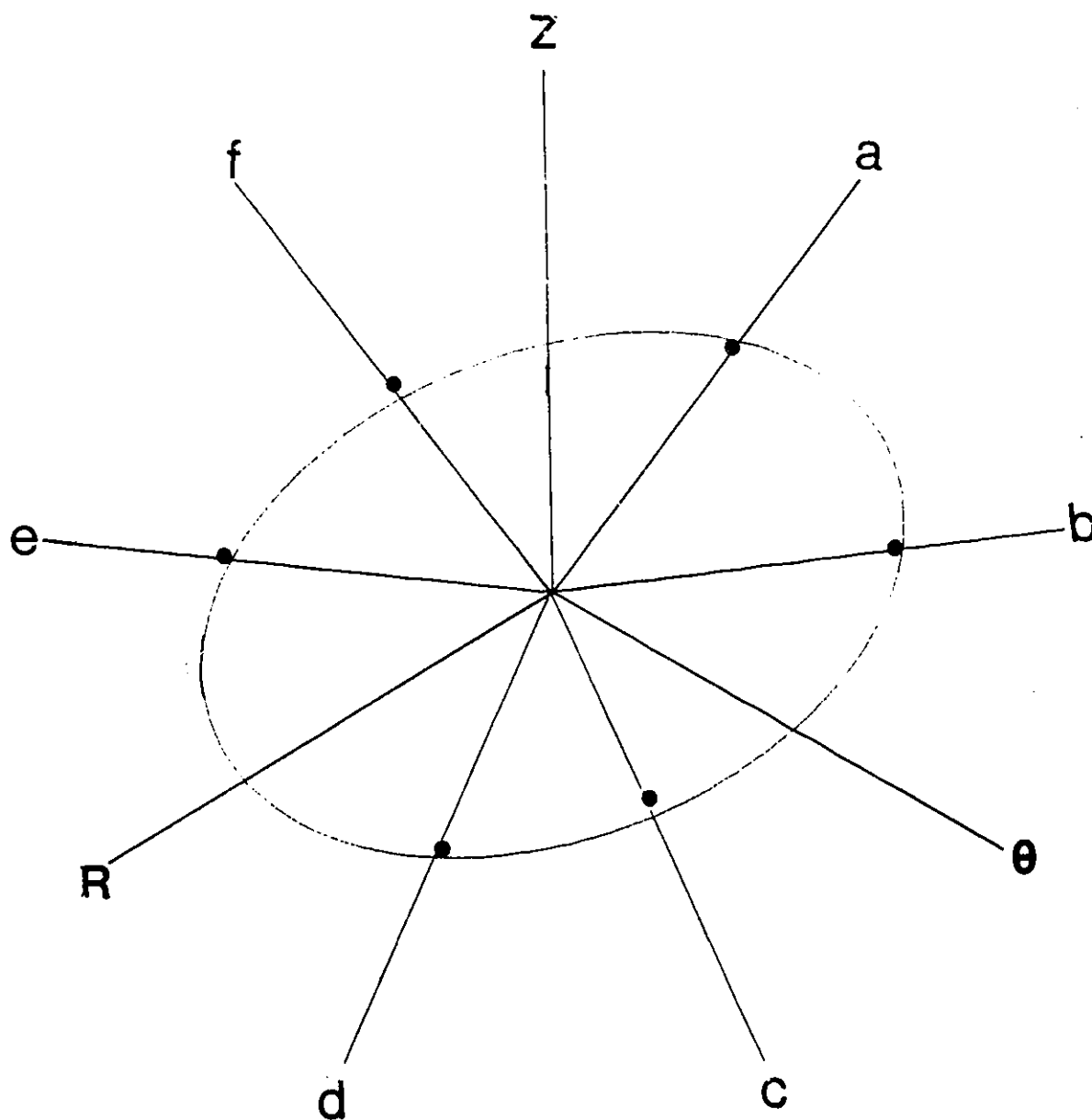


Figure 4.7 Flow surface diagram for Zircaloy-4 tubing annealed at 800°C for 10³ seconds.

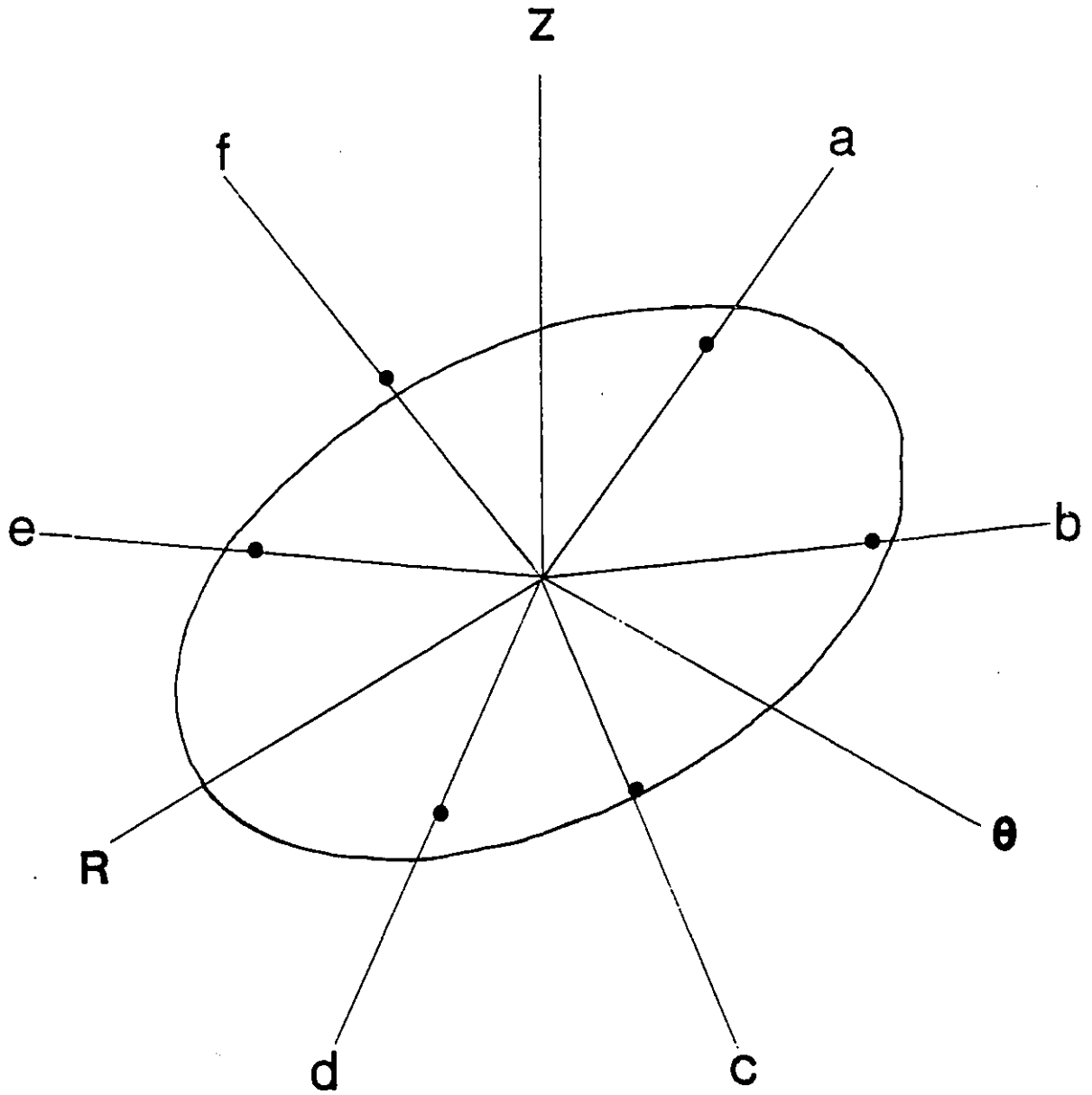


Figure 4.8 Flow surface diagram for Zircaloy-4 tubing annealed at 900°C for 10³ seconds.

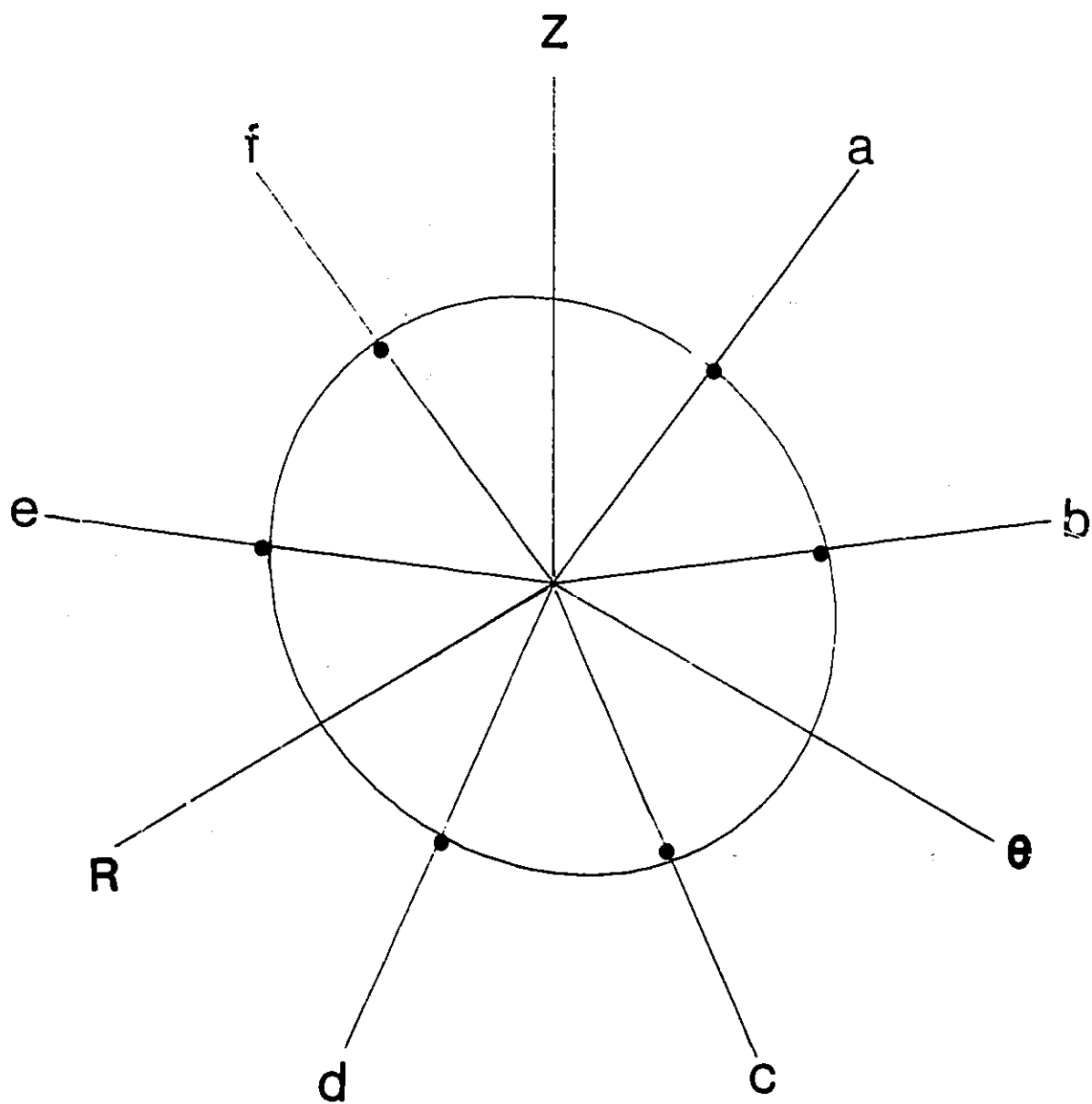


Figure 4.9 Flow surface diagram for Zircaloy-4 tubing annealed at 1000°C for 10³ seconds.

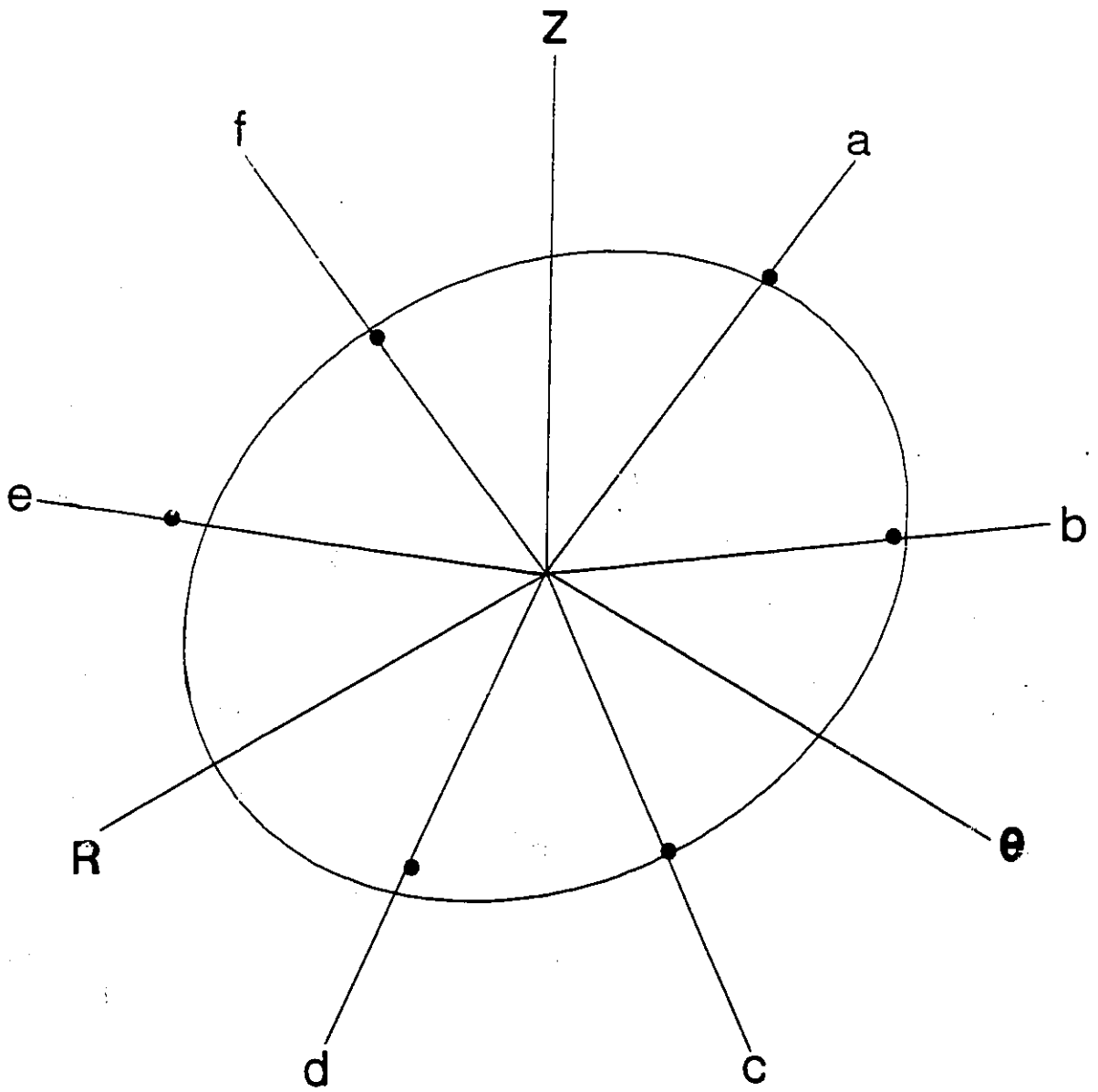


Figure 4.10 Flow surface diagram for Zircaloy-4 tubing annealed at 300°C for 10⁴ seconds.

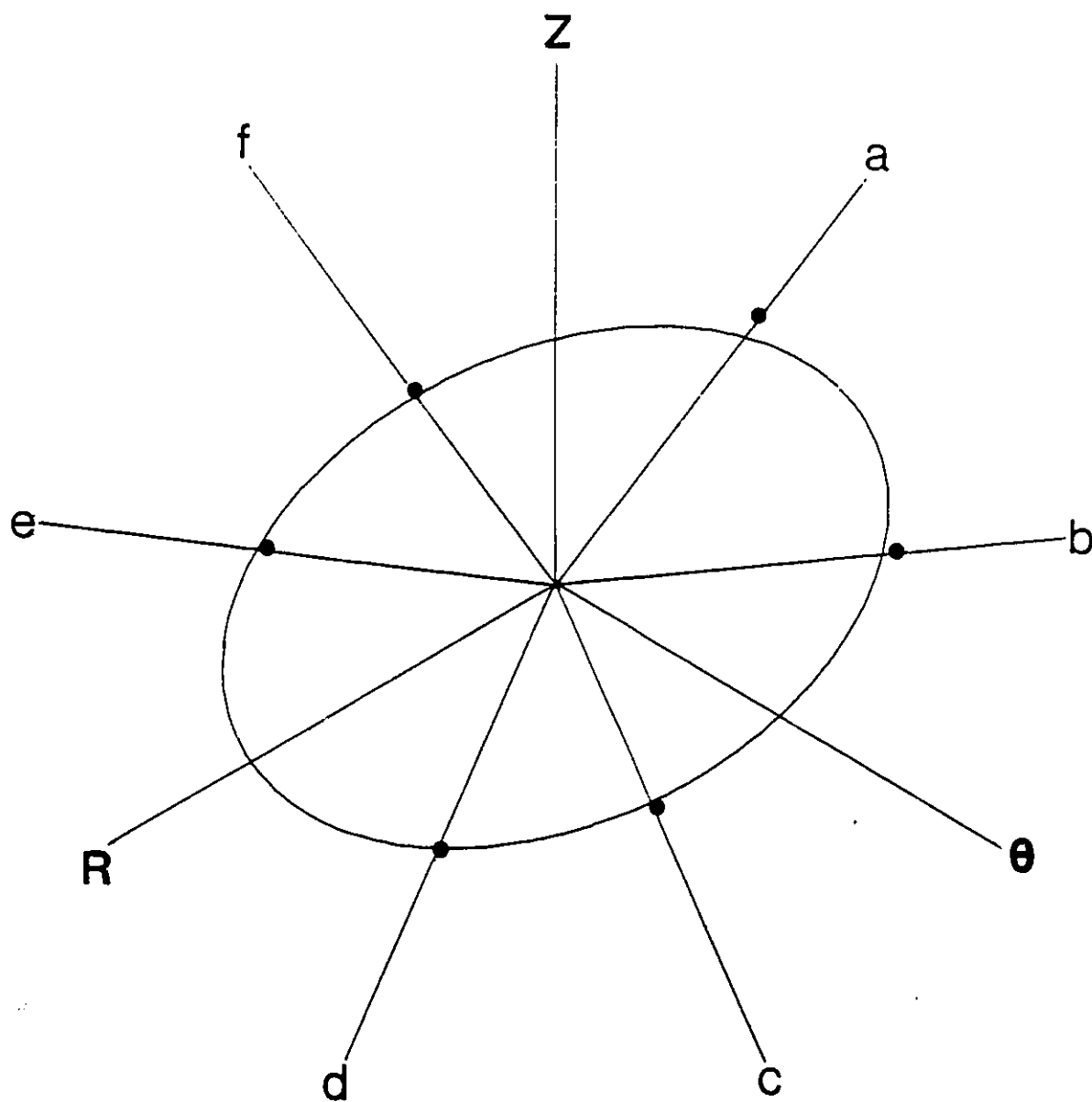


Figure 4.11 Flow surface diagram for Zircaloy-4 tubing annealed at 400°C for 10⁴ seconds.

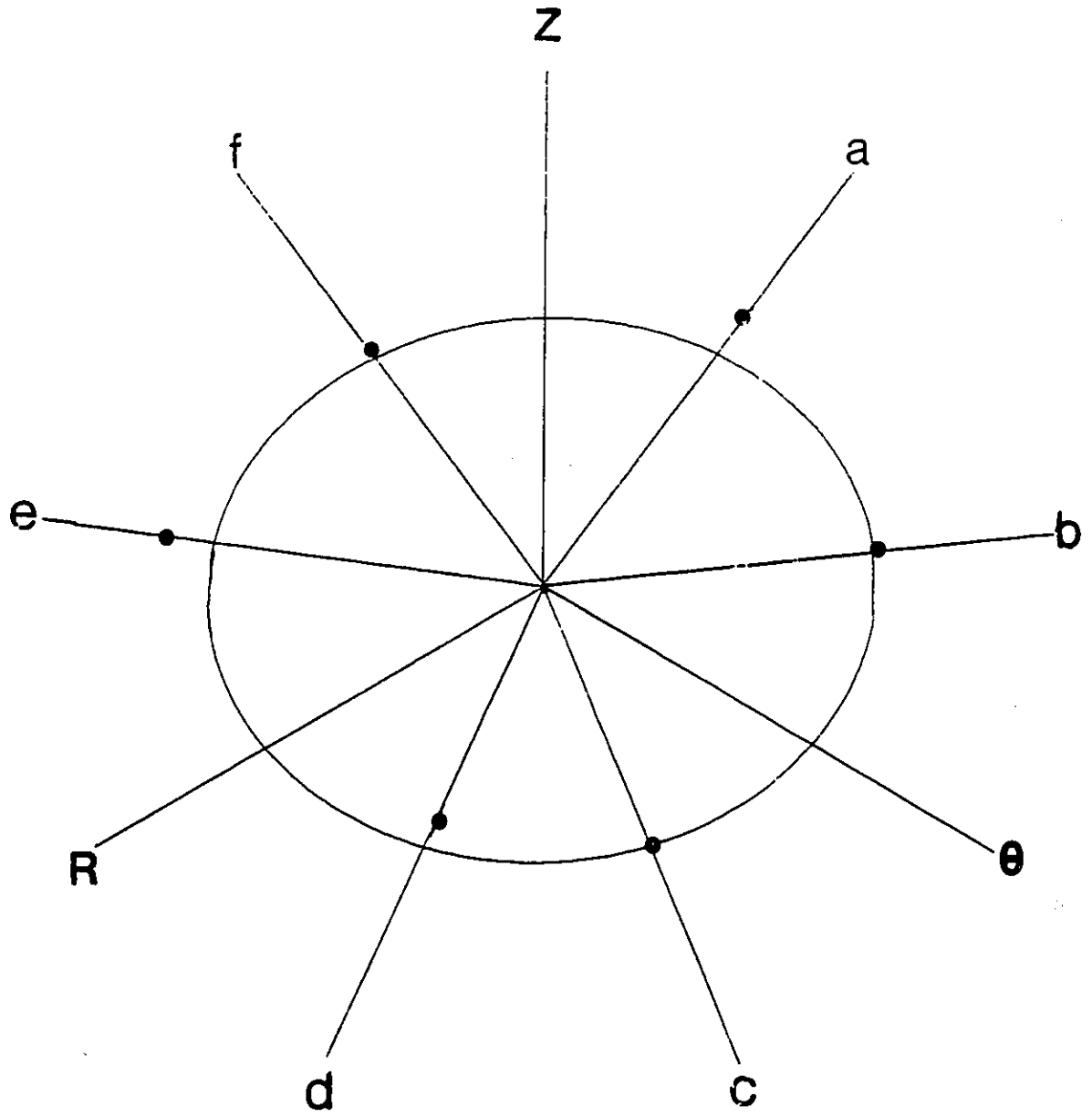


Figure 4.12 Flow surface diagram for Zircaloy-4 tubing annealed at 500°C for 10⁴ seconds.

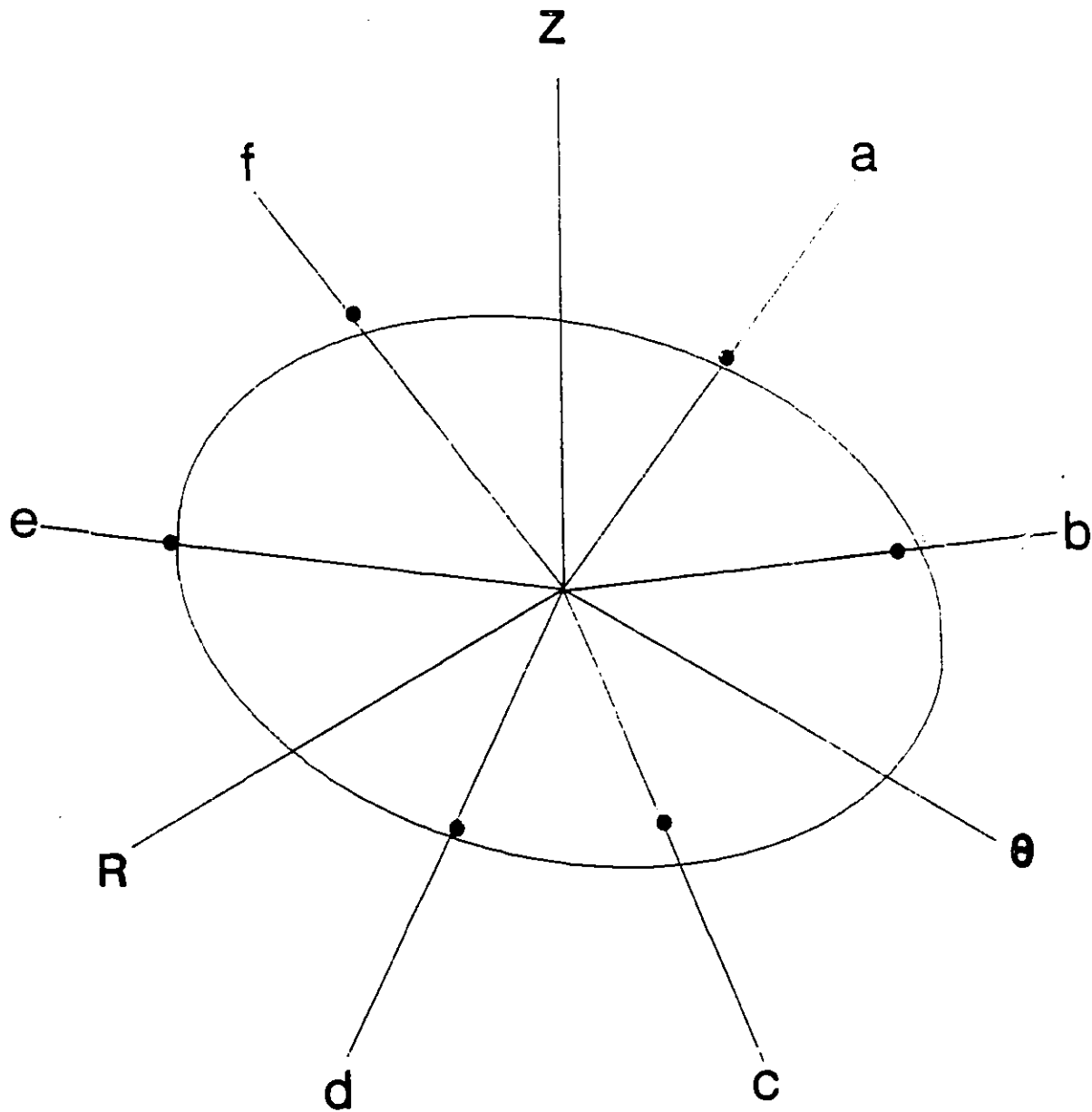


Figure 4.13 Flow surface diagram for Zircaloy-4 tubing annealed at 600°C for 10⁴ seconds.

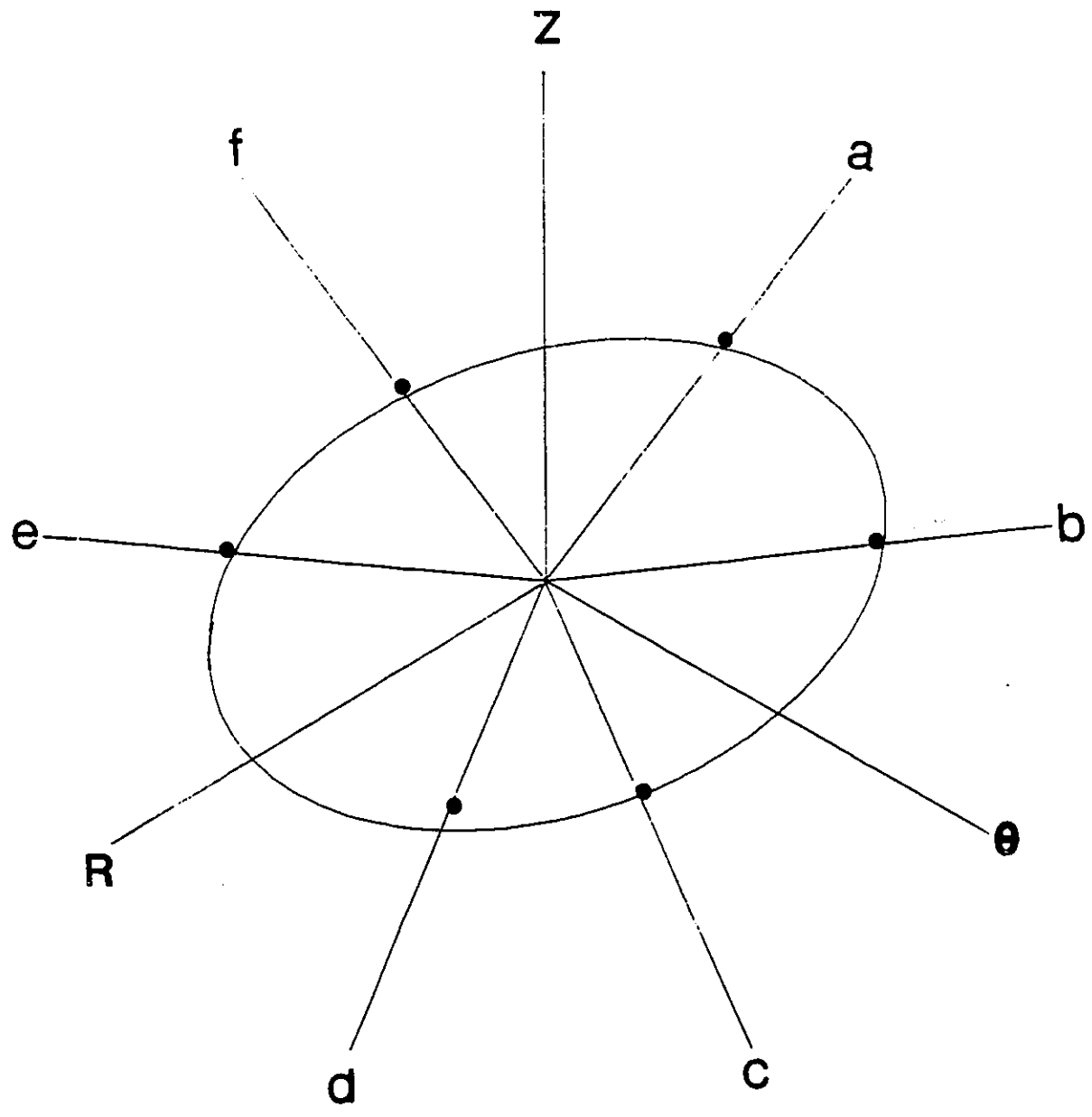


Figure 4.14 Flow surface diagram for Zircaloy-4 tubing annealed at 700°C for 10⁴ seconds.

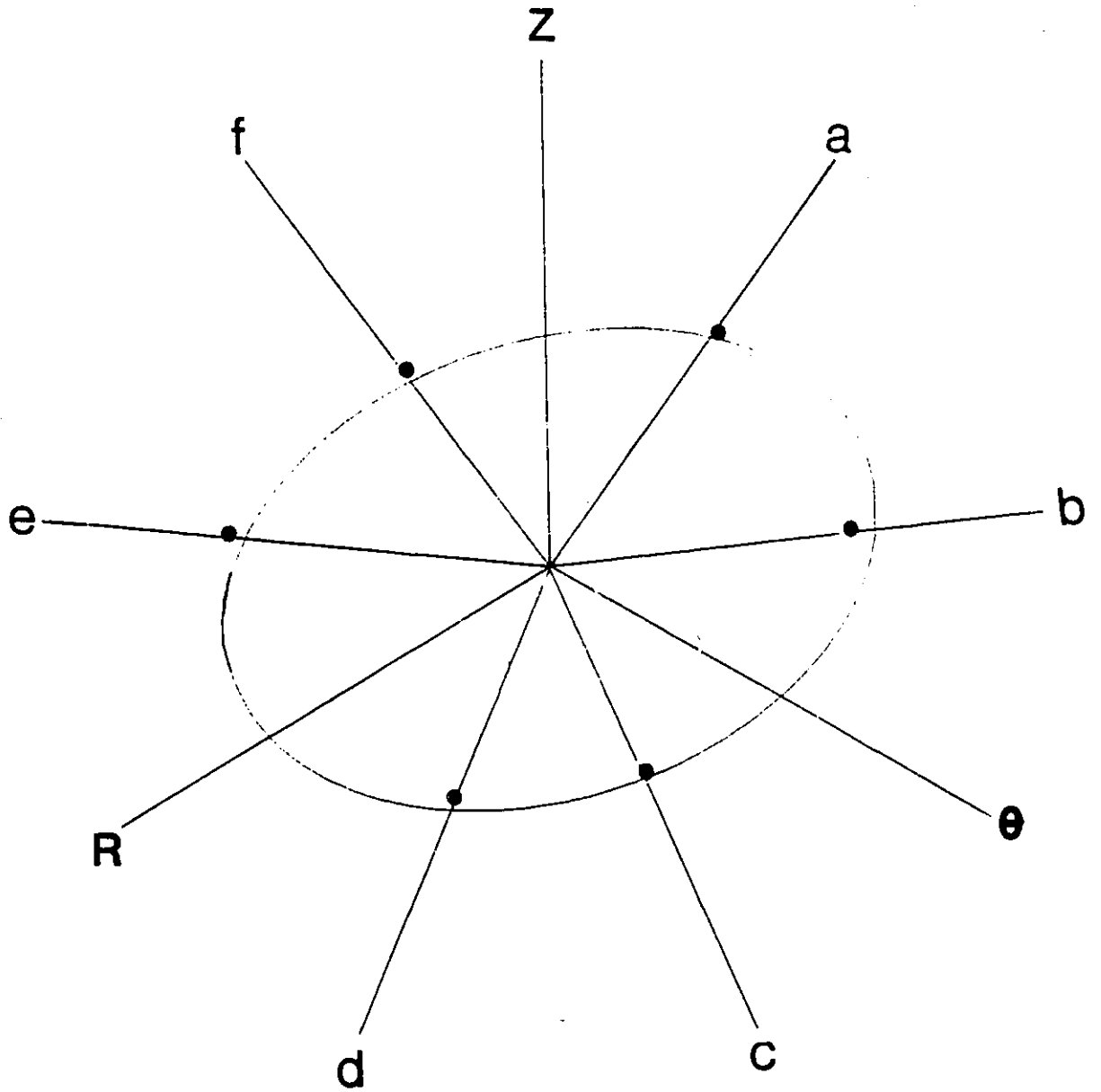


Figure 4.15 Flow surface diagram for Zircaloy-4 tubing annealed at 800°C for 10⁴ seconds.

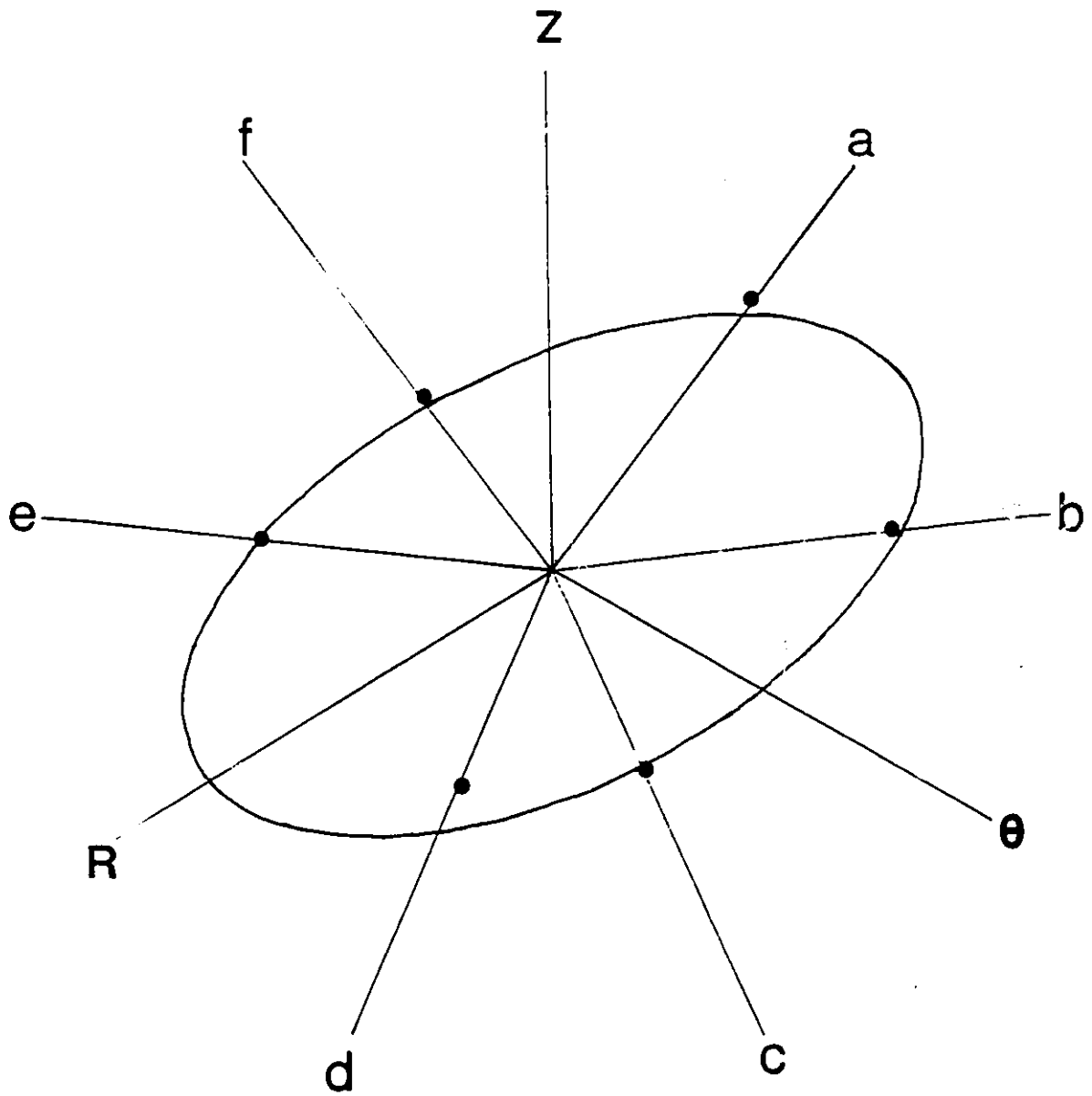


Figure 4.16 Flow surface diagram for Zircaloy-4 tubing annealed at 900°C for 10⁴ seconds.

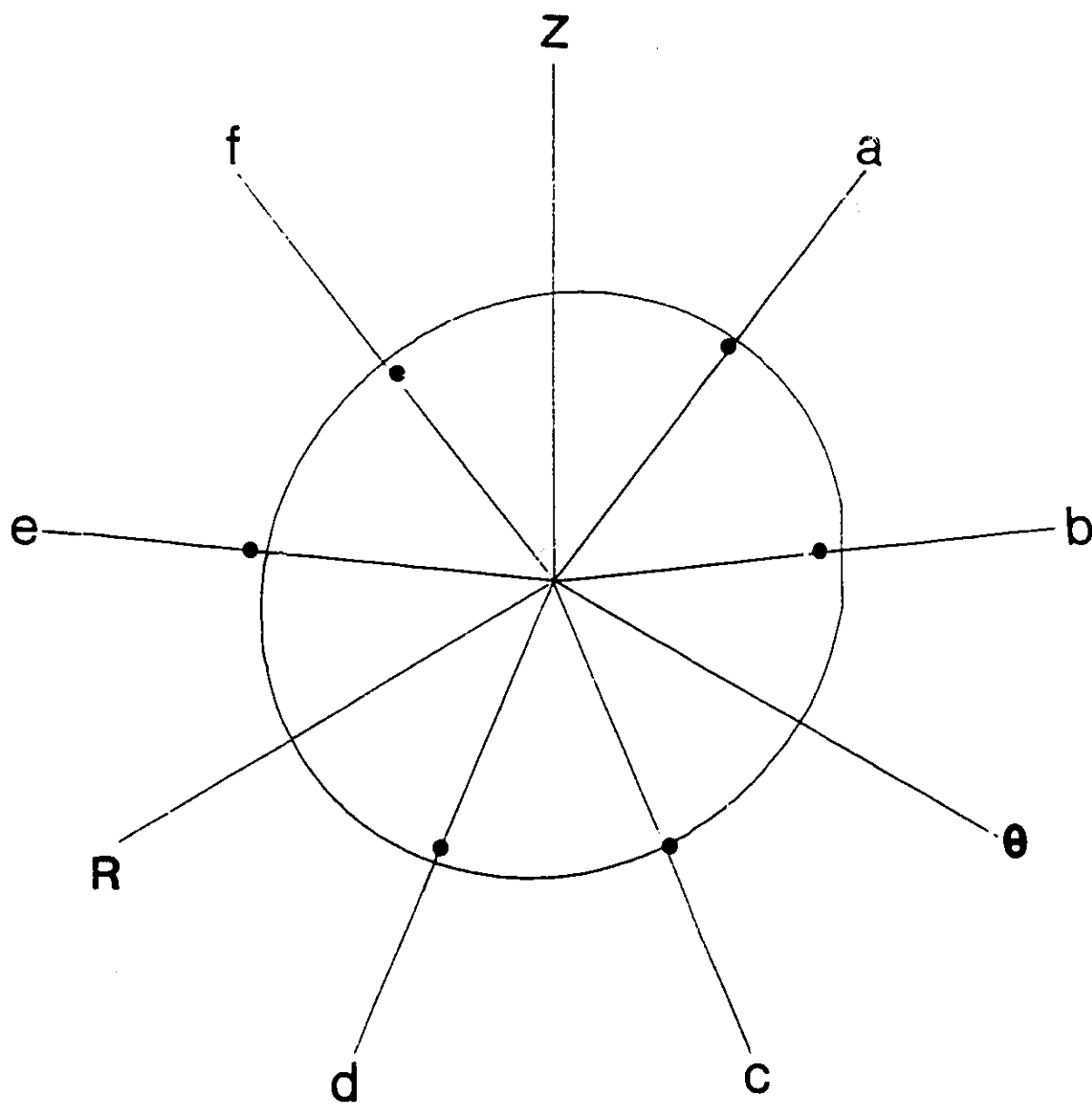


Figure 4.17 Flow surface diagram for Zircaloy-4 tubing annealed at 1000°C for 10⁴ seconds.

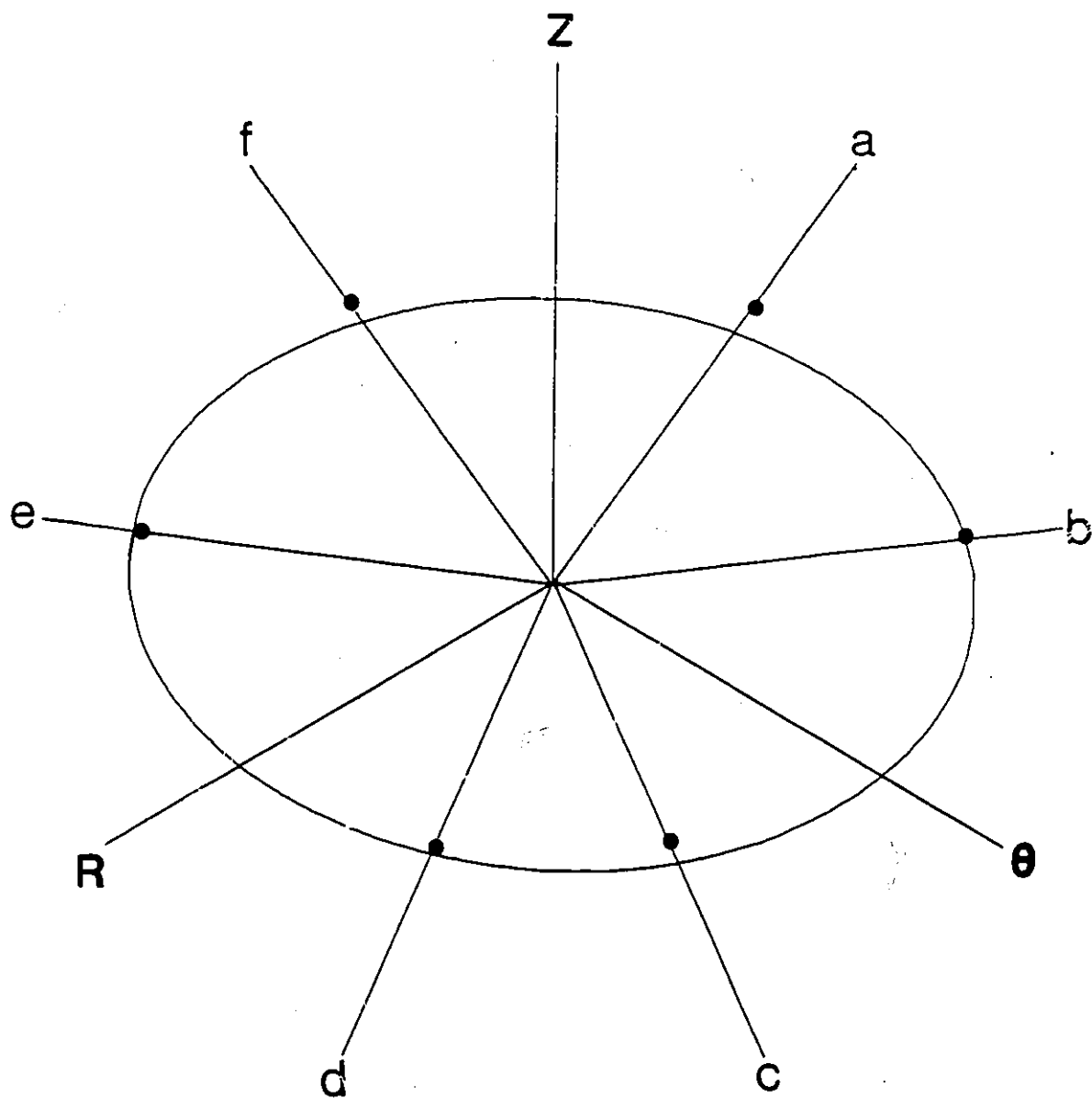


Figure 4.18 Flow surface diagram for Zircaloy-4 tubing annealed at 300°C for 10⁵ seconds.

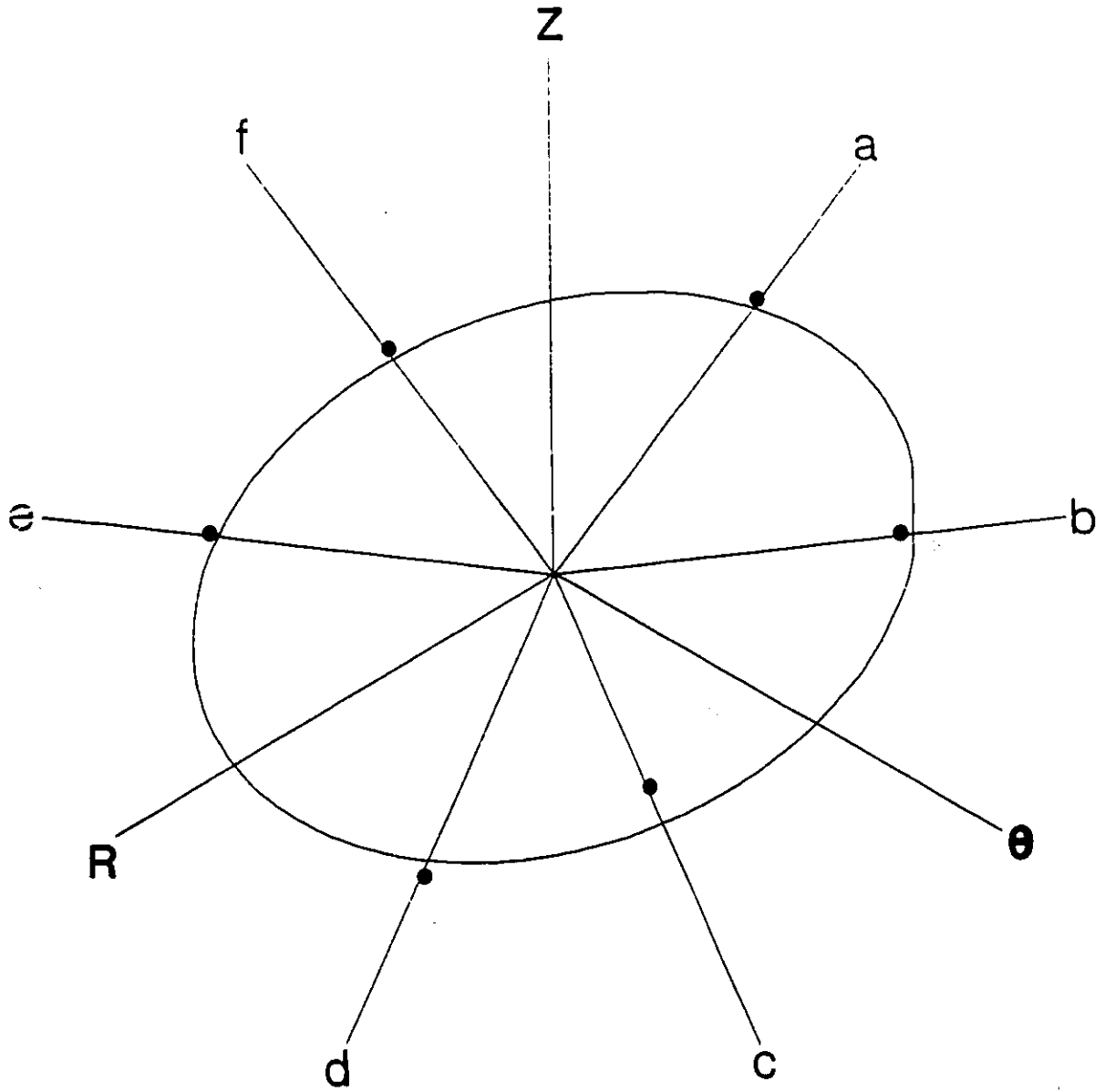


Figure 4.19 Flow surface diagram for Zircaloy-4 tubing annealed at 400°C for 10⁵ seconds.

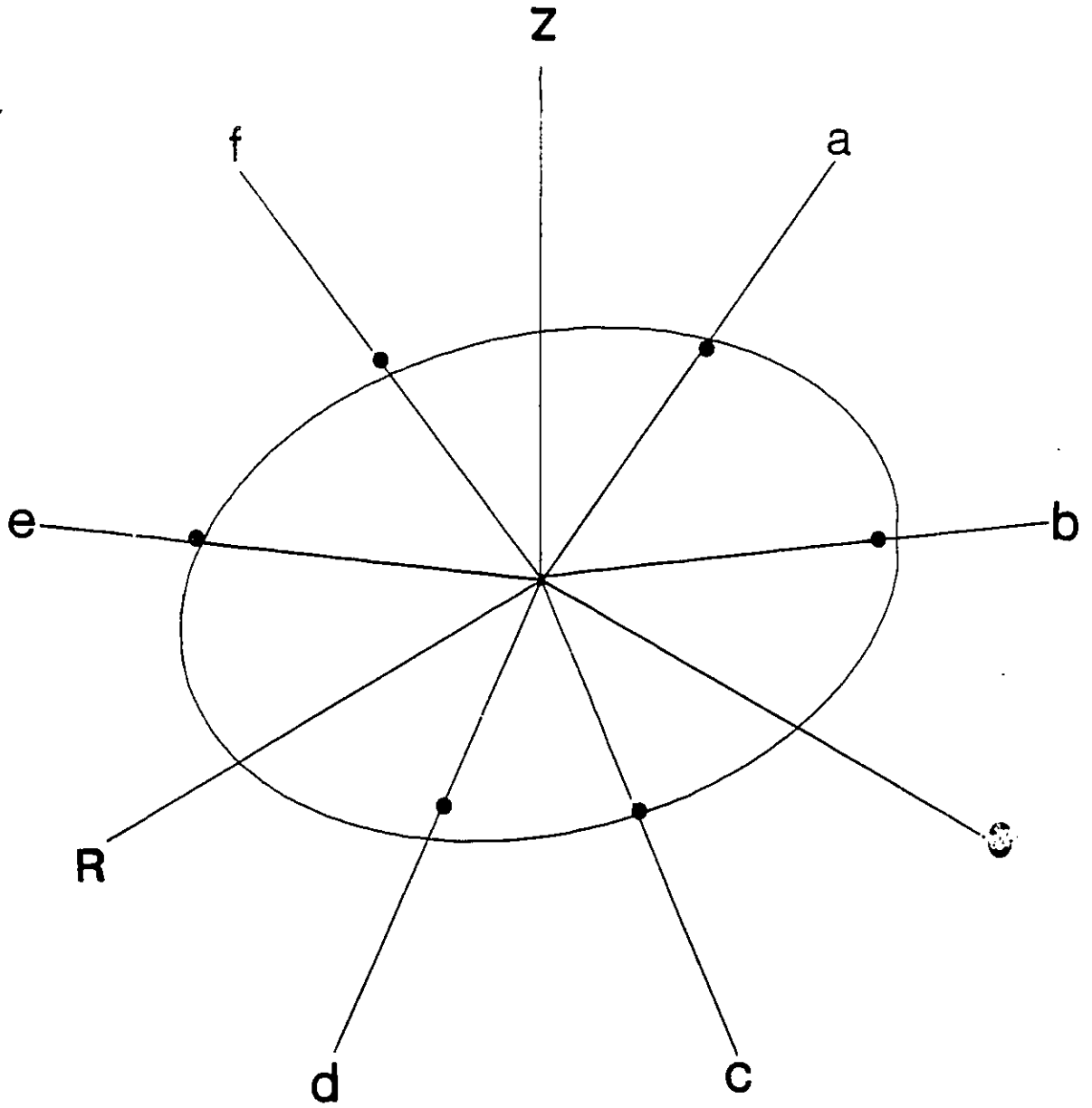


Figure 4.20 Flow surface diagram for Zircaloy-4 tubing annealed at 500°C for 10⁵ seconds.

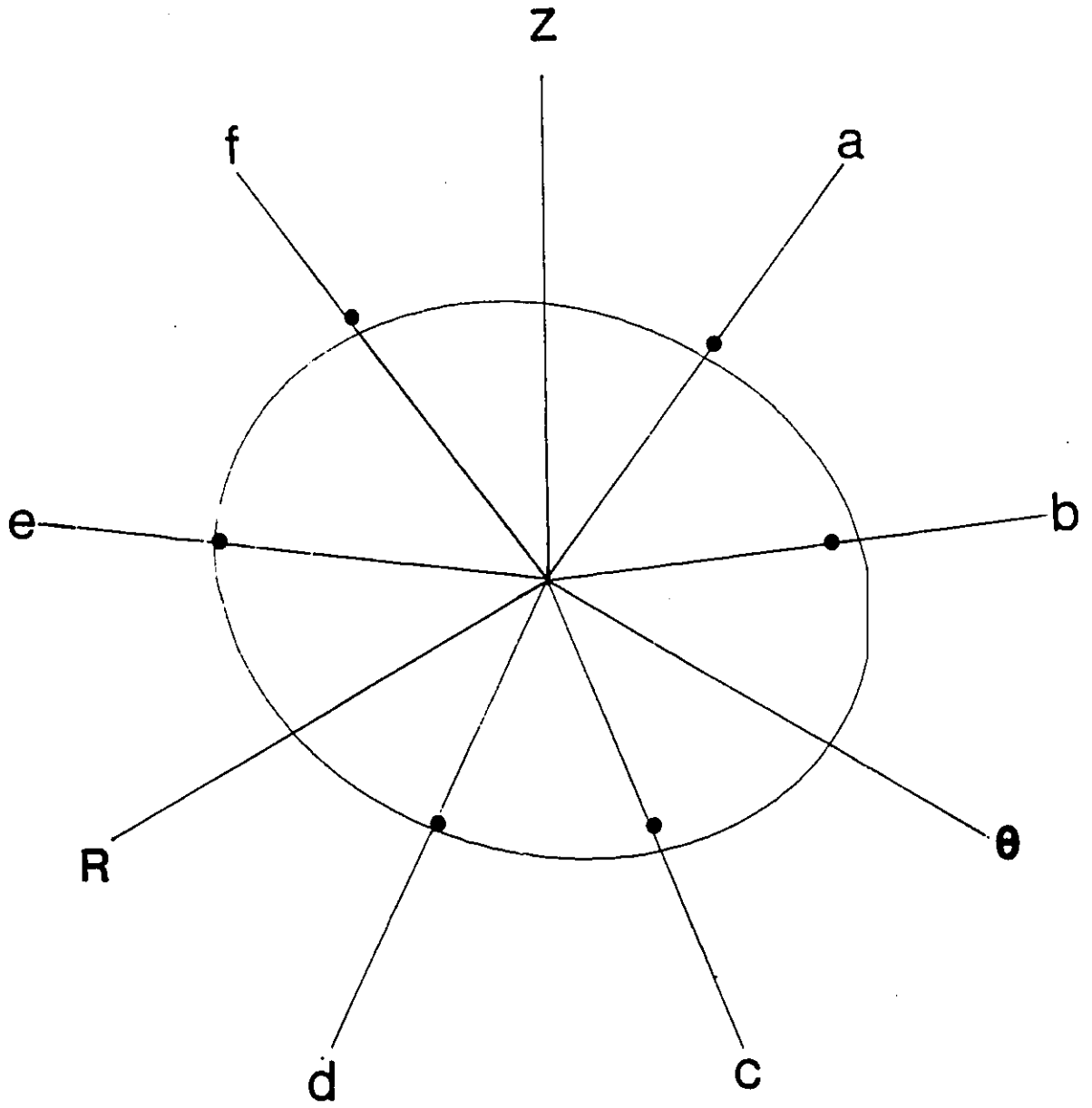


Figure 4.21 Flow surface diagram for Zircaloy-4 tubing annealed at 600°C for 10⁵ seconds.

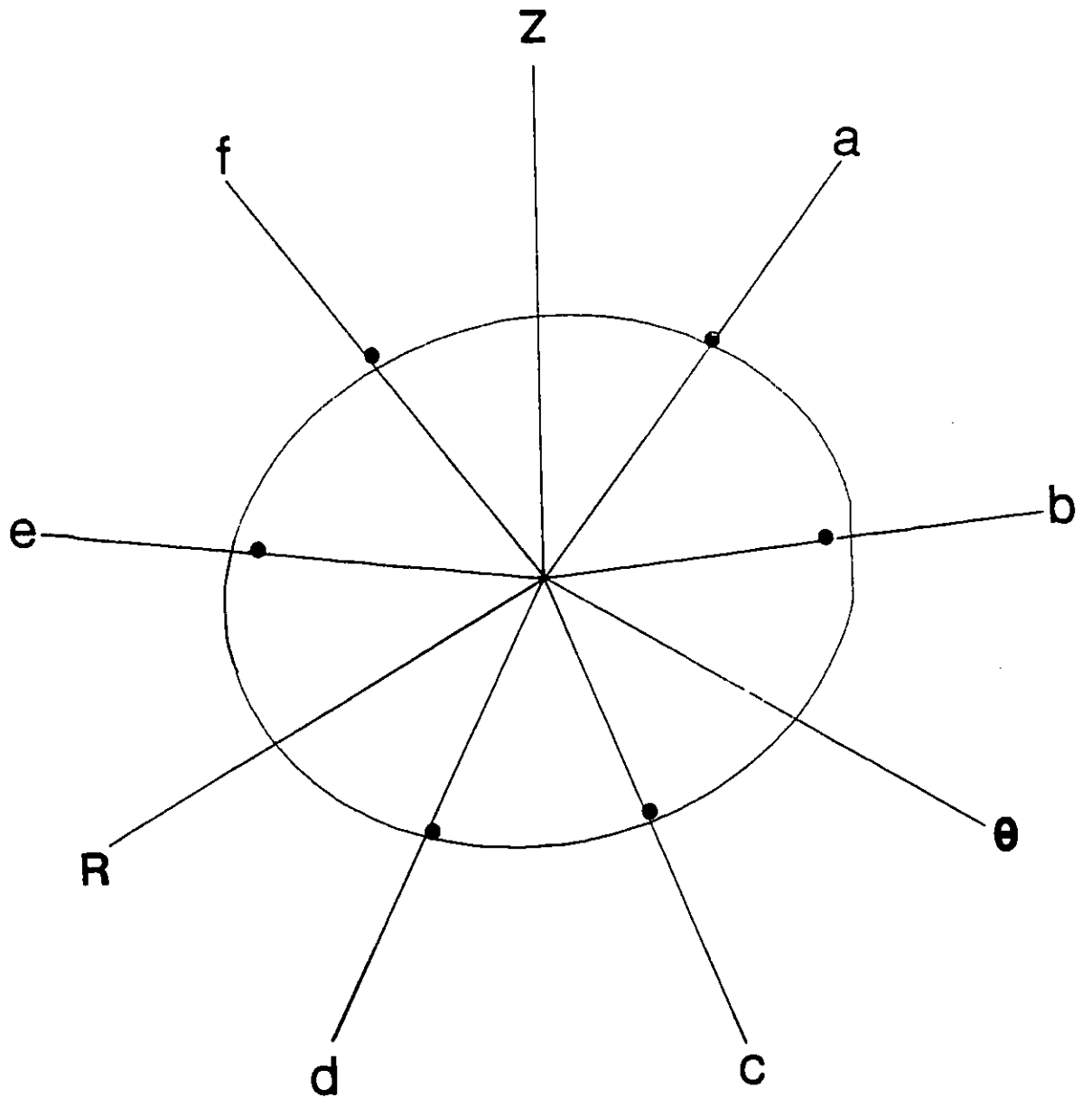


Figure 4.22 Flow surface diagram for Zircaloy-4 tubing annealed at 700°C for 10⁵ seconds.

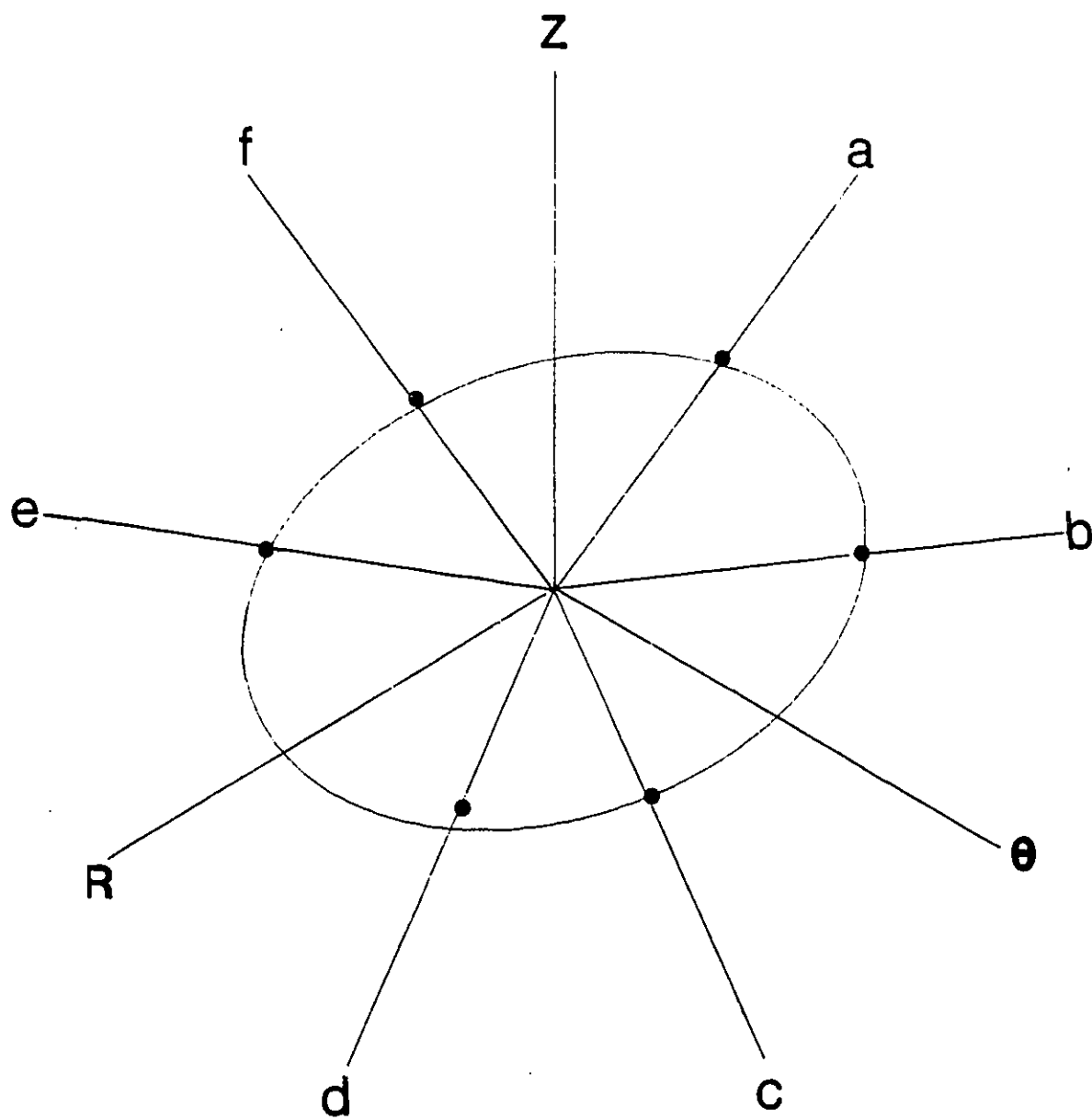


Figure 4.23 Flow surface diagram for Zircaloy-4 tubing annealed at 800°C for 10⁵ seconds.

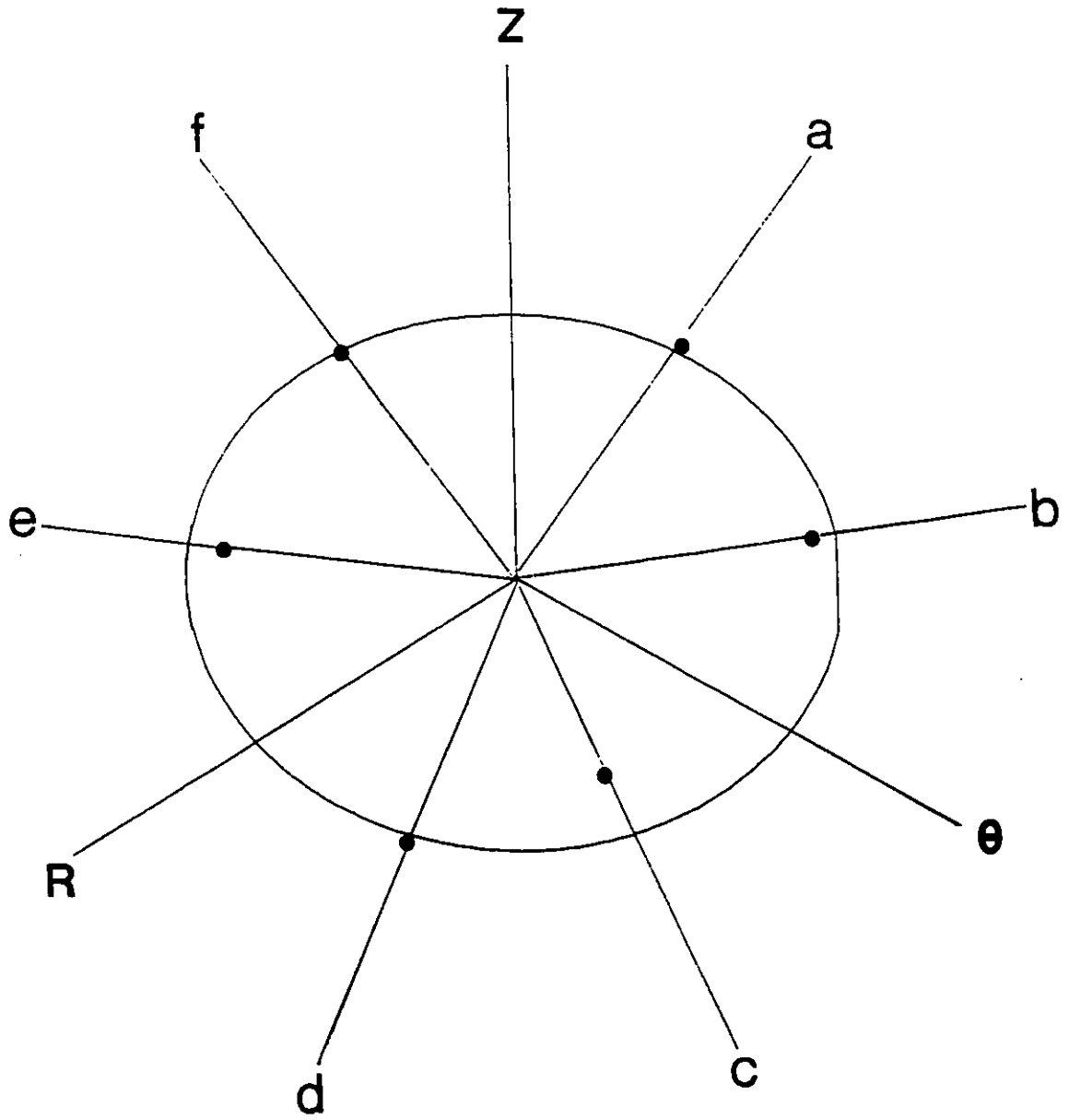


Figure 4.24 Flow surface diagram for Zircaloy-4 tubing annealed at 900°C for 10⁵ seconds.

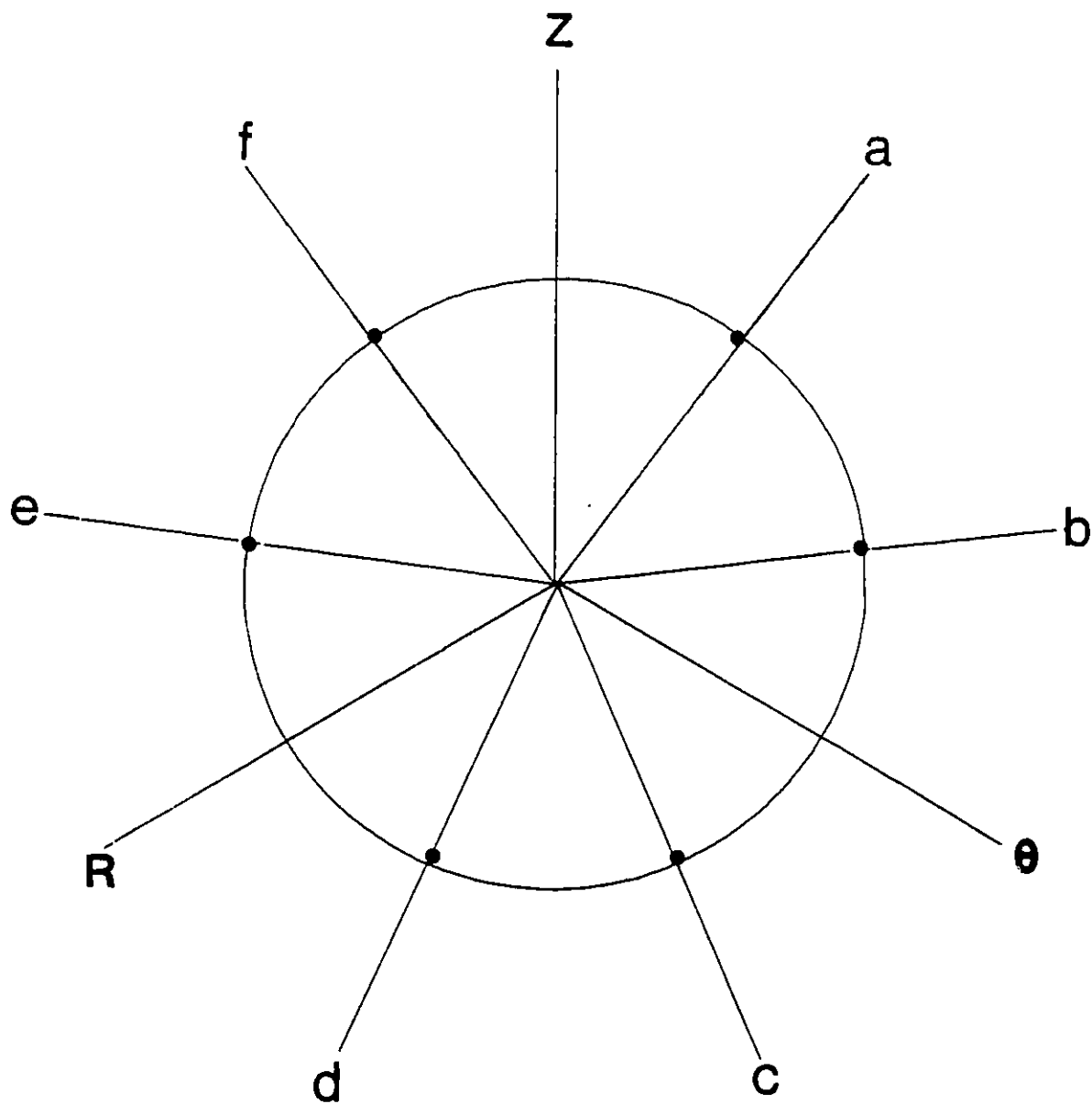


Figure 4.25 Flow surface diagram for Zircaloy-4 tubing annealed at 1000°C for 10⁵ seconds.

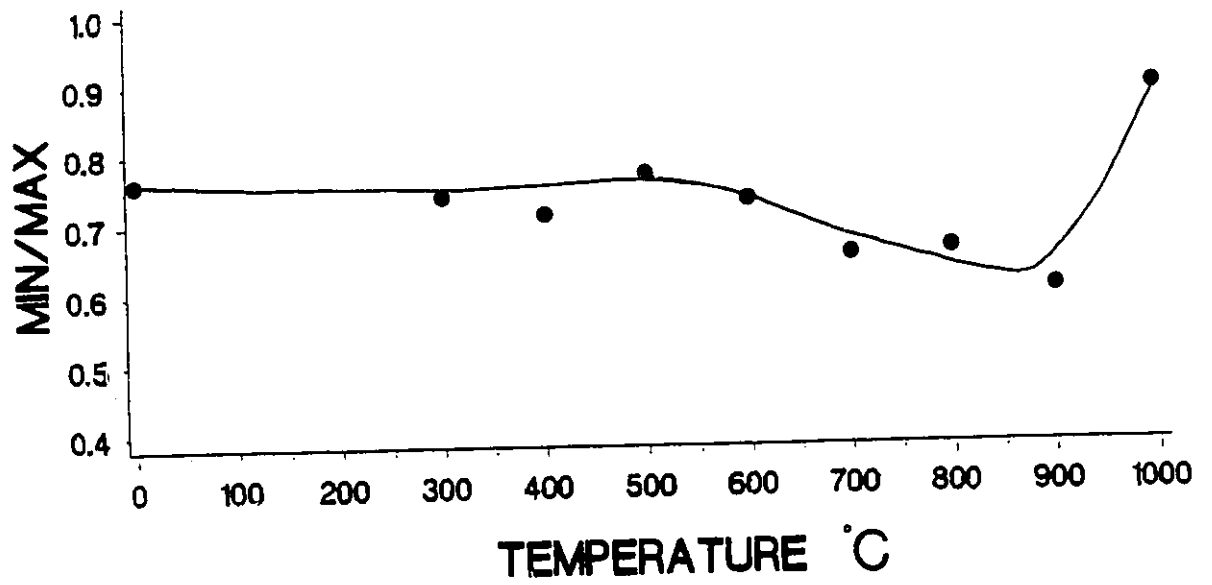


Figure 4.26 The mechanical anisotropy ratio, for Zircaloy-4 tubing, vs. annealing temperature for 10^3 seconds annealing time.

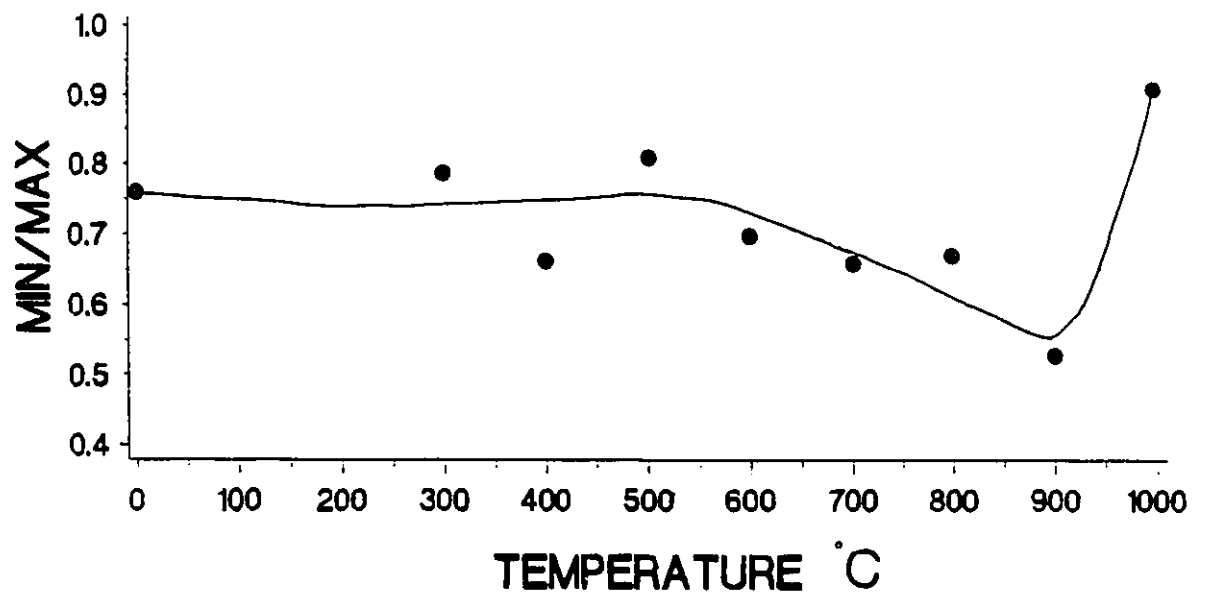


Figure 4.27 The mechanical anisotropy ratio, for Zircaloy-4 tubing, vs. annealing temperature for 10^4 seconds annealing time.

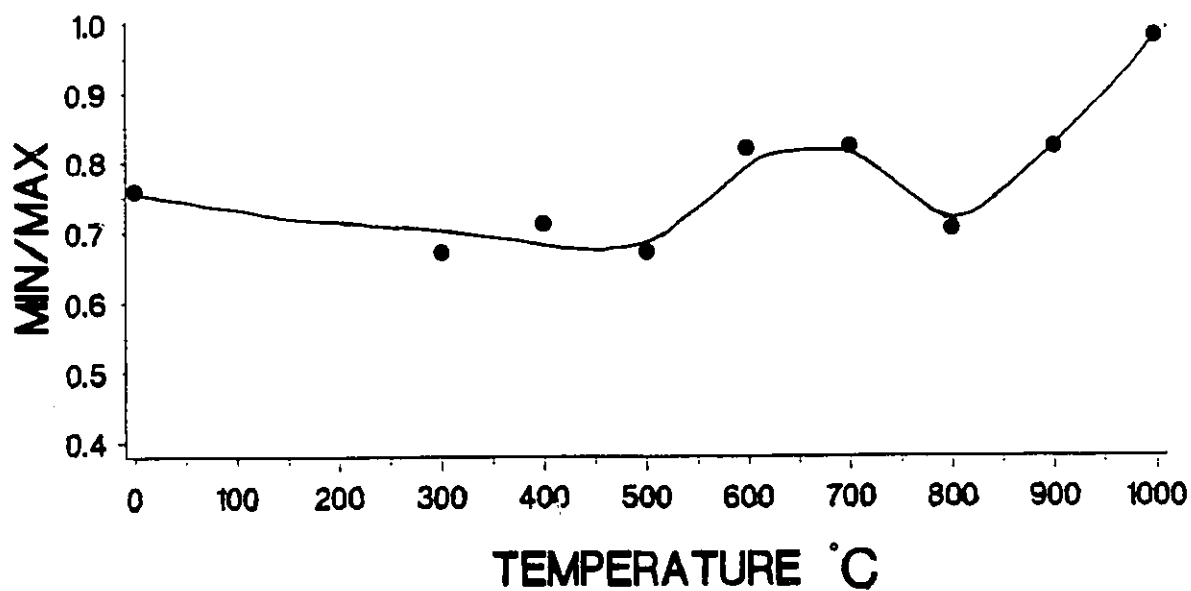


Figure 4.28 The mechanical anisotropy ratio, for Zircaloy-4 tubing, vs. annealing temperature for 10^5 seconds annealing time.

▲ AXIAL
● RADIAL
◆ TANGENTIAL

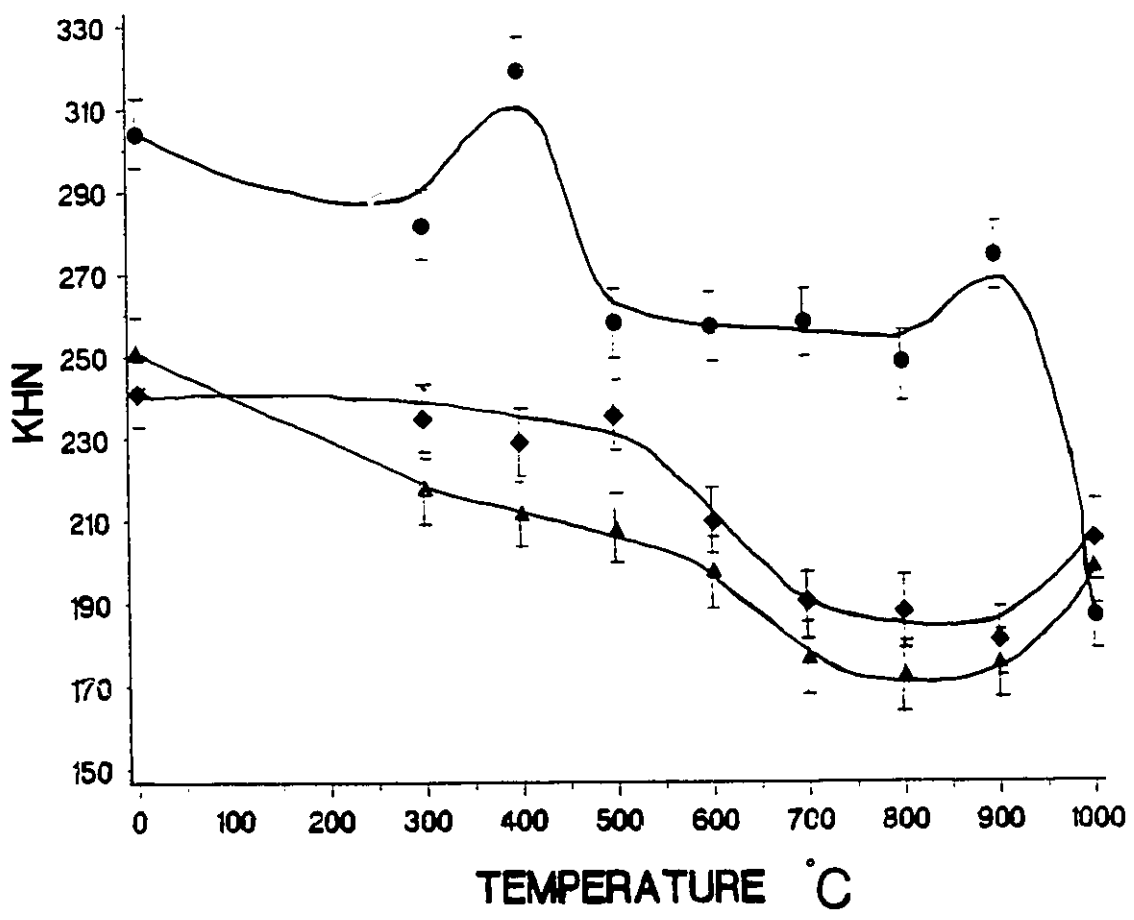


Figure 4.29 KHN, in major directions, vs. annealing temperature for Zircaloy-4 tubing for an annealing time of 10^3 seconds.

▲ L₁IAL
 ● RADIAL
 ◆ TANGENTIAL

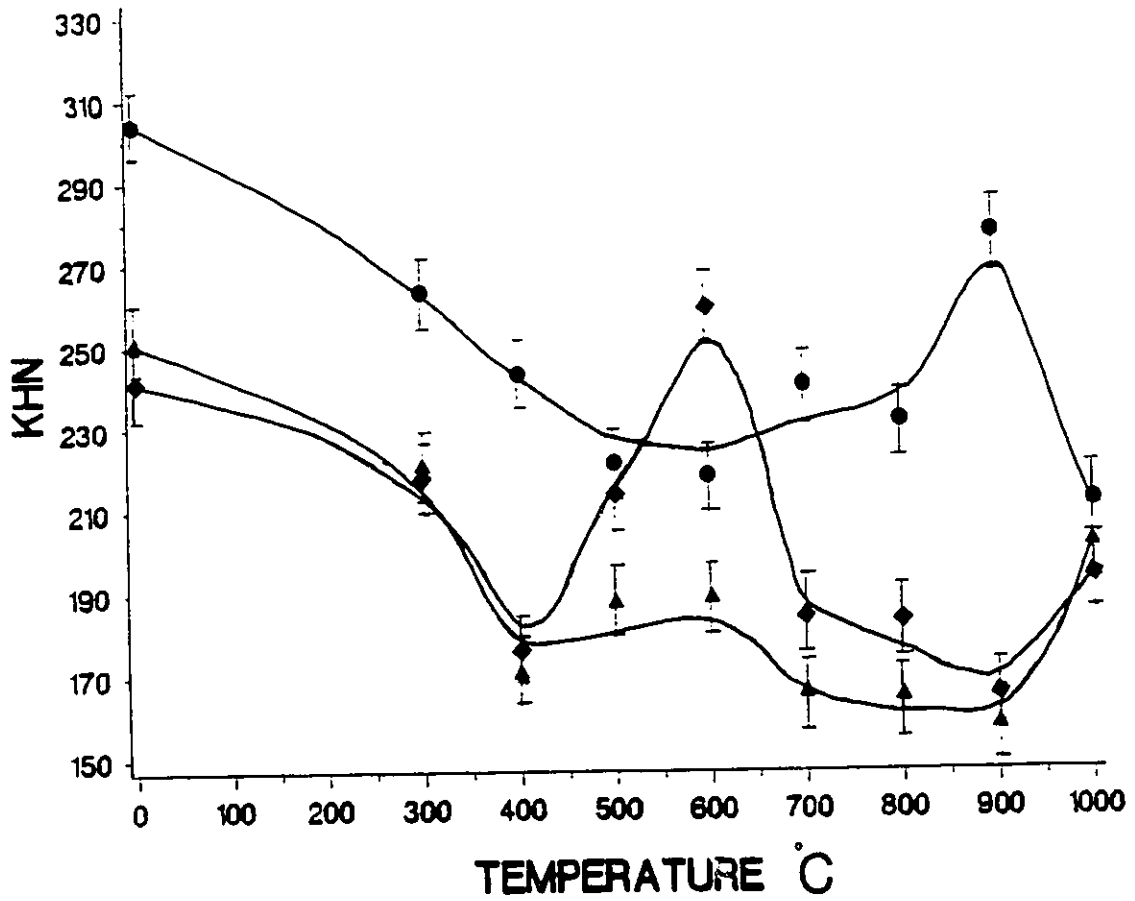


Figure 4.30 KHN, in major directions, vs. annealing temperature for Zircaloy-4 tubing for an annealing time of 10^4 seconds.

▲ AXIAL
● RADIAL
◆ TANGENTIAL

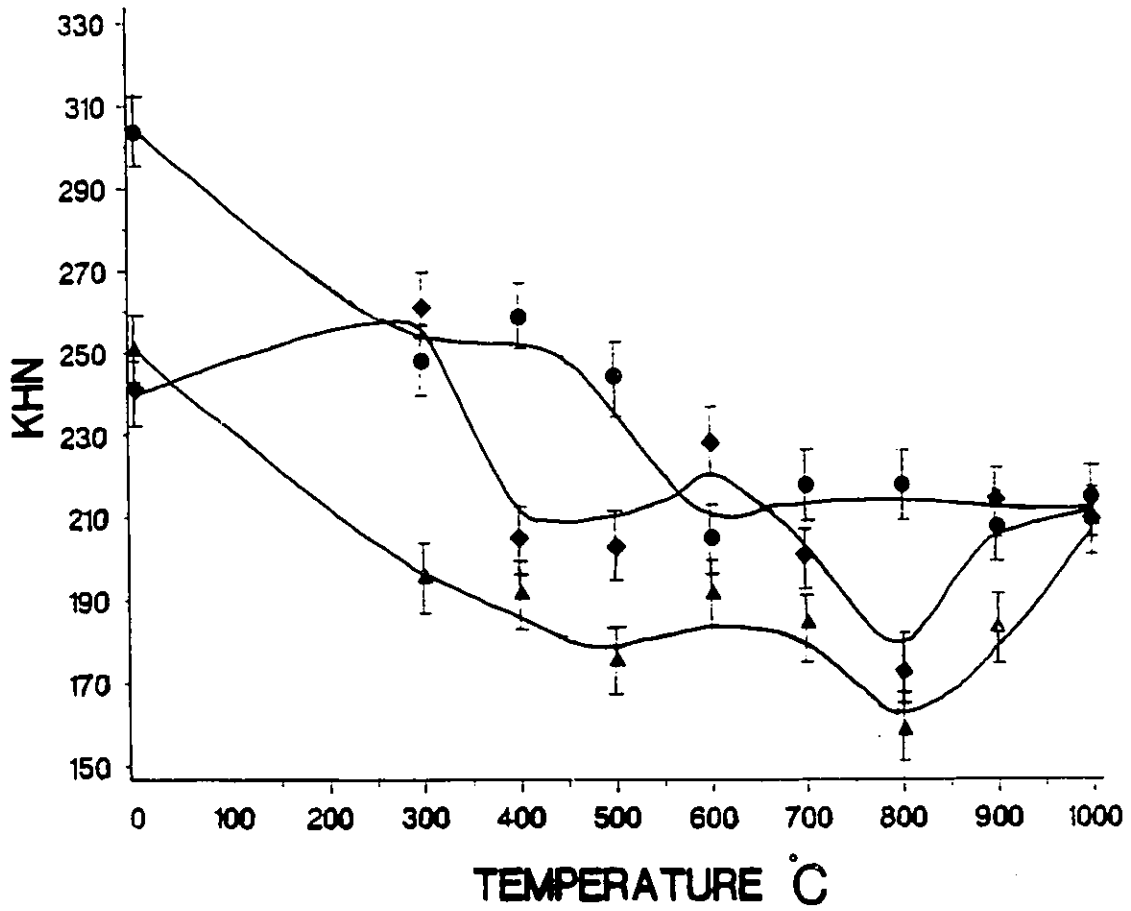


Figure 4.31 KHN, in major directions, vs. annealing temperature for Zircaloy-4 tubing for an annealing time of 10^5 seconds.

▲ AXIAL
● RADIAL
◆ TANGENTIAL

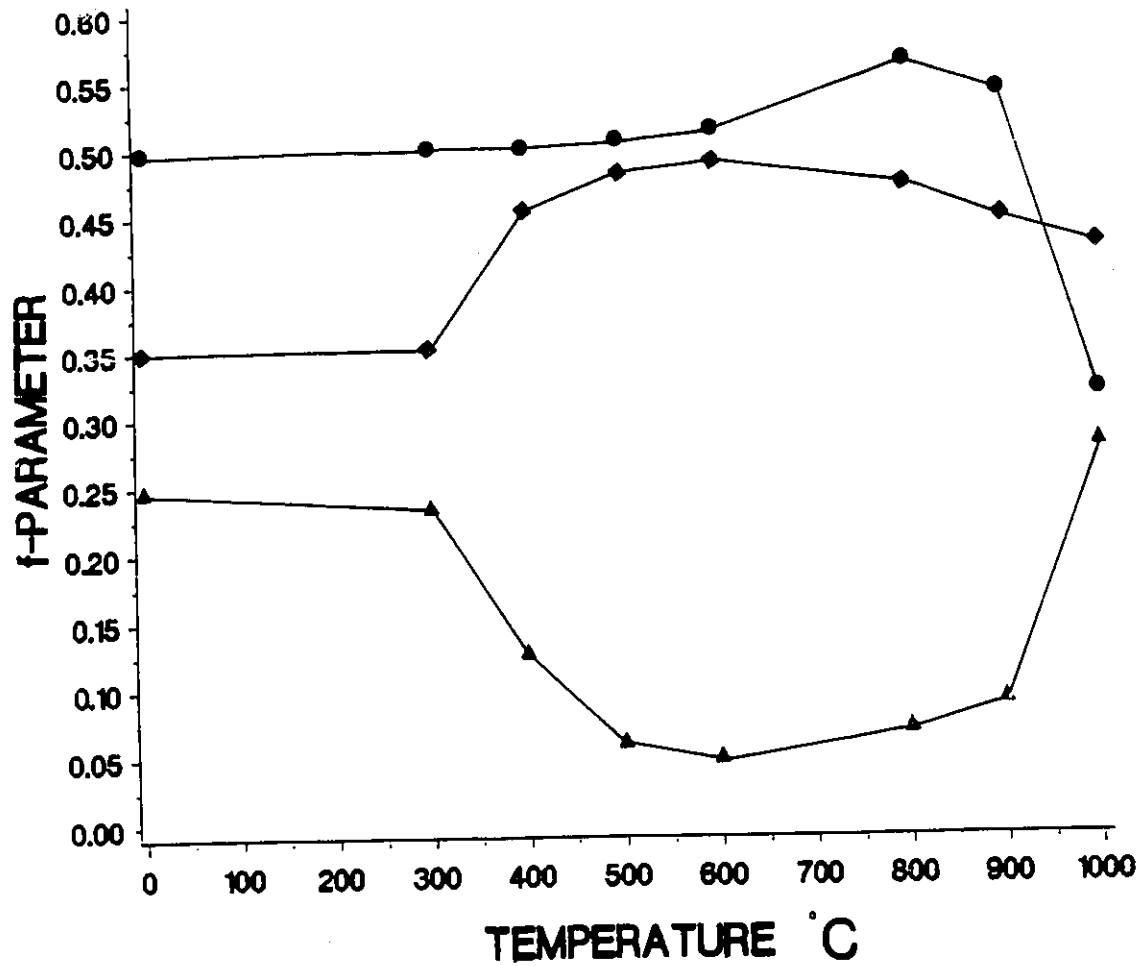


Figure 4.32 The f-parameter, in major directions, vs. annealing temperature for Zircaloy-4 tubing for an annealing time of 10^3 seconds.

▲ AXIAL
● RADIAL
◆ TANGENTIAL

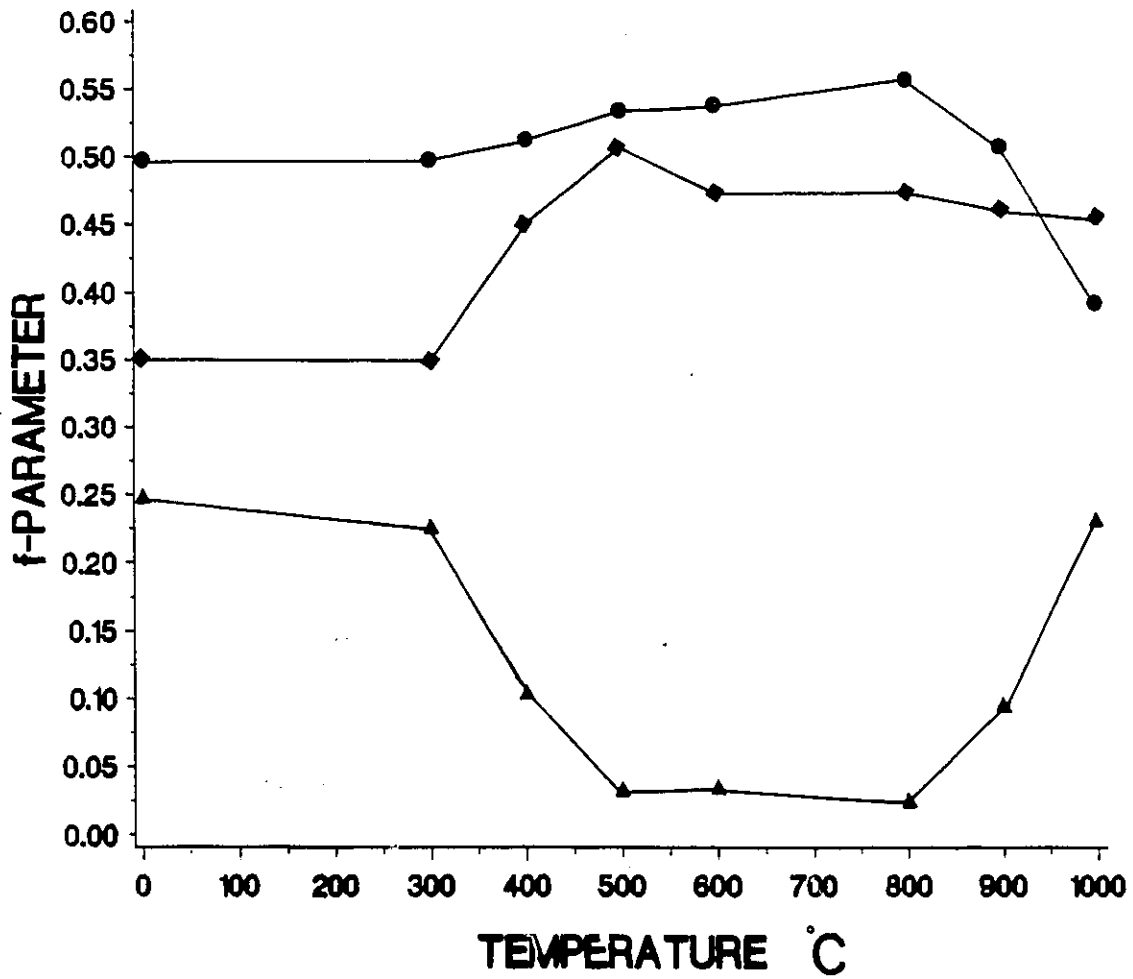


Figure 4.33 The f-parameter, in major directions, vs. annealing temperature for Zircaloy-4 tubing for an annealing time of 10^4 seconds.

▲ AXIAL
● RADIAL
◆ TANGENTIAL

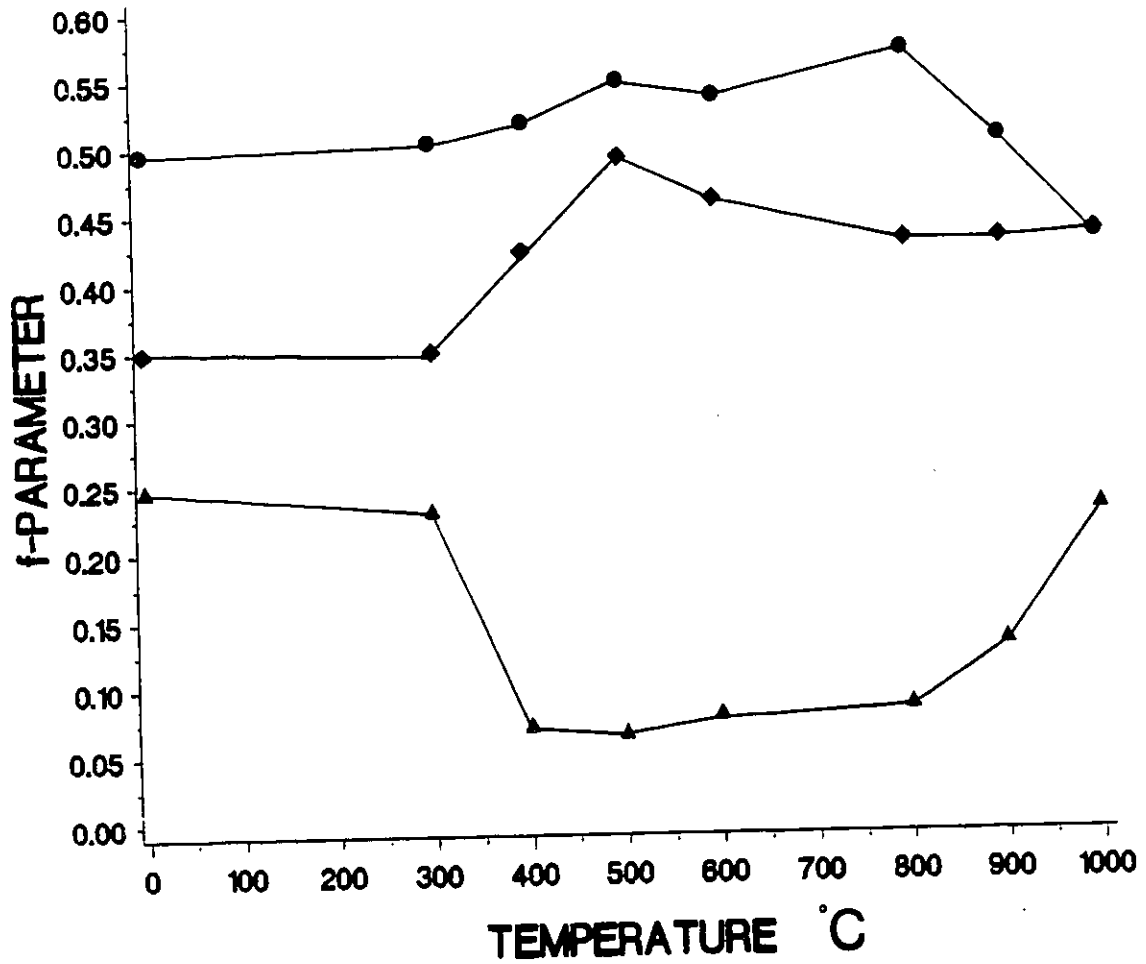


Figure 4.34 The f-parameter, in major directions, vs. annealing temperature for Zircaloy-4 tubing for an annealing time of 10^5 seconds.

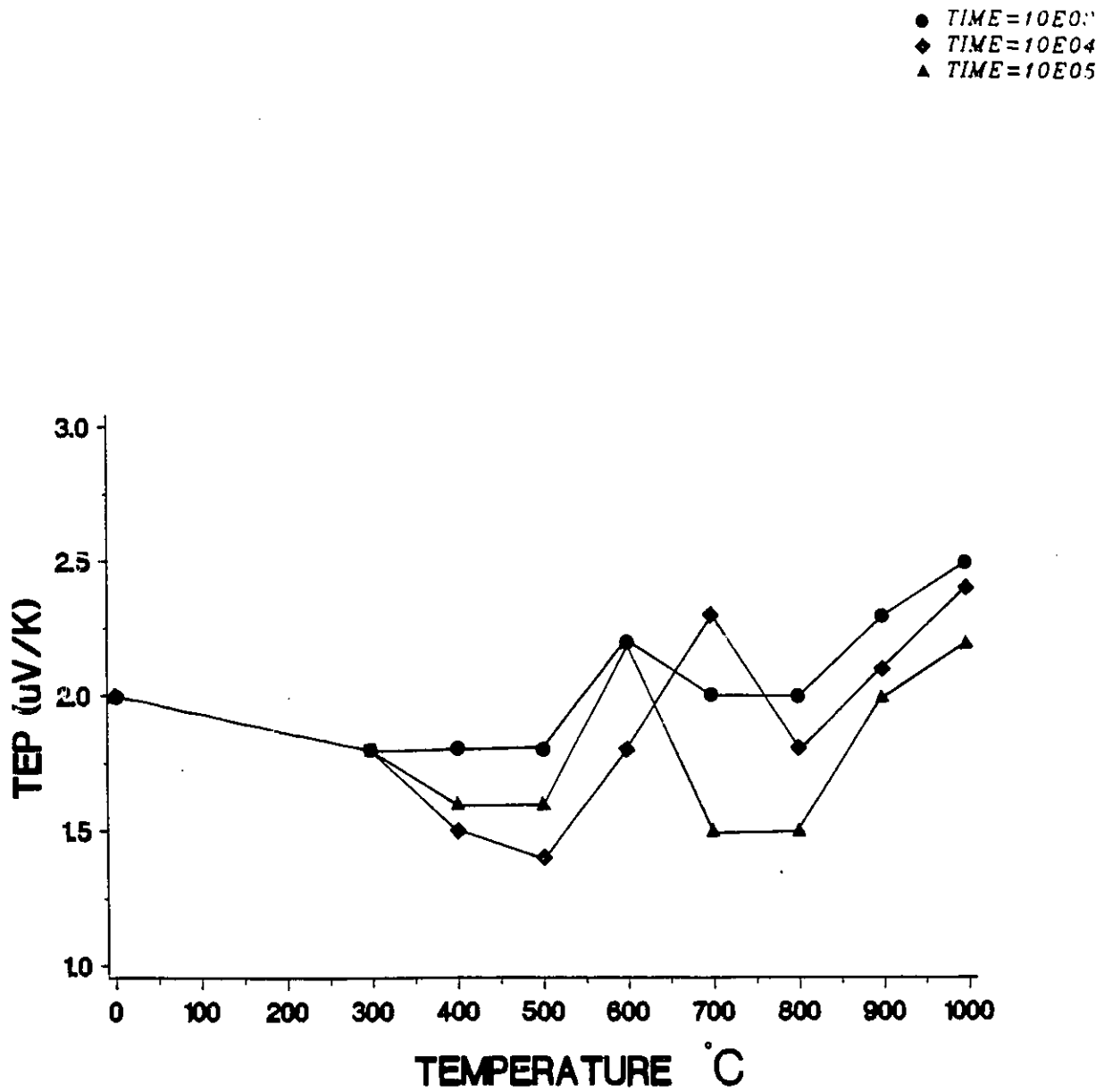
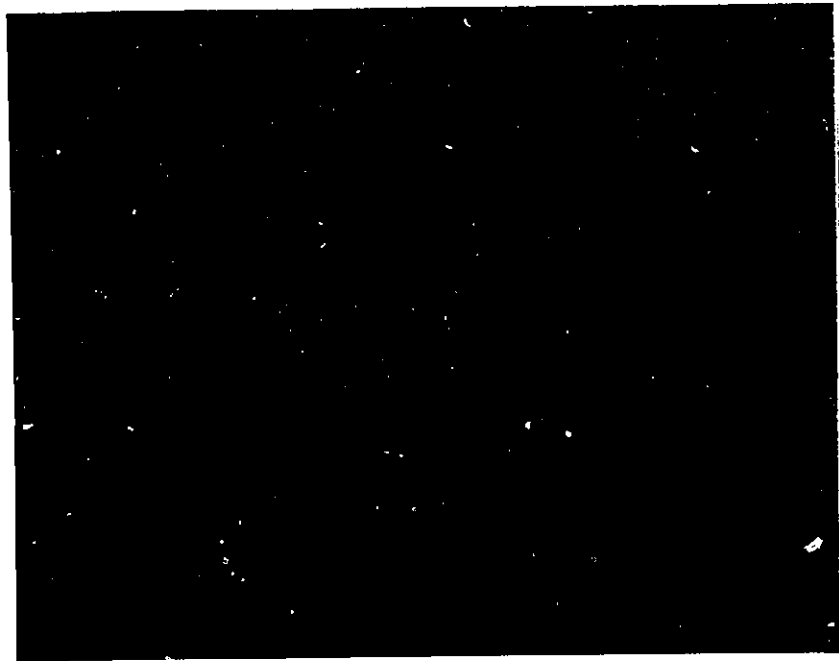
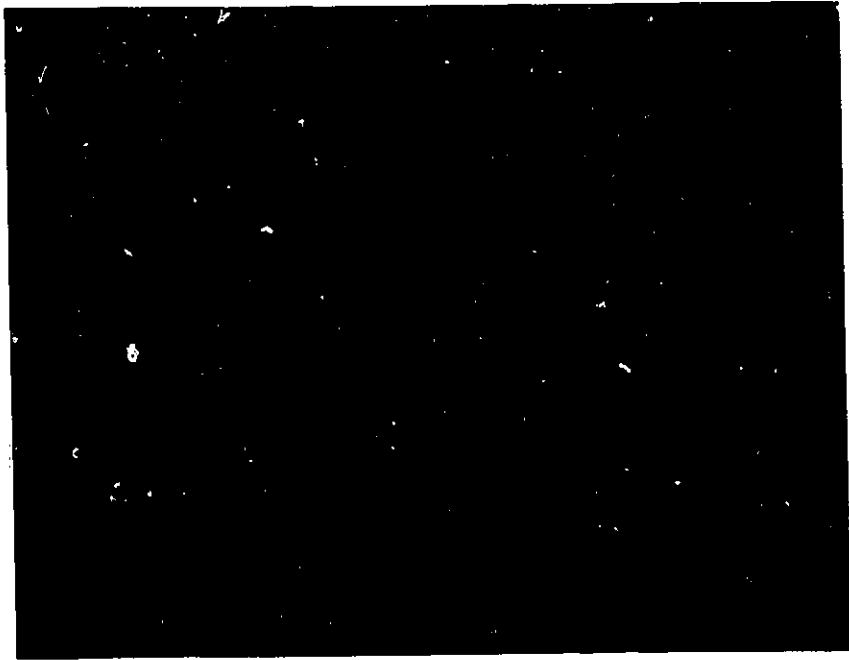


Figure 4.35 TEP vs. annealing temperature for Zircaloy-4 for an annealing time of 10^3 , 10^4 and 10^5 seconds.



20μm

Figure 4.36 Optical micrograph of Zircaloy-4 tubing in the as-received condition (using polarized light), showing elongated α -Zr grains.



20μm

Figure 4.37 Optical micrograph of Zircaloy-4 annealed at 500°C for 10³ seconds (using polarized light), showing partially recrystallized α -Zr grains.



20μm

Figure 3.38 Optical micrograph of Zircaloy-4 annealed at 500°C for 10⁴ seconds (using polarized light), showing partially recrystallized α -Zr grain.



Figure 4.39 Optical micrograph of Zircaloy-4 annealed at 500°C for 10⁵ seconds (using polarized light), showing partially recrystallized α -Zr grains.



20μm

Figure 4.40 Optical micrograph of Zircaloy-4 annealed at 600°C for 10³ seconds (using polarized light), showing recrystallized α -Zr grains.



20μm

Figure 4.41 Optical micrograph of Zircaloy-4 annealed at 600°C for 10⁴ seconds (using polarized light), showing recrystallized α -Zr grains.

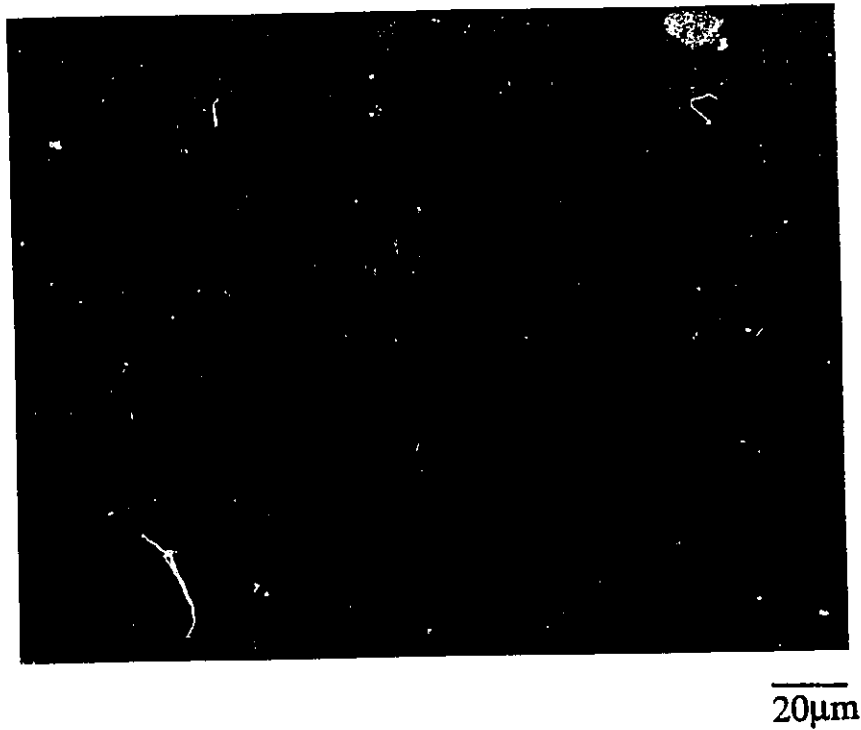


Figure 4.42 Optical micrograph of Zircaloy-4 annealed at 600°C for 10⁵ seconds (using polarized light), showing recrystallized α -Zr grains.

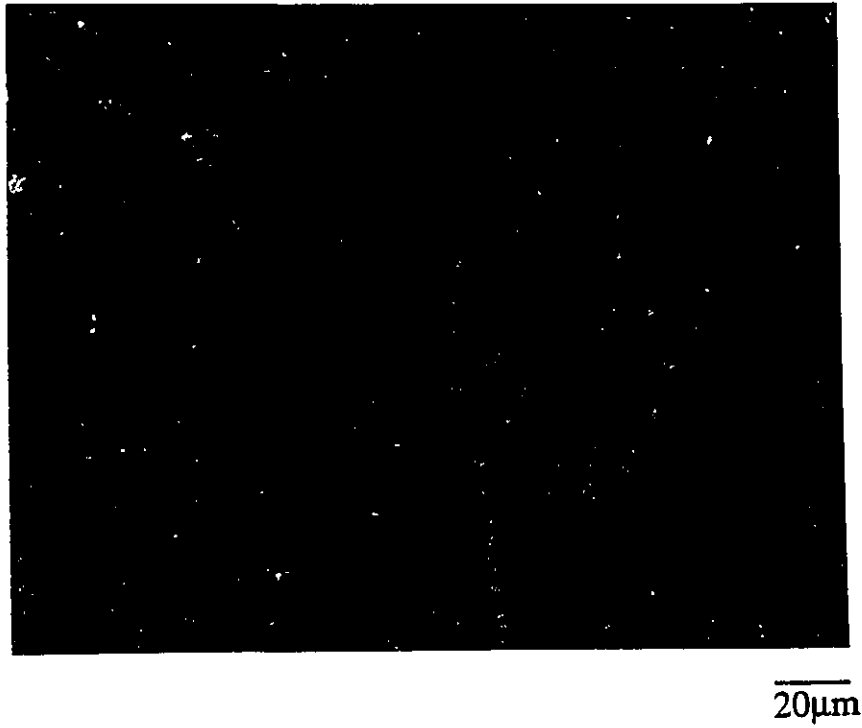


Figure 4.43 Optical micrograph of Zircaloy-4 annealed at 800°C for 10^3 seconds (using polarized light), showing α -Zr grain growth.



Figure 4.44 Optical micrograph of Zircaloy-4 annealed at 800°C for 10⁴ seconds (using polarized light), showing α -Zr grain growth .



Figure 4.45 Optical micrograph of Zircaloy-4 annealed at 800°C for 10⁵ seconds (using polarized light), showing α -Zr grain growth.



Figure 4.46 Optical micrograph of Zircaloy-4 annealed at 900°C for 10³ seconds (using polarized light), showing both α and α' structures.

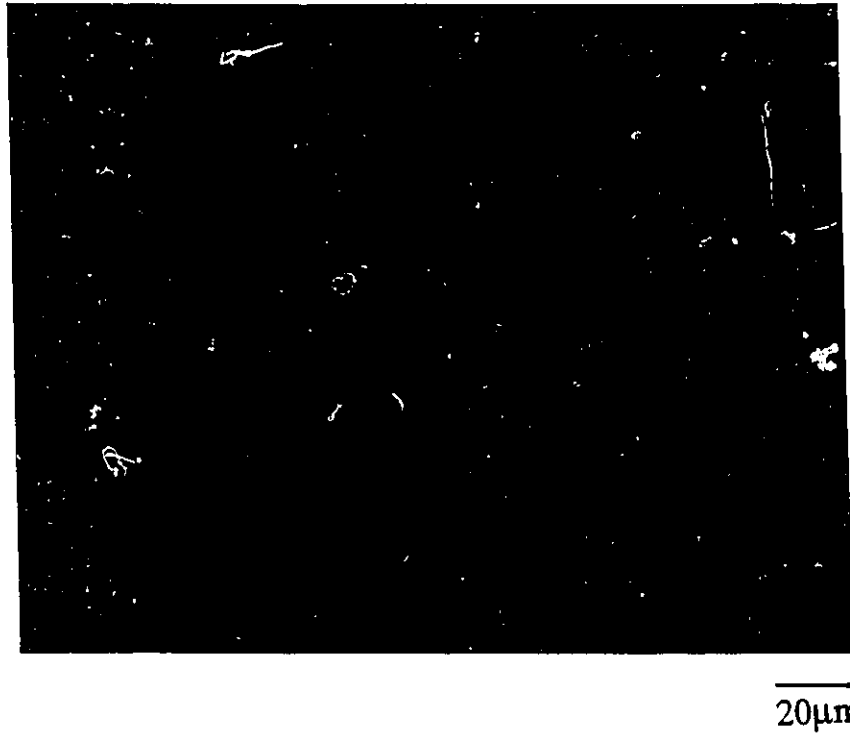
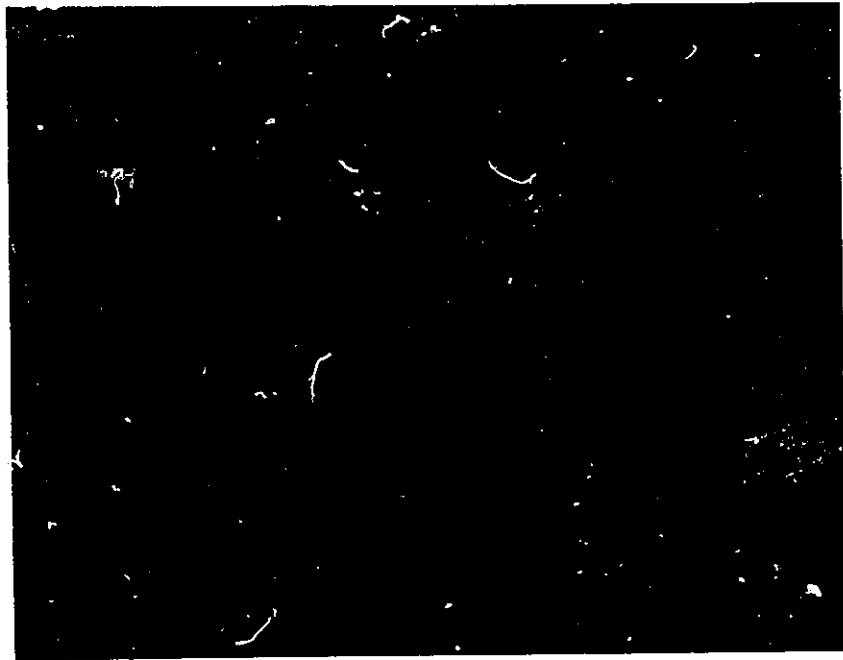


Figure 4.47 Optical micrograph of Zircaloy-4 annealed at 900°C for 10⁴ seconds (using polarized light), showing both α and α' structures.



20 μ m

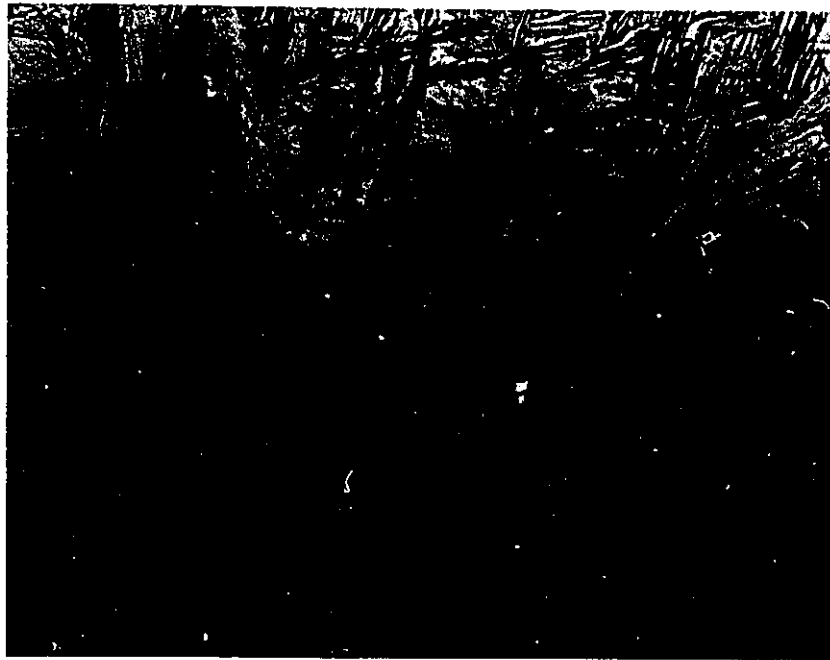
Figure 4.48 Optical micrograph of Zircaloy-4 annealed at 900°C for 10⁵ seconds (using polarized light), showing both α and α' structures.



Figure 4.49 Optical micrograph of Zircaloy-4 annealed at 1000°C for 10^3 seconds (using polarized light), showing large α' grains .



Figure 4.50 Optical micrograph of Zircaloy-4 annealed at 1000°C for 10^4 seconds (using polarized light), showing large α' grains.



50μm

Figure 4.51 Optical micrograph of Zircaloy-4 annealed at 1000°C for 10⁵ seconds (using polarized light), showing large α' grains.

Table 4.1 KHN in major directions for various heat treatment conditions for Zircaloy-4 tubing.

| Temperature °C | Time sec. | a | b | c | d | e | f |
|----------------|-----------------|-------|-------|-------|-------|-------|-------|
| A.R. * | | 296.3 | 263.1 | 226.9 | 273.5 | 284.6 | 244.0 |
| 300 | 10 ³ | 263.1 | 253.3 | 204.4 | 231.0 | 284.6 | 226.9 |
| 400 | | 284.6 | 296.0 | 211.5 | 235.2 | 284.6 | 235.2 |
| 500 | | 244.0 | 253.3 | 219.0 | 226.9 | 273.5 | 235.2 |
| 600 | | 244.0 | 244.0 | 173.7 | 204.4 | 235.2 | 219.0 |
| 700 | | 235.2 | 244.0 | 163.3 | 179.3 | 219.0 | 191.2 |
| 800 | | 211.5 | 235.2 | 153.9 | 191.2 | 226.9 | 179.3 |
| 900 | | 204.4 | 235.2 | 158.5 | 173.7 | 219.0 | 179.3 |
| 1000 | | 185.1 | 185.1 | 197.6 | 191.2 | 204.4 | 219.0 |
| 300 | 10 ⁴ | 258.1 | 244.0 | 207.9 | 222.5 | 266.1 | 219.0 |
| 400 | | 235.2 | 235.2 | 163.3 | 197.6 | 219.0 | 168.4 |
| 500 | | 235.2 | 235.2 | 191.2 | 173.7 | 263.1 | 204.4 |
| 600 | | 219.0 | 235.2 | 173.7 | 179.3 | 273.5 | 244.0 |
| 700 | | 211.5 | 226.9 | 158.5 | 168.4 | 226.9 | 173.7 |
| 800 | | 204.4 | 211.5 | 158.5 | 173.7 | 226.9 | 173.7 |
| 900 | | 235.2 | 235.2 | 153.9 | 163.3 | 204.4 | 153.9 |
| 1000 | | 204.4 | 185.1 | 197.6 | 197.6 | 211.5 | 179.3 |
| 300 | 10 ⁵ | 235.2 | 284.6 | 191.2 | 197.6 | 284.6 | 244.0 |
| 400 | | 244.0 | 244.0 | 179.0 | 226.9 | 244.0 | 197.6 |
| 500 | | 219.0 | 235.2 | 173.7 | 168.4 | 244.0 | 191.2 |
| 600 | | 204.4 | 219.0 | 185.1 | 185.1 | 226.9 | 226.9 |
| 700 | | 204.4 | 219.0 | 179.3 | 191.2 | 219.0 | 197.6 |
| 800 | | 197.6 | 211.5 | 153.9 | 163.3 | 197.6 | 163.3 |
| 900 | | 219.0 | 204.4 | 145.2 | 119.2 | 219.0 | 219.0 |
| 1000 | | 211.5 | 211.5 | 204.4 | 204.4 | 211.5 | 211.5 |

* As-recieved.
All KHN's are ±8.0.

Table 4.2 KHN, in major directions, and mechanical anisotropy ratio for Zircaloy-4 tubing annealed at various temperatures for 10^3 seconds.

| Temperature °C | Y_{FR} | Y_{θ} | Y_{π} | min/max hardness |
|-------------------|----------|--------------|-----------|---------------------|
| A.R. | 304 | 241 | 251 | 0.76 |
| 300 | 282 | 235 | 218 | 0.74 |
| 400 | 319 | 229 | 212 | 0.71 |
| 500 | 258 | 236 | 208 | 0.77 |
| 600 | 257 | 210 | 198 | 0.73 |
| 700 | 258 | 190 | 177 | 0.65 |
| 800 | 248 | 187 | 173 | 0.66 |
| 900 | 274 | 181 | 176 | 0.60 |
| 1000 | 187 | 206 | 199 | 0.89 |

Table 4.3 KHN, in major directions, and mechanical anisotropy ratio for Zircaloy-4 tubing annealed at various temperatures for 10^4 seconds.

| Temperature °C | Y_R | Y_θ | Y_z | min/max hardness |
|-------------------|-------|------------|-------|---------------------|
| 300 | 263 | 218 | 221 | 0.79 |
| 400 | 243 | 176 | 171 | 0.66 |
| 500 | 221 | 214 | 188 | 0.81 |
| 600 | 218 | 259 | 189 | 0.70 |
| 700 | 240 | 184 | 166 | 0.66 |
| 800 | 231 | 183 | 165 | 0.67 |
| 900 | 277 | 165 | 158 | 0.53 |
| 1000 | 212 | 194 | 202 | 0.91 |

Table 4.4 KHN, in major directions, and mechanical anisotropy ratio for Zircaloy-4 tubing annealed at various temperatures for 10^5 seconds.

| Temperature °C | Y_R | Y_θ | Y_Z | min/max hardness |
|-------------------|-------|------------|-------|---------------------|
| 300 | 248 | 251 | 196 | 0.67 |
| 400 | 259 | 205 | 192 | 0.71 |
| 500 | 244 | 203 | 176 | 0.67 |
| 600 | 205 | 228 | 192 | 0.82 |
| 700 | 218 | 201 | 185 | 0.82 |
| 800 | 218 | 173 | 159 | 0.70 |
| 900 | 208 | 214 | 184 | 0.82 |
| 1000 | 215 | 210 | 210 | 0.98 |

Table 4.5 The f-parameter, in major directions, at different annealing temperatures for 10^3 seconds for Zircaloy-4 tubing.

| Temperature °C | f_{radial} | $f_{\text{tangential}}$ | f_{axial} |
|-------------------|---------------------|-------------------------|--------------------|
| A.R. | 0.497 | 0.350 | 0.248 |
| 300 | 0.501 | 0.352 | 0.235 |
| 400 | 0.501 | 0.453 | 0.127 |
| 500 | 0.505 | 0.481 | 0.061 |
| 600 | 0.513 | 0.490 | 0.049 |
| 800 | 0.562 | 0.472 | 0.070 |
| 900 | 0.539 | 0.447 | 0.091 |
| 1000 | 0.318 | 0.426 | 0.280 |

All f-parameters are ± 0.009 .

Table 4.6 The f-parameter, in major directions, at different annealing temperatures for 10^4 seconds for Zircaloy-4 tubing.

| Temperature °C | f_{radial} | $f_{\text{tangential}}$ | f_{axial} |
|-------------------|---------------------|-------------------------|--------------------|
| 300 | 0.498 | 0.350 | 0.226 |
| 400 | 0.513 | 0.451 | 0.104 |
| 500 | 0.535 | 0.507 | 0.033 |
| 600 | 0.539 | 0.474 | 0.035 |
| 800 | 0.559 | 0.475 | 0.025 |
| 900 | 0.510 | 0.462 | 0.096 |
| 1000 | 0.394 | 0.456 | 0.233 |

All f-parameters are ± 0.009 .

Table 4.7 The f-parameter, in major directions, at different annealing temperatures for 10^5 seconds for Zircaloy-4 tubing.

| Temperature °C | f_{radial} | $f_{\text{tangential}}$ | f_{axial} |
|-------------------|---------------------|-------------------------|--------------------|
| 300 | 0.503 | 0.349 | 0.231 |
| 400 | 0.518 | 0.423 | 0.072 |
| 500 | 0.548 | 0.492 | 0.066 |
| 600 | 0.536 | 0.460 | 0.079 |
| 800 | 0.569 | 0.429 | 0.085 |
| 900 | 0.504 | 0.429 | 0.132 |
| 1000 | 0.431 | 0.434 | 0.231 |

All f-parameters are ± 0.009 .

Table 4.8 TEP values at different annealing temperatures for 10^3 seconds for Zircaloy-4 tubing.

| Temperature °C | ΔV volts | ΔT K | ΔS $\mu v/K$ |
|-------------------|---------------------|-----------------|-------------------------|
| A.R. | 20 | 10 | 2.0 |
| 300 | 18 | 10 | 1.8 |
| 400 | 18 | 10 | 1.8 |
| 500 | 18 | 10 | 1.8 |
| 600 | 22 | 10 | 2.2 |
| 700 | 20 | 10 | 2.0 |
| 800 | 20 | 10 | 2.0 |
| 900 | 23 | 10 | 2.3 |
| 1000 | 25 | 10 | 2.5 |

ΔS is $\pm 0.05 \mu v/K$.

Table 4.9 TEP values at different annealing temperatures for 10^4 seconds for Zircaloy-4 tubing.

| Temperature °C | ΔV volts | ΔT K | ΔS $\mu v/K$ |
|-------------------|---------------------|-----------------|-------------------------|
| 300 | 18 | 10 | 1.8 |
| 400 | 15 | 10 | 1.5 |
| 500 | 14 | 10 | 1.4 |
| 600 | 18 | 10 | 1.8 |
| 700 | 23 | 10 | 2.3 |
| 800 | 18 | 10 | 1.8 |
| 900 | 21 | 10 | 2.1 |
| 1000 | 24 | 10 | 2.4 |

ΔS is $\pm 0.05 \mu v/K$.

Table 4.10 TEP values at different annealing temperatures for 10^5 seconds for Zircaloy-4 tubing.

| Temperature °C | ΔV volts | ΔT K | ΔS $\mu\text{v/K}$ |
|-------------------|---------------------|-----------------|-------------------------------|
| 300 | 18 | 10 | 1.8 |
| 400 | 16 | 10 | 1.6 |
| 500 | 16 | 10 | 1.6 |
| 600 | 22 | 10 | 2.2 |
| 700 | 15 | 10 | 1.5 |
| 800 | 15 | 10 | 1.5 |
| 900 | 20 | 10 | 2.0 |
| 1000 | 22 | 10 | 2.2 |

ΔS is $\pm 0.05 \mu\text{v/K}$.

Table 4.11 Grain size for Zircaloy-4 tubing after various heat treatments.

| | Grain size (μm) | |
|----------------------|------------------------------|-------|
| | 600°C | 800°C |
| 10 ³ sec. | 10.5 | 19.5 |
| 10 ⁴ sec. | 13.0 | 23.0 |
| 10 ⁵ sec. | 16.0 | 35.0 |

All grain sizes are $\pm 0.5 \mu\text{m}$.

Table 4.12 Oxygen content (in ppm by weight) of Zircaloy-4 tubing in the as-received condition and after various heat treatments.

| | Oxygen content (ppm) | |
|----------------------|----------------------|--------|
| | 500°C | 1000°C |
| 10 ³ sec. | 1340 | 1340 |
| 10 ⁴ sec. | 1360 | 1470 |
| 10 ⁵ sec. | 1270 | 1510 |

As-received oxygen content is 1290 ppm.

Table 4.13 The yield strength in the tangential direction for Zircaloy-4 tubing in the as-received condition and after various heat treatments (using ring tensile tests).

| Yield strength (θ-direction) Kpsi | | |
|--------------------------------------|-----------|------------|
| As-received | | 87.3 |
| | 500 °C | 1000 °C |
| 10 ³ ϕ | 86.1 | 88.0 |
| 10 ⁴ ϕ | 107.5 | 78.9 |
| 10 ⁵ ϕ | 79.8 | 78.0 |

CHAPTER 5

DISCUSSION

The changes experienced by the Zircaloy-4 fuel cladding on annealing at temperatures up to 1000°C can be divided into three main categories, namely recovery, recrystallization, and phase transformation. In general, removal of cold work occurs at the lower annealing temperatures ($\leq 600^\circ\text{C}$) in the recovery and recrystallization stages. Phase transformation, however, occurs at higher annealing temperatures ($\geq 900^\circ\text{C}$). These three general categories were monitored for all three annealing durations (10^3 , 10^4 , and 10^5 seconds).

The recovery process was "best" monitored by the TEP measurements. Recovery effects were, of course, not visible using optical metallography. A decrease in TEP value was detected in the temperature range 300 to 400°C which defines the recovery stage for all three annealing times. Generally, only a small decrease in microhardness was observed in this temperature range. However, the microhardness in the radial and tangential

directions, for 10^3 and 10^4 seconds annealing periods, respectively, increases slightly during the recovery stage. A similar increase in hardness, in the recovery stage, has been observed in cold-worked 70-30 brass annealed at lower temperatures⁽²¹⁾.

The recovery process has no effect on the mechanical anisotropy ratio and only a small effect on texture. The f-parameter increases slightly in the tangential direction accompanied by a corresponding decrease in the f-parameter in the axial direction, with no significant change in the axial direction. Although the mechanical anisotropy remained fairly constant (same as for the as-received tubing) a slight shift in the effective number of poles from the tangential to the axial direction took place.

Recrystallization effects were effectively monitored by a number of the different techniques used in this study, and were found to occur in the temperature range 500 to 600°C for all three annealing times. Recrystallization is readily seen in the optical micrographs, starting at a temperature of 500°C as very fine equiaxed crystals and is essentially complete at a temperature of 600°C.

Recrystallization was also seen as an increase in the TEP value in the 500 to 600°C temperature range. A significant decrease in Knoop microhardness also occurred in this temperature range because of the newly formed, stress free, crystals. This general pattern is seen in all directions and for all annealing times with the exception of the microhardness in the tangential direction for a 10^4 seconds annealing time. The Knoop microhardness in this direction is increased in the recrystallization temperature range (500 to 600°C). This behaviour can to some extent be explained by looking at the recrystallization texture of the tubing under these annealing conditions. The f-parameter for an annealing time of 10^4 is larger than the corresponding ones for both 10^3 and 10^5 seconds annealing times (see Tables 4.(5-7)). Thus the effective number of basal poles in the tangential direction, for 10^4 seconds annealing time, is larger than that in the tangential direction for 10^3 and 10^5 seconds annealing time. This gives rise to an increase in microhardness since the basal pole direction in the hcp α -Zr crystal is the strongest direction. Because deformation occurs by slip on the system $[10\bar{1}0]\langle\bar{1}210\rangle$, and all the slip directions are perpendicular to $[0001]$, deformation along $[0001]$ cannot be accommodated by slip. Instead twinning occurs and this requires a higher resolved shear stress than slip, making the $[0001]$ direction the

stronger direction in the crystal.

However, although the f -parameter is larger in the radial direction (at 600°C and 10^4 seconds) than that in the tangential direction, the microhardness is higher in the latter direction. This might be due to activation of new slip systems in the radial direction that have a lower resolved shear stress, when deformed along [0001], than the resolved shear stress required by the slip system $[10\bar{1}0]\langle 1\bar{2}10\rangle$. Another factor that may contribute to the sudden rise in microhardness in the tangential direction (at 500 to 600°C for 10^4 seconds) is the grain size effect. Table 4.1 shows that the grain size for 10^5 seconds is slightly larger than that for 10^4 seconds at the same annealing temperature, hence, a softer structure. It should be mentioned that this type of behaviour (increase in KHN during the recrystallization stage) is also evident for the 10^5 seconds and 600°C but on a much smaller scale.

During the recrystallization stage (500 to 600°C) the mechanical anisotropy ratio drops for annealing times of 10^3 and 10^4 seconds, ie. the recrystallized structure of the tubing is more anisotropic than the as-received tubing. However, an increase in the mechanical anisotropy ratio

(towards a more isotropic behaviour) occurs when the tubing is heated for 10^5 seconds in the recrystallization temperature range. The mechanical anisotropy ratio changes are attributed to the recrystallization texture developed on heating. During recrystallization the f-parameter in the tangential direction increases to a maximum with a corresponding decrease in the f-parameter in the axial direction and a slight increase in the f-parameter in the radial direction. This general trend appears for all annealing times used in this study, however, the "difference" between f-parameters in any two directions is changing with change in annealing time (for any particular annealing temperature). For example, at 500°C the difference in the f-parameter between the tangential and radial directions is larger for an annealing time of 10^5 seconds than for annealing times of 10^3 and 10^4 seconds. The difference in the f-parameter between the radial and tangential directions is small for samples annealed for 10^3 seconds (at 500 and 600°C) which is indicative of crystallographic isotropy in the radial-tangential plane.

For annealing temperatures from 600 to 800°C the tubing exhibits no significant changes. The microhardness drops slowly due to grain growth effects, which are seen by comparing α -grain sizes at 500 and 800°C . The

texture in this temperature range is reasonably constant in all directions of the tubing. Also there is no significant change in mechanical anisotropy ratio.

Phase change effects were recorded at annealing temperatures of 900 and 1000°C. In this temperature range, changes in both mechanical and crystallographic anisotropy took place. Phase changes were also reflected as an increase in the TEP value.

An increase in microhardness is evident in both the axial and tangential directions when annealed at 900 to 1000°C. This increase is accompanied by a decrease in microhardness in the radial (for annealing times of 10^3 and 10^4 seconds) direction and no significant change in microhardness in the radial direction for an annealing time of 10^5 seconds. The microhardness in all directions of the tubing is essentially the same at 1000°C (for any particular annealing time) which is indicative of mechanical isotropy. This is also reflected in the mechanical anisotropy ratio, which shows an increase in the "minimum/maximum hardness" ratio approaching unity at annealing temperature of 1000°C. The texture at this temperature (1000°C) undergoes a major change in the radial and axial

directions. For annealing time of 10^3 and 10^4 seconds (at 1000°C) the f -parameter in the radial direction drops and becomes smaller than the f -parameter in the tangential direction. This is accompanied by a corresponding increase in the f -parameter in the axial direction and a slight decrease in the f -parameter in the tangential direction. For an annealing time of 10^5 seconds the f -parameters in the radial and tangential directions are exactly the same which reflects the crystallographic isotropy in the radial-tangential plane of the tubing. For all annealing times used in this study, the f -parameter approaches a value of $1/3$ in all directions at an annealing temperature of 1000°C , and thus the tubing is crystallographically isotropic.

Optical metallography at 900°C shows that the volume fraction of transformed β (α') in the structure increases with annealing time, the volume fraction being 10, 30, and 50% for 10^3 , 10^4 , and 10^5 seconds annealing time, respectively. However, at the annealing temperature of 1000°C the microstructure is 100% transformed β , for all annealing times. The microhardness appears to increase with an increase in transformed β (α') in the structure (at 900°C).

The overall increase in the microhardness in the 900 to 1000°C range is due to two effects. The first effect is the major one which is the presence of transformed β in the structure, as discussed above. The second effect is the oxygen content of the tubing which is known to have a strengthening effect. However, the oxygen effect is slight as seen by comparing the microhardness values at a 1000°C for the different annealing times. This shows that the microhardness tends to increase only slightly with an increase in the oxygen content of the tubing. The increase in the "average" microhardness (the KHN values averaged over all three directions of the tubing), when increasing the annealing time from 10^3 seconds to 10^5 seconds, per 100 ppm increase in oxygen content is estimated to be 9 KHN/(100 ppm O).

The microhardness in any direction in the temperature range 900 to 1000°C is directly proportional to the effective number of basal poles in that direction, i.e. an increase or a decrease in the effective number of basal poles in one direction causes an increase or a decrease, respectively, in the microhardness. This is seen by comparing the KHN vs. temperature plots with their corresponding f-parameter vs temperature plots. This effect is more evident in the radial and axial directions.

Figure 5.1 is a schematic diagram giving a summary of the effects of annealing temperature on the Zircaloy-4 fuel tubing both in terms of microstructural and crystallographic changes and in terms of property changes. The diagram (Fig. 5.1) is divided into three major parts. The first part is recovery which takes place at lower temperatures. The second part is recrystallization which starts at about 500°C. The third part of this diagram is phase transformation which starts at about 890°C. The Zr-Sn phase diagram (Fig. 2.11) shows that at 900°C (Zr-1.5wt% Sn) only a single β -Zr phase exists. However, metallographic examinations of Figures 4.46 to 4.48 show both α and α' phases even at the longer annealing time of 10^5 seconds. This suggests that at 900°C both the α -Zr and β -Zr exist. A shift in the transus line, α -Zr/(α -Zr + β -Zr), from 870 to 890°C occurred due to oxygen content of the as-received tubing (~1300 ppm). Moreover, the existence of both α -Zr and β -Zr at 900°C might also be due, to lesser extent, to temperature fluctuations during annealing.

The Knoop microhardness flow surfaces were compared to the ring test results (Table 5.1). The predicted yield strength values were found by calibrating the flow surface. The calibration factor is the ratio of the ring yield strength (in the θ -direction) to its corresponding Knoop

microhardness value. A mean calibration factor has been calculated and found to be 0.4040 Ksi per KHN.

The % error, between the yield strength predicted by the Knoop microhardness flow surface and the one determined by the ring tensile test, vary from 0.6% to a maximum error of 19.6% and the mean error is only 8.5%. These results verify the validity of the Knoop microhardness flow surface technique as means of determining mechanical anisotropy non-destructively.

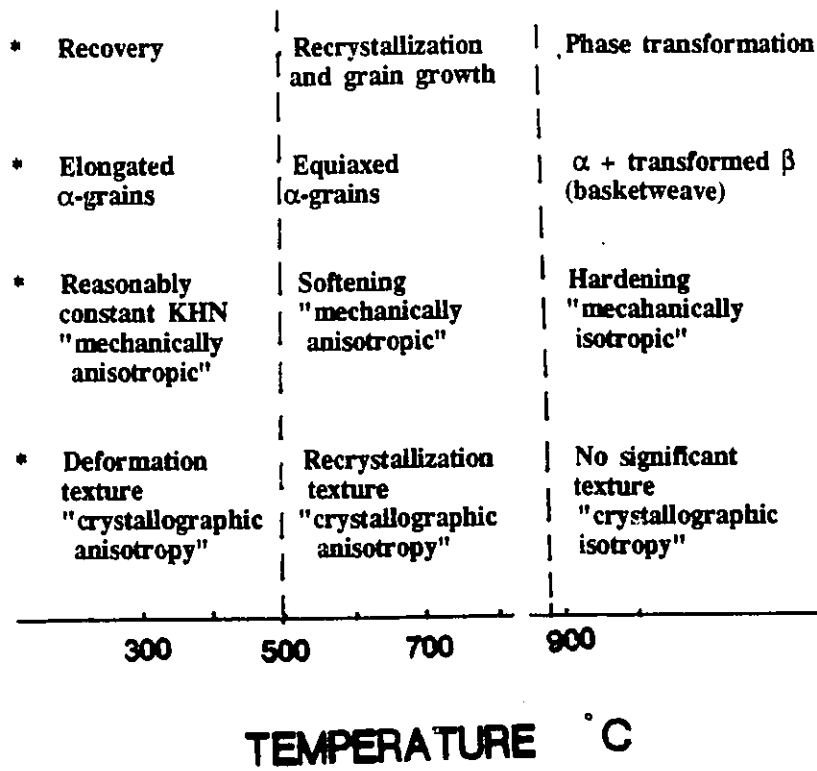


Figure 5.1 Schematic diagram showing the effect of annealing temperature on the Zircaloy fuel tubing.

Table 5.1 Predicted and measured yield strength values for Zircaloy-4 tubing for the as-received tubing and after various heat treatment conditions.

| | | Yield strength (θ-direction) Ksi | | |
|-------------|-------------------|-------------------------------------|-------------------|---------|
| | | Flow surface prediction | Ring tensile test | % Error |
| As-received | | 97.4 | 87.3 | 11.6 |
| 500°C | 10 ³ s | 95.3 | 86.1 | 10.7 |
| | 10 ⁴ s | 86.4 | 107.5 | 19.6 |
| | 10 ⁵ s | 82.0 | 79.8 | 2.8 |
| 1000°C | 10 ³ s | 83.2 | 88.0 | 5.5 |
| | 10 ⁴ s | 78.4 | 78.9 | 0.6 |
| | 10 ⁵ s | 84.8 | 78.0 | 8.7 |

CHAPTER 6

CONCLUSIONS

AND RECOMMENDATIONS

6.1 CONCLUSIONS

This investigation into the effect of annealing, for 10^3 , 10^4 and 10^5 seconds, at temperatures from 300 to 1000°C on the mechanical and crystallographic anisotropy of Zircaloy-4 nuclear fuel tubing indicates that:

1- The Zircaloy-4 fuel tubing is highly anisotropic and remains so to a very high temperature (900°C) before a relatively sharp change occurs and the tubing becomes essentially isotropic.

2- Recovery effects occurred in the annealing temperature range 300 to 400°C . The TEP technique was particularly sensitive in monitoring recovery effects which could not be detected easily by microhardness tests or be seen by light microscopy. TEP measurements were proven to be useful in monitoring low temperature, as well as high temperature, changes

occurring in the fuel cladding on heating.

3- Annealing at temperatures up to 500°C, which is below the recrystallization temperature, for times of 10^3 , 10^4 and 10^5 seconds, produced little change in texture, microhardness and mechanical anisotropy ratio.

4- The Zircaloy-4 fuel cladding exhibits a major softening when heated at, or above, the recrystallization temperature. This is true for all tubing directions except in the tangential direction when heated for 10^4 seconds, which exhibits an increase in microhardness.

5- During recrystallization, Zircaloy-4 tubing exhibits changes in texture with the formation of a "recrystallization texture" which is different from that of the as-fabricated tubing.

6- The Zircaloy-4 fuel cladding becomes more mechanically anisotropic as a result of the recrystallization.

7- Transformed β (α') starts to appear in the microstructure, on heating, at

900°C with an increasing volume fraction being formed with an increase in annealing time. Heating at 1000°C brings the Zircaloy-4 fuel cladding to the β -Zr single phase region. On cooling to room temperature, large grains of 100% transformed β are formed. This transformed β has a basketweave structure.

8- The microhardness in both the axial and tangential directions increases with an increase in the amount of transformed β in the microstructure, since the overall microhardness of the transformed β structure is higher than that of the recrystallized α -Zr.

9- The mechanical anisotropy ratio approaches unity, i.e. "isotropy", at 1000°C. The crystallographic texture also shows isotropy at 1000°C.

10- Generally speaking, the microhardness is directly proportional to the effective number of basal poles in any one direction, i.e. it is proportional to the f-parameter.

11- A significant absorption of oxygen only took place upon annealing at 1000°C for longer times, i.e. 10^4 and 10^5 seconds. This increase in oxygen

content produced only a slight increase in microhardness.

12- The microhardness flow surface is a very useful technique for the non-destructive determination of mechanical anisotropy.

13- A 20°C shift in the transus line, $\alpha\text{-Zr}/(\alpha\text{-Zr} + \beta\text{-Zr})$, from 870°C to 890°C as a result of the oxygen content of the tubing.

14- The yield strengths determined by the ring tensile tests are in good agreement with the corresponding ones predicted by the Knoop microhardness flow surface.

6.2 RECOMMENDATIONS

1- Further investigation in the temperature range 800 to 1000°C is recommended to determine the equilibrium temperature at which transformed β forms.

2- Investigate the effect of the $\alpha\text{-Zr}$ layers in the transformed β microstructure on the overall texture of the tubing.

3- Study the effect of the initial texture of the tubing on the resulting recrystallization texture.

4- For further verification of the flow surface a closed-end and a tensile test are recommended.

5- Thermodynamic explanation of anisotropy changes.

REFERENCES

- 1 - L. F. P. Van Swam, D. B. Knorr, R. M. Pelloox, and J. F. Shewbridge (1979). Trans. AIME, 10A, p. 483.
- 2 - Kister Kallstrom (1972). Can. Met. Quar., 11, p. 185.
- 3 - J. J. Kearns (1965). AEC Report, Westinghouse Atomic Power Division-Technical Memorandum, WAPD-TM-472.
- 4 - L. G. Schulz (1949). J. App. Phys., 20, p. 1030.
- 5 - B. F. Decker, E. T. Aps, and D. Harker (1947). J. App. Phys., 19, p. 388.
- 6 - G. B. Harris (1952). Comm. National Phys. Lab., 43, p. 113.
- 7 - Sheikh T. Mahmood and K. Linga Murty (1989). J. Eng. Mat., 11, p. 315.
- 8 - H. R. Wenk, H. J. Bunge, J. S. Kallend, K. Lucke, S. Matthies, J. Pospiech, and P. Van Houtte (1988). Conf. Proc. Eighth International Conference On Texture Of materials (ICOTOM 8), p. 17.
- 9 - C. C. Sanderson (1965). *The Effect of Specimen Geometry on the Tensile Properties of Some Zirconium Alloys*, Atomic Energy of Canada Limited Report, AECL.2207.
- 10- P. C. Bera and M. G. Wright (1975). *Effect of Temperature and Time on the Anisotropy of Zircaloy-4 Fuel Cladding*, Atomic Energy of Canada Report, WNRE Report-229.
- 11- R. G. Wheeler and D. R. Ireland (1966) . Electrochemical Tech., 4, p. 313.
- 12- R. Hill (1948). Proc. Roy. Soc. London, 193A, p. 281.
- 13- R. D. Barnard. *Thermoelectricity in Metals and Alloys*, Taylor and Francis, London, 1972.

- 14- D. K. MacDonald. *Thermoelectricity*, Wiley, N.Y., 1962.
- 15- P. Merle, R. Borrely (1986). *Scripta Metallurgica*, 20, p. 1089.
- 16- P. Merle, C. Vauglin, G. Fantozzi, J. Derep, and D. Charquet (1987). American Society of Testing and Materials ASTM, Special Technical Publication STP 939, Philadelphia, p. 555.
- 17- Zheng Jie, John W. Robinson and Derek O. Northwood (1989). *Microstructural Science*, 17, p. 393.
- 18- Zheng Jie, John W. Robinson and Derek O. Northwood (1989). The Metallurgical Society (AIME), Technical Paper no. A89-20.
- 19- G. J. C. Carpenter, E. F. Ibrahim and J. F. Watters (1981). *J. Nuc. Mat.*, 102, p. 280.
- 20- C. J. Rosa (1968). *J. Less Comm. Met.*, 16, p. 173.
- 21- R. A. Higgins. *Engineering Metallurgy*, R. E. Krieger Publication Company, Florida, 1983.
- 22- Derek O. Northwood, John W. Robinson and Zheng Jie (1991). *Texture and Microstructures*, 13, p. 133.
- 23- Derek O. Northwood, John W. Robinson and Zheng Jie (1990). *Conf. Proc., Recrystallization '90*, Australia.
- 24- T. B. Massalski. *Binary Alloy Phase Diagrams*, American Society of Metals, Ohio, 1986.
- 25- W. R. Tyson (1967). *Can. Met. Quar.*, 6, p. 301.

BIBLIOGRAPHY

- 1 - H. G. Hellmut. *Crystal Physics*, Advanced Book Programe, N.Y., 1974.
- 2 - J. D. Lubahn and R. P. Felgar. *Plasticity and Creep of Metals*, Wiley, New York, 1961.
- 3 - Erich Tenckhoff (1988). American Society of Testing and Materials ASTM, Special Technical Publication STP 966, Philadelphia.
- 4 - G. Abbruzzese, K. Lucke, and H. Eichelkraut (1988). Conf. Proc. Eighth International Conference On Texture Of Materials (ICOTOM 8), p. 693.
- 5 - N. V. Bangaru (1985). *J. Nuc. Mat.*, 131, p. 280.
- 6 - C. R. Calladine. *Engineering Plasticity*, 1st ed., Peragamon Press, 1969.
- 7 - M. A. Meyers and K. K. Chawla. *Mechanical Metallurgy*, Prentice-Hall Inc., N.J., 1984.
- 8 - George E. Dieter. *Mechanical Metallurgy*, 3rd. ed., McGraw-Hill, New York, 1986.
- 9 - Derek O. Northwood (1985). *Materials and Design*, 2, p. 58.
- 10- R. M. Caddell and W. F. Hosford. *Metal Forming*, Prentice-Hall, N.J., 1983.
- 11- B. D. Cullty. *Elements of X-ray Diffraction*, 2nd. ed., Addison-Wesely Publication Co. Inc., 1967.
- 12- C. S. Barrett and T. B. Massalski. *Structure of Metals*, 3rd. ed., McGraw-Hill, New York, 1980.

- 13- E. F. Ibrahim, R. Choubey and J. J. Jonas (1984). *J. Nuc. Mat.*, 126, p. 44.
- 14- Derek O. Northwood and W. L. Fong (1983). *Can. Met. Quar.*, 22 no. 3, p. 411.
- 15- R. Borrelly, P. Merle, and L. Adami (1990). *J. Nuc. Mat.*, 170, p. 147.
- 16- R. Hill. *Mathematical Theory of Plasticity*, Oxford Univ. Press, London, 1950.
- 17- V. Valvoda (1990). *Powder Diffraction*, 5 no. 4, p. 200.
- 18- H. J. Bunge, C. Esing, and J. Muller (1988). *Conf. Proc., Eighth International Conference On Texture Of Materials (ICOTOM 8)*, p. 61.
- 19- Sheriff A. Hussien, Sheikh T. Mahmood, and K. L. Murty (1988). *Conf. Proc., Eighth International Conference On Texture Of Materials (ICOTOM 8)*, p. 843.
- 20- H. Inove and N. Inakazu (1988). *Conf. Proc., Eighth International Conference On Texture Of Materials (ICOTOM 8)*, p. 997.
- 21- A. Tylor. *X-ray Metallography*, Wiley, New York, 1961.
- 22- R. G. Ballinger, G. E. Lucas, and R. M. Pelloux (1984). *J. Nuc. Mat.*, 126, p. 53.
- 23- Sheikh T. Mahmood and K. L. Murty (1988). *Conf. Proc., Eighth International Conference On Texture Of Materials (ICOTOM 8)*, p. 1117.
- 24- M. H. Muller, W. P. Chernock, and P. A. Beck (1958). *Trans. AIME*, 212, p. 39.
- 25- R. A. Holt (1970). *J. Nuc. Mat.*, 35, p. 322.
- 26- M. J. Philippe, F. Wagner, and C. Esling. (1988). *Conf. Proc., Eighth*

- International Conference On Texture Of Materials (ICOTOM 8), p. 837.
- 27- S. L. Wadekar, V. V. Raman, S. Banerjee and M. K. Asundi (1988). J. Nuc. Mat., 151, p. 162.
 - 28- T. Kubo, Y. Wakashima, K. Amano, and M. Najai (1985). J. Nuc. Mat., 132, p. 1.
 - 29- Ka-Yu Huang and Chuen-Horng (1985). J. Nuc. Mat., 136, p. 16.
 - 30- I. Iordanova, k. S. Forcey, D. K. Ross, J. Mayers, and A. C. Hannon (1989). Material Science and Technology, 5, p. 665.
 - 31- S. K. Hwang and G. P. Sabol (1988). J. Nuc. Mat., 151, p. 327.
 - 32- C. Tome, A. Pochettino, and R. Penelle (1988). Conf. Proc., Eighth International Conference On Texture Of Materials (ICOTOM 8), p. 985.
 - 33- W. A. Backofen, W. F. Hosford, and J. J. Burke (1962). Trans. ASM, 55, p. 264.
 - 34- M. A. Eisenberg, C. S. Hartley, Hu-chul Lee, and C. F. Yen (1980). J. Nuc. Mat., 88, P. 138.
 - 35- G. E. Lucas, and A. L. Bement (1975). J. Nuc. Mat., 55, p. 246.
 - 36- W. M. Evans, R. F. Gessner, and J. G. Goodwin (1972). Met. Trans., 3, p. 2879.
 - 37- E. Ortlieb, G. Cheliotis and H. G. Weidinger (1985). J. Nuc. Mat., 132, p. 205.
 - 38- D. Clurchea (1984). J. Nuc. Mat., 131, p. 1.
 - 39- L. P. Tarasov and N. W. Thibault (1947). Trans. ASM, 38, p. 331.
 - 40- J. M. Pelletier and R. Borrely (1981). Mater. Sci. and Eng., 55, p. 191.

- 41- J. M. Pelletier, G. Vigier, and R. Borrely (1982). *Scripta Metallurgica*, 16, p. 1343.
- 42- D. Benkirat, P. Merle and R. Borrely (1988). *Acta Metallurgica*, 36 no. 3, p. 613.
- 43- F. Haessner. *Recrystallization of Metallic Materials*, Dr. Riedere Verlag GmbH, Germany, 1978.

APPENDIX

ERROR ANALYSES

1 - MICROHARDNESS MEASUREMENTS

- i - The Knoop hardness tester has an uncertainty of ± 5 hardness numbers.
- ii- The mean KHN value was determined by

$$\bar{X} = (\sum X_i)/n \quad \text{A.1}$$

where \bar{X} is the mean KHN (Table. 4.1), X_i is the i^{th} KHN measurement and n is the number of KHN measurements taken for each indenter orientation ($n=6$).

- iii- The Knoop microhardness data scatter around a mean KHN value was calculated for each indenter orientation, j , by

$$S_j = [\sum(X_i - \bar{X})^2/(n-1)]^{1/2} \quad \text{A.2}$$

where S is known as the standard deviation. A mean deviation \bar{S} was

calculated by

$$\bar{S} = (\sum S_i)/N \quad \text{A.3}$$

where N is the number of the indenter orientations for all samples (N=150). The mean deviation was found to be ± 8.0 KHN , this was entered in Figures 4.29 to 4.31 as error bars of ± 8.0 KHN.

2- THERMOELECTRIC POWER MEASUREMENTS

i- The uncertainty in the TEP set-up, $U_{\Delta S}$, was calculated by the use of Taylor's theorem,

$$U_{\Delta S} = [(U_{\Delta V} (\partial \Delta S / \partial \Delta V))^2 + (U_{\Delta T} (\partial \Delta S / \partial \Delta T))^2]^{1/2} \quad \text{A.4}$$

where $U_{\Delta V}$ is the uncertainty in the voltage measurement and is equal to $\pm 0.5 \mu\text{v}$, and $U_{\Delta T}$ is the uncertainty in the temperature measurement and is equal to ± 0.5 K. Since $\Delta S = \Delta V / \Delta T$ (equation 2.14), thus by differentiating and arranging equation A.4 we get,

$$U_{\Delta S} = [(U_{\Delta V}^2 / \Delta T^2) + (U_{\Delta T}^2 \Delta V^2 / \Delta T^4)]^{1/2} \quad \text{A.5}$$

For ΔT of 10 K and ΔV of 25 μV (the largest ΔV value measured), $U_{\Delta S}$ becomes $\pm 0.06 \mu\text{V/K}$. Thus, the maximum uncertainty in the calculation of ΔS is $\pm 0.06 \mu\text{V/K}$.

ii- The average scatter of the TEP measurements around the mean ΔS values (Tables 4.8 to 4.10) was calculated using equations A.1 to A.3 and was found to be $\pm 0.05 \mu\text{V/K}$.

VITA AUCTORIS

Name Zoheir N. Farhat

Birth September 27th, 1962
Tripoli Libya.

Education B. A. Sc. (1989) in Engineering Materials
at the University of Windsor
Windsor, Ontario, Canada.

M. A. Sc. (1991) in Engineering Materials
at the University of Windsor
Windsor, Ontario, Canada.